Technische Universität München
Fakultät für Chemie
Lehrstuhl für Theoretische Chemie

Multiscale Modeling of Disorder in Solid-State Battery Materials

Hendrik Helge Heenen

Dissertation

Technische Universität München
Fakultät für Chemie
Lehrstuhl für Theoretische Chemie

Multiscale Modeling of Disorder in Solid-State Battery Materials

---

Hendrik Helge Heenen

Vollständiger Abdruck der von der
Fakultät für Chemie der Technischen Universität München
zur Erlangung des akademischen Grades eines

Doktors der Naturwissenschaften (Dr. rer. nat.)

genehmigten Dissertation.

Vorsitzender: Priv.-Doz. Dr. Harald Oberhofer

Prüfer der Dissertation:

1. Prof. Dr. Karsten Reuter
2. Prof. Dr. Tom Nilges

Die Dissertation wurde am 21.06.2018 bei der Technischen Universität München eingereicht und durch die Fakultät für Chemie am 16.07.2018 angenommen.

Für meine Eltern
Für Vanessa

"Ordnung braucht nur der Dumme, das Genie beherrscht das Chaos."

- Albert Einstein

. . . oder ein Computer.

Preface

All work presented in this doctoral thesis was performed between June 2014 and May 2018 at the Chair of Theoretical Chemistry of the Technical University of Munich (TUM), under the supervision of Prof. Dr. Karsten Reuter. A research stay hosted by Prof. Dr. Alan Luntz at the SUNCAT Center for Interface Science and Catalysis at SLAC National Accelerator Laboratory, Stanford University complemented the work performed locally at TUM. Parts of this dissertation have been published before in Ref. [1].

Garching, June, 2018

Hendrik Heenen

Abstract

Atomistic simulations of battery materials have greatly improved our understanding of the elementary thermodynamic and kinetic processes in corresponding compounds. In most computational studies density functional theory (DFT) is the method of choice due to the strong predictive power founded in its quantum mechanical origin. The contribution of such studies ranges from the characterization of the materials performance in battery applications [2–4] to the prediction of new materials in screening approaches [5–8]. Unfortunately, DFT presents a major bottleneck in terms of computational cost. This restricts its applicability to only most simple model structures. Even at the limit of what is computationally tractable with present day resources, such models grossly oversimplify the strong inherent disorder that is typically present in battery materials. In an attempt to overcome this limitation, coarse grained approaches are often employed which permit the computation of larger length and time scales. For example, contemporary studies use cluster expansion, kinetic Monte-Carlo or percolation models [4, 9, 10]. These rely on input from DFT calculations and thus enable an extrapolated evaluation of the relevant macroscopic properties. However, a major shortcoming of these coarse grained models is the significant restriction of atomic degrees of freedom (DOF). These DOFs contain detailed information which is critical for an accurate representation of disorder effects.

In this thesis, new computational approaches for different classes of materials are therefore elaborated. These approaches employ DFT validated or parameterized force field potentials, whose advantageous numerical efficiency allows for treating large system sizes while retaining the crucial DOFs. The force field potentials are integrated into a simulation strategy which includes extensive sampling from Monte-Carlo (MC) and/or molecular dynamics (MD) methods.

This unique combination of methodological tools provides unprecedented insight into the implications of structural disorder on battery performance. The latter are hereby demonstrated for two showcase battery materials that are of great technological value. In a first application to the anode material $Li_4Ti_5O_{12}$ (LTO), novel disorder-stabilized defects are revealed which promote high localized mobility. This gives rise to a correlated ion diffusion mechanism that can rationalize the hitherto unexplained high rate capabilities of this material [1]. Secondly, for the glass-amorphous Li_3OCl solid-state electrolyte, non-unity transference numbers are predicted which suggest a performance limiting concentration polarization. It is reasonable to expect that much of the hereby derived physical insight extends also to other applications of configurationally disordered compounds. This work thus overall underscores the importance of disorder-induced relationships in battery materials. Most importantly, such effects only become apparent on large simulated length and time scales, which are not accessible with DFT. Therefore, the presented methodology establishes a protocol that can be employed to uncover disorder relationships in other technologically relevant materials. Ultimately, this opens the road towards a deeper understanding of transport phenomena in general and help guide future efforts for designing next-generation battery materials.

Zusammenfassung

Atomistische Simulationen von Batteriematerialien verbessern das Verständnis der grundlegenden thermodynamischen und kinetischen Vorgänge in entsprechenden Stoffklassen. Die meisten dieser Simulationen werden mithilfe von Dichtefunktionaltheorie (DFT) durchgeführt, da diese dann ein hohes Maß an Genauigkeit und Vorhersagbarkeit besitzen. Die Beiträge aus solchen Studien umfassen die Charakterisierung von Betriebseigenschaften der Materialien in Batterieanwendungen [2–4] und die Vorhersage neuer Materialien in sogenannten "Screening" Ansätzen [5–8]. Die Anwendung von DFT ist jedoch end verbunden mit einem hohen Rechenaufwandt. Aufgrund dessen, ist die Anwendbarkeit von solchen Studien auf kleinste Modellsysteme beschränkt, welches eine problematische Limitierung für die Untersuchung von Batteriematerialien darstellt. Diese sind häufig von einer starken Unordnung bestimmt, welche in den kleinen Modellsystemen deutlich vereinfacht werden muss. Aus diesem Grund werden oft vergröberte Methoden verwendet, welche die Behandlung größerer atomarer Strukturen erlaubt. In heutigen Studien werden dafür z.B. Cluster Expansion, kinetisches Monte-Carlo oder Perkolationsmodelle verwendet [4, 9, 10]. Diese Verfahren nutzen dabei Informationen aus DFT Rechnungen und ermöglichen dadurch eine extrapolierte Auswertung der relevanten Materialeigenschaften. Ein entscheidender Nachteil der vergröberten Methoden ist allerdings die Reduzierung der atomaren Freiheitsgrade. Diese sind jedoch entscheidend für eine akkurate Beschreibung von Effekten, die durch Unordnung entstehen.

In dieser Dissertation werden daher Simulationsansätze für verschiedene Stoffklassen erarbeitet, welche DFT-validierte oder -parametrisierte Kraftfeldpotentiale verwenden. Mit diesen können große atomare Strukturen behandelt werden, wobei die notwendigen Freiheitsgrade erhalten bleiben. Die Kraftfeldpotentiale werden in eine Simulationsstrategie integriert, welche auf einer Kombination von Monte-Carlo und/oder Molekulardynamik-Simulationen basiert.

Mithilfe des beschriebenen Ansatzes werden einschlägige Auswirkungen der Unordnung auf die Leistung von zwei angewandten Batteriematerialien aufgedeckt. Hierbei sind neue, durch Unordnung stabilisierte, Defekte in dem Anodenmaterial $Li_4Ti_5O_{12}$ (LTO) gefunden worden, welche eine hohe lokalisierte Ionenmobilität ermöglichen. Diese wiederum gibt eine Erklärung für die bisher nicht verstandene hohe Ratenkapazität [1], welche in DFT Studien [11, 12] bislang nicht aufgedeckt wurde. Des Weiteren werden Li-Transferzahlen weniger eins in dem glasartig-amorphen Festkörperelektrolyten Li_3OCl vorhergesagt. Aufgrund dessen, kann eine leistungslimitierende Konzentrationspolarisation angenommen werden. Diese beiden Beispiele demonstrieren die Bedeutung von Zusammenhängen in Batteriematerialien, welche durch Unordnung induziert werden können. Letztere sind jedoch nur auf großen Längen- und Zeitskalen in Simulationen erkennbar. Daraus folgt, dass die in dieser Dissertation vorgestellte Simulationsstrategie eine mögliche Route für die Untersuchung von Unordungseffekten in weiteren Materialien vorgibt. Durch diese kann ein tieferes Verständnis von Transportphänomenen in Materialien erarbeitet werden. Hieraus entstehende Einsichten, welche für das Design neuer Materialien entscheidend sein können.

Contents

List of Abbreviations

AIMD	*ab initio* molecular dyamics	**MC**	Monte-Carlo
cDOS	configurational density of states	**MD**	molecular dynamics
COM	center of mass	**MSD**	mean square displacement
DEA	differential evolution algorithm	**NEB**	nudged-elastic-band
DFT	density functional theory	**PES**	potential energy surface
DOF	degrees of freedom	**PSO**	particle swarm optimization
GA	genetic algorithm	**RDF**	radial distribution function
GK	Green-Kubo	**VACF**	velocity autocorrelation function

1 Introduction

The relevance of structural disorder in materials has been recognized for many applications of great technological value. Examples range from atomic scale doping of semiconductors in microelectronics [13] to nanoscale disorder in solar cell materials [14]. Desirable material properties may also be specifically engineered by exploiting disorder. Prominent such representatives are mechanical properties in the rich chemistry of alloys [15] and transport properties in crystalline and amorphous materials [16].

Not surprisingly, disorder also plays a major role in battery materials. On the device scale, cathode or anode are prepared by immersing particles in a binding agent whereby a high degree of randomization is introduced. Favorable Li ion transport results from the cross-linked network between the particles which exhibit a fast uptake by a maximized surface area [17, 18]. On the atomic scale, disorder is ever present during battery charging and discharging. This is due to the lithiation process that leads to a phase transition in which chaotic structural arrangements can be expected [9]. Furthermore, many of the as-prepared materials exhibit inherent or coerced atomic disorder which facilitates ion conduction or intercalation properties. With the exception of the original layered cathode material LCO ($LiCoO_2$) which exhibits a strict symmetry, most attempts for improvement either suffer from or benefit from occupational disorder. For example, the full replacement of Co with Ni or Mn yields LNO ($LiNiO_2$) and layered-LMO ($LiMnO_2$), where the high symmetry is not sustained and leads to performance limiting cation exchange. In contrast, the systematic introduction of occupational disorder into the transition metal layers can produce high-performance cathode materials such as the commercialized NCA ($LiNi_{0.8}Co_{0.15}Al_{0.05}O_2$) and NMC ($LiNi_{0.33}Co_{0.33}Mn_{0.33}O_2$). Alternative classes of cathode materials, like spinel-LMO ($LiMn_2O_4$) or polyanionic compounds like LFP ($LiFePO_4$), are subject to doping strategies in order to introduce disorder [3, 19]. Similarly, strong disorder is also found in anode materials. Carbon and silicon based materials exhibit highly irregular structures based on an omnipresent nanostructuring that is necessary for reasonable performance. Another example is the crystalline material LTO. An increased Li content during synthesis yields the occupationally disordered $Li_4Ti_5O_{12}$ instead of the pure spinel $LiTi_2O_4$. The introduced disorder thereby enhances the material performance profoundly [18]. Electrolytes follow the same principles. The liquid representatives exhibit high ion mobility based on the chaotic structures in the aggregate state. In solid state electrolytes a similar degree of disorder needs to be maintained to reproduce equally high ion mobility. Here, amorphous materials like LiPON or crystals with strong occupational disorder as found in the garnet LLZO ($Li_7La_3Zr_2O_{12}$) and the perovskite LLTO ($Li_{3x}La_{2/3-x}TiO$) are employed [20–22]. Consequently, glass-ceramics, which are mixed amorphous and crystalline compounds, like $Li_7P_3S_{11}$ are equally suitable [23]. In light of the general presence of disorder, an understanding of its impact on material properties will thus aid in the pursuit of better performing battery materials.

Computer simulations can provide most detailed insight into such structures at the microscopic level. For simulating battery materials in particular, a large number of different methods have been applied over the years to e.g. explore atomic structures or ongoing dynamical processes. These methods offer different levels of chemical accuracy which generally tend to scale with computational cost. This yields a reciprocal relationship between accuracy versus the length and time scales accessible via simulation, as illustrated in Fig. 1.1. The highest level of accuracy is provided by first-principles, or so-called *ab initio*, electronic structure methods. Based on the fundamental laws of quantum mechanics, these exhibit strong predictive power and can provide a most accurate description of atomic energies and forces. It is therefore not surprising that *ab initio* methods, with density functional theory (DFT) as the most prominent example, have found great popularity in battery materials research [24, 25]. For example, DFT has formed the basis for numerous screening studies. Here, specific performance indicators are examined independently in an attempt to either discover new materials or derive structural design principles [4–8, 26]. As already indicated, however, this predictive power comes at a considerable computational cost. The latter scales as N^3-N^{10}, where N is the number of electrons, depending on the employed approximations [27]. This presently prohibits their application to system sizes beyond a few hundred atoms. While this may suffice for high symmetry bulk and surface models within periodic boundary conditions [28, 29], it becomes a showstopper for applications to extended, disordered systems. Similarly, achievable time scales for example in molecular dynamics (MD) simulations are limited to few hundred picoseconds, i.e. a time scale that is statistically insufficient for sampling rare molecular events [30].

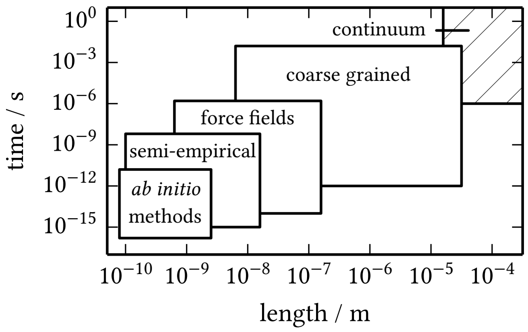

Fig. 1.1: Schematic representation of the accessibility of length and time scales with different computational methods (see text).

It is thus highly desirable to reduce the computational cost for accessing larger length and time scales, while still retaining atomic-scale resolution. In this respect, the use of parameterized effective models is particularly attractive. Here, parameterization can enter either in the solution to many-body electron integrals (semi-empirical electronic structure), atomic interactions (force field potentials), or the description of coarse grained (lattice Monte-Carlo, cluster expansion) and mean field models [27, 30, 31]. Also in battery materials research such methods have been applied. Based on DFT input, for example, cluster expansion allows for the extrapolation to larger length scales and e.g. investigate the thermodynamic phase stability of intercalated compounds. Similarly, kinetic Monte-Carlo allows for accessing longer time scales e.g. in order to study macroscopic diffusion [2, 3, 9, 25, 32]. Alternatively, one may use classical interatomic, or force field, potentials. The favorable numerical efficiency of the latter offers an enormous advantage for simulating both extended length and time scales. In battery applications, force fields have previously been used to e.g. study selected defect formation energies or investigate Li ion mobility via MD simulations in order to extract macroscopic diffusion coefficients [24, 25]. Overall, the effective nature of the aforementioned models also constitutes their major weakness as it restricts their application to the specific physical problem for which they have been parameterized. Other drawbacks include the limited predictability and ease of application since these models depend crucially on input data and require a rather involved parameterization process.

If wishing to go one level further to even larger (macroscopic) length and time scales, one must resort to continuum methods (see Fig. 1.1). Here, atomic resolution is lost since the smallest entities considered are grains and effective flows. These methods typically rely on many approximations and effective ensemble properties [33]. Hence, they are most appropriately applied to the device scale and will not be further discussed here.

In this thesis potential effects of disorder on battery materials are investigated. The employed computational models and methods are uniquely combined to offer a most detailed representation of both thermodynamics and kinetics, while bridging the gap between the micro- and the mesoscale. Specifically, the configurational entropy resulting from disorder is a central property which needs to be adequately captured. Here, rigorous statistics are necessary to obtain representative structural ensembles as created for example via Monte-Carlo sampling approaches. Accordingly, the evaluation of materials properties at operating temperatures needs to include enough thermal averaging which is most suitably performed via MD simulations. For these tasks large model systems have to be employed to depict atomic relaxation and correlation effects. The attempted strategy involves many calculations for large system sizes which cannot be conducted using *ab initio* methods due to the prohibitive computational cost. Coarse-grained approaches are also excluded on the basis of explicitly including all atomic degrees of freedom (DOF). Thus, parameterized force field potentials are the optimal method of choice for the present purposes. These yield an increased computational efficiency by a factor of ca. 10^4 compared to other potentially more accurate semi-empirical methods (such as tight-binding DFT) or machine learning approaches [34]. To retain sufficient accuracy, the employed force field potentials are validated or trained using DFT, following a bottom-up multiscale methodology.

The involved basic theory is presented in chapter 2 followed by the hereby newly combined and developed methods in chapter 3. The derived methodology is applied to two systems of particular technological relevance: The crystalline anode material LTO ($Li_4Ti_5O_{12}$) which is presented in chapter 4 and the solid state electrolyte Li_3OCl in its glass-amorphous phase as presented in chapter 5. Finally, chapter 6 presents a comprehensive summary of the results, along with the drawn conclusions and outlook for future directions.

2 Theoretical background

The approach employed in this thesis follows a multiscale methodology. The investigation of disorder at large length and time scales is conducted using force field potentials. These are parameterized and validated with high-level electronic structure calculations based on density functional theory (DFT). Both approaches represent total energy methods which associate an energy with the structural degrees of freedom (DOF) in a chemical system, as described through the so-called potential energy surface (PES). The behavior of a system under the influence of temperature can be investigated on basis of the PES via molecular dynamics (MD) which is a applied throughout this work. The fundamental theory relevant for these methods is presented in this chapter.

2.1 Density Functional Theory

In computer simulations for materials research, DFT is presently the most frequently applied electronic structure method. This is due to the very favorable, for many applications, balance between accuracy and computational efficiency. The advantage of relying on the electron density as the central quantity lies in the reduced DOF which need to be treated in comparison to e.g. wavefunction based methods. From this follows a favorable system size scaling. In the following the basics of concepts behind DFT are briefly introduced. Naturally, a plethora of basic literature exists which shall be referred to for a more detailed description [27, 31, 35].

2.1.1 Hohenberg-Kohn theorems

In electronic structure methods the fundamental energetic contributions in atomic systems are treated. These consist of the interactions among and the momenta of the electrons and nuclei. Explicitly included are the kinetic energy of the electrons T_e and nuclei T_n as well as the electron-electron V_{ee}, nuclei-nuclei V_{nn} and nuclei-electron V_{ne} interactions. When the mass difference between electrons and protons is considered ($m_e \ll m_p$), the electron motion can often be assumed as quasi instantaneous. This allows for a timescale separation. Subsequently, the nuclei can be regarded as static and the terms which only depend on the nuclear positions, T_n and V_{nn}, can be omitted. This simplification is the adiabatic Born-Oppenheimer (B.O.) approximation, which is valid in most cases. It follows for the total energy

$$E_{\mathrm{tot}} = T_{\mathrm{e}} + T_{\mathrm{n}} + V_{\mathrm{ee}} + V_{\mathrm{nn}} + V_{\mathrm{ne}} \xrightarrow{\text{B.O.}} E_{\mathrm{tot,el}} = T_{\mathrm{e}} + V_{\mathrm{ee}} + V_{\mathrm{ne}}. \tag{2.1}$$

The resulting expression thus represents the electrons interacting within an external potential constituted by the nuclei [27, 31].

In DFT, the electrons are represented as a density $\rho(r)$ comprising the mapping of the electron positions within an external potential. Here, only one unique density leads to an energy minimum (to which every system strives). Henceforth, there is a unique density representation ρ_0 of the ground state energy E_0 and in principle its wavefunction. These statements are the first and second Hohenberg-Kohn theorem [36] which also suggest that a solution to an external potential is unambiguous complying with the variation principle

$$E_0 = E\left[\rho_0(r)\right] < E[\rho_{\text{trial}}]. \tag{2.2}$$

Following this, any energy defined by a trial density ρ_{trial} cannot give a better solution than that obtained from ρ_0. This is analogous to wavefunction based methods were a self-consistent solution strategy is followed in order to obtain a suitable representation of the true wavefunction Ψ_0. Such an approach is possible since the corresponding Hamilton operator, which contains all energy operations in a system, is clearly defined. In contrast to the latter, in DFT the non-linear functional for the electron density is not known. Thus a straightforward variation of ρ in a self-consistent manner to obtain ρ_0 cannot be performed. Instead the different contributions to the total energy are split into known and unknown functionals of ρ

$$E_{\text{tot}} = \underbrace{T_{\text{e}}[\rho(r)] + V_{\text{ee}}[\rho(r)] + V_{\text{ne}}[\rho(r)]}_{\text{known}} + \underbrace{V_{\text{xc}}[\rho(r)]}_{\text{unknown}}. \tag{2.3}$$

where $T_{\text{e}}[\rho(r)]$ corresponds to the non-interacting kinetic energy, $V_{\text{ee}}[\rho(r)]$, and $V_{\text{ne}}[\rho(r)]$ to the known classical interactions and $V_{\text{xc}}[\rho(r)]$ is the so-called exchange-correlation functional which contains everything unknown [35].

2.1.2 Kohn-Sham Approach

The general solution strategy in the Kohn-Sham approach is based on a non-interacting reference system. Here, the single electron wavefunctions ϕ_i combine to the real ground state density ρ_0 as

$$\sum_i^N |\phi_i|^2 = \rho_0. \tag{2.4}$$

Minimization of Eq. 2.3 with respect to the ϕ_i then yields an eigenvalue problem known as the Kohn-Sham equations

$$\left(-\frac{\hbar\nabla_i^2}{2m_e} + \hat{V}_{\text{eff}}\right)\phi_i = \epsilon_i\phi_i \quad \text{with} \quad \hat{V}_{\text{eff}} = \int \frac{\rho(r')}{||r-r'||}dr' + \sum_{k=1}^{M} \frac{-z_k}{||r-R_k||} + V_{\text{xc}} \tag{2.5}$$

where $-\frac{\hbar\nabla_i^2}{2m_e}$ is the operator for the kinetic energy of the non-interacting reference electrons and V_{eff} is the effective potential combining the classical and exchange-correlation potential. V_{eff} consists of the Coulomb interaction of each single electron density with the mean-field $\rho(r')$ formed by the other electrons, the Coulomb interaction of the single electron density with the M nuclei of charge z_k and the potential V_{xc} of the unknown exchange-correlation functional. Eq. 2.5 can be solved in a self-consistent field approach. It should be noted, that the here resulting single electron densities are not equivalent to molecular orbitals, although they turn out quite similar in shape and energy [35].

2.1.3 Exchange-correlation approximation

In the Kohn-Sham approach presented above the total electron energy is split into known and unknown contributions. In the former the classic Coulomb interactions and the kinetic energy of the non-interacting reference system cover the largest part of the total energy. Thus, the unknown exchange-correlation functional only needs to approximate a small portion of the energy. This contribution is however decisive for the chemical accuracy and involves rigorous physical effects originating in the missing static exchange and dynamic correlation [27, 31, 35].

The exact form of the exchange-correlation functional is not known and likely never will be [37]. For this reason, many approximate functionals have been developed which can be categorized in rungs according to their approximation strategy [27]:

LDA The local density approximation functional is based on the density at a point in space. For each point the according exact exchange-correlation from a corresponding homogeneous electron gas of equal density is taken. This approximation works fairly well for systems with slowly varying densities such as metals.

GGA The generalized gradient approximation adds information about the gradient of the electron density. Thus it is suitable to describe inhomogeneous systems.

meta-GGA meta-GGA functionals include even higher order derivatives into the exchange-correlation. From this, only minor improvement is often gained in comparison to GGA for which reason their application is rather rare.

hybrid In hybrid functionals the exact exchange as known from Hartree-Fock theory is calculated for the Kohn-Sham reference system and mixed into LDA and GGA expressions. This includes non-local contributions and leads to a strong reduction of the self-interaction error at the cost of significantly increased computational demand.

Further improvements or approximations may additionally be added. Universally applicable to all functionals are parameterized or self-consistent methods to correct for missing van der Waals interactions which are usually badly described using semi local DFT exchange correlation functionals.

2.2 Force Field Potentials

Classical force field potentials use physically motivated analytical expressions which are parameterized to effectively describe interactions between particles in a chemical system [27]. Here, the explicit treatment of electrons and the involved complex quantum mechanical terms are avoided which reduces computational cost significantly. The resulting force field expressions can be optimized to yield high parallel efficiency ensuring linear scaling of computational cost with number of atoms. Thus, the treatment of millions of atoms is possible and simulation times are accessible which are long enough to sample kinetic processes with statistical reliability [34].

The accuracy and predictability of a force field potential depends on its parameterization and usually requires careful validation. Furthermore, the transferability of parameters from one system to another relates to the generality of the parameterization strategy and the involved force field expressions. It needs to be stressed that force fields can only reproduce non-electronic attributes which depend on the included physics. Using only basic interaction terms thereby limits to the thermodynamics and kinetics of transport and mechanical properties. Including specialized potential terms, additional higher level information can be effectively included. Examples entail optical, magnetic, oxidation state and solvation properties as well as bond breaking and formation [27, 31, 34].

In literature, a multitude of force fields can be found where each is designed to describe a specific class of material. The most prominent type are molecular mechanics force fields which are used for organic systems and find most application in biology or polymer research. These explicitly include terms describing covalent bonds with a specified hybridization as well as the resulting dependencies on bond angles, dihedrals and out-of-plane deformations. The involved analytic terms are intuitive and can be parametrized in a straight-forward fashion [38]. In contrast to this, interactions in bulk materials like solids are less clearly categorizable and respective force fields vary quite significantly. The simplest potentials follow the Born model of solids (as described in Sec. 2.2.1) which depends solely on pair-wise interactions and perform quite accurately for ionic and van der Waals systems [39]. For covalent or metallic solids, manybody potentials are necessary [34]. Hereby, the most successful force fields include the (modified) Embedded Atom Model (EAM and MEAM) for metals [40–42] and the Tersoff [43] and bond order potential (BOP) [44] for covalent solids (e.g. Silicon). In order to extend force fields to yield accurate and variable oxidation states variable charge force fields have recently emerged. These are needed for a reliable description of e.g. transition metal oxides and interfaces. Popular examples include the reactive force field ReaxFF [45] and the charge optimized many body potential (COMB) [46].

2.2.1 Born Model of Solids

Following the Born model of solids [39], an ionic compound presents a saturated system where each ion holds a full valence shell. In contrast to unsaturated compounds where atoms form covalent bonds with a strong directionality, interactions in saturated systems are isotropic and can be described via two-body terms. For an ionic solid, these specifically consist of the ionic Coulomb potential, the van der Waals interactions, and repulsive short range interactions due to Pauli repulsion [39].

In the case of the well-known Coulomb potential, its reciprocal decay in distance r between two charges q_i with the relation $E \propto \frac{q_i q_j}{r}$ needs special consideration when treating crystals. Here, the infinitely extended ionic lattice creates an effective background potential which has to be included via a correction. Either the lattice specific Madelung constant can be introduced as a proportionality factor α_M ($E \propto \alpha_M \frac{q_i q_j}{r}$) or a long range correction like the Ewald method or the Particle-Particle Particle Mesh (pppm) formalism can be applied [29, 47, 48].

The van der Waals interactions originate from fluctuating dipoles in the charge cloud of an atom. These can be derived from the polarizability dependence of the isotropically averaged second order energy yielding the so-called London interactions. The latter have a fast decaying $\frac{C}{r^6}$ dependence of the ion eigen energies Δ_i and ion polarizabilities α_i with $C = -\frac{2}{3}\frac{\Delta_1\Delta_2}{\Delta_1+\Delta_2}\alpha_1\alpha_2$. With the approximation of Δ_i as the ionization potentials the interaction potential has a well defined and parameter-free analytical form. It should be noted that these induced dipole interactions in non-ionic systems are fairly strong and cumulatively exceed that of permanent dipoles due their isotropy [39].

Compared to the Coulomb and van der Waals interactions, the short range repulsion has no simple analytical representation and is therefore heuristically approximated with a $\frac{b}{r^n}$ (Lenard-Jones) or $A \exp -\frac{r}{\rho}$ (Buckingham) potential [39]. The exponential expression is thereby known to reproduce quantum mechanical behavior more accurately. It, however, suffers from instabilities at very small r which could occur in “bad” simulations, e.g. molecular dynamics simulations with too large time steps [38]. The overall energy of an ionic system, following the Born model of solids, is thus often expressed including a Buckingham repulsion such that

$$U_{ij} = \frac{1}{4\pi\epsilon_0}\frac{q_i q_j}{r_{ij}} + A_{ij}\exp\left(-\frac{r_{ij}}{\rho_{ij}}\right) - \frac{C_{ij}}{r_{ij}^6} \tag{2.6}$$

where ϵ_0 corresponds to the dielectric constant in vacuum, r_{ij} to the ion distance, q_i are the ion charges, and A_{ij}, ρ_{ij}, C_{ij} are parameters for the short-range interactions.

Although defined for systems with pure ionic or/and van der Waals interactions, the potential following Eq. 2.6 is often employed for compounds which include some covalency. This is possible since in practice, the parameters A_{ij}, ρ_{ij}, C_{ij} are fitted to reproduce reference data and not directly derived from quantum chemical calculations. Hereby, the parameter C_{ij} of the London interaction is often non-correspondent to its physical meaning since it additionally accounts for weak covalent interactions. This way, good-quality potentials have been parameterized for a wide range of oxides, halogenides, and even polyanionic solids such as phosphates and silicates. For the latter an angular dependent term is often added to reproduce the correct geometry of the polyanion [24, 49, 50]. The originally intended choice for q_i in ionic systems are formal charges. However, these are often replaced with fractional charges which physically correspond to a mean static polarization of an ion. This is motivated by the fact that formal charges present an extremum compared to charge partitioning schemes in *ab initio* calculations (which are also not uniquely defined) [38]. Using fractional charges usually yields better results but makes force fields less transferable as an environment dependent polarization is included.

2.2.2 Polarizability via the core/shell model

In order to extend the Born model of solids, the electronic polarizability α can be added to improve the description of bulk properties. The latter include phonon dynamics, elastic properties, defect and reorganization energies, as well as ion diffusion [51–53]. A simple effective example for such an extension is the core/shell model by Dick and Overhauser [54]. This method is motivated by findings that the electric response to an electrostatic environment corresponds to the deformation of the outer electronic shell [55, 56]. Therefore, the latter is explicitly mimicked by adding a pseudoparticle which is attached to the original ion. It follows, that ions previously described by one point charge are now split into two particles, each carrying a fraction of the original charge (see Fig. 2.1). The only interaction between such a core/shell pair is a restoring harmonic spring force

$$U_{\text{c-s}} = \frac{1}{2}k r_{\text{c-s}}^2 \tag{2.7}$$

where $r_{\text{c-s}}$ represents the core/shell distance and k is the force constant. This interaction corresponds to the harmonic response of the ionic polarization α according to the created dipole $p = q_{\text{s}} r_{\text{c-s}}$ where q_{s} is the shell charge or the charge split respectively. The created dipole p is then given as

$$p = q_{\text{s}} r_{\text{c-s}} = \alpha E \tag{2.8}$$

where E is the induced electric field. Multiplying Eq. 2.8 with the charge q_s yields an expression for the induced force F

$$q_\mathrm{s}^2 r_\text{c-s} = \alpha E q_\mathrm{s} = \alpha F \tag{2.9}$$

inserting the harmonic force $F_\text{c-s} = k r_\text{c-s}$ then yields an expression for the polarizability only depending on the shell parameters q_s and k

$$\alpha = \frac{q_\mathrm{s}^2}{k}. \tag{2.10}$$

In a simulation the effect of the polarizability manifests itself by the Coulomb interactions of each the core and shell with the other ions consisting either of point charges or again core/shell pairs. Hereby, a polarized core/shell pair ($r \neq 0$) yields a combined Coulomb interaction which differs from that of the original point charge. In the resulting model, van der Waals interaction and the short-range repulse are only assumed to act between shells as a simplification (see Fig. 2.1). The introduced error of this approximation scales with the difference of the core/shell separation $r^i_\text{c-s} - r^j_\text{c-s}$ of two core/shell pairs i and j which is negligibly small [54].

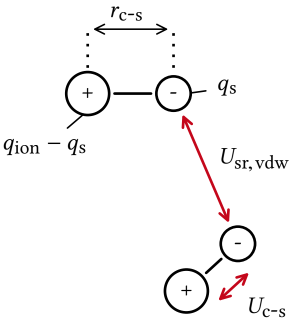

Fig. 2.1: Schematic of the core/shell model. Two core/shell pairs are shown with the positive core carrying the resulting charge $q_\text{ion} - q_\mathrm{s}$ and a negative shell carrying the charge q_s indicated by a "+" and "-", respectively. The internal core/shell interaction $U_\text{c-s}$ acting over the core/shell separation $r_\text{c-s}$ is indicated. Additionally, the short-range repulsion and van der Waals interactions which are only acting between shells are labeled as $U_\text{sr, vdw}$. It should be noted that the Coulomb interactions act between all charges of different core/shell pairs.

Overall the core/shell model has demonstrated considerable quantitative success. An extension to the simple core/shell model has been developed by adding a finite ionic radius instead of an explicit shell particle for an isotropic interaction with the environment. This amendment, called the breathing shell model, further refines phonon spectra and improves elastic properties at 0 K. It thereby specifically cures a cauchy violation for symmetric (fcc) crystals where the core/shell model yields the same elastic constants for transverse and shear relations ($C_{12} = C_{44}$) [52].

2.3 Molecular Dynamics Simulations

In MD simulations, dynamic properties of a system are computed from the statistics observed during its temporal evolution. For this, an atomistic model is propagated in time following classical mechanics i.e. Newton's equation of motion. Temperature and pressure effects are explicitly included which is very useful to study for example the operational behavior of battery materials. In the following, fundamental aspects relevant in this thesis are elaborated.

2.3.1 Integrating the equations of motion

To determine particle trajectories in atomistic simulations, the equations of motion need to be integrated in time. The required information about the change in momentum at a point of time is readily obtained from the positions of and forces on the particles (e.g. taken from DFT or force field calculations). For the integration, a time step is chosen as large as possible to reduce computational cost but small enough to resolve the particle motion with a high accuracy. In regard to the latter, any finite time step will still lead to small errors accumulating over the course of the simulation. These errors need to be compensated by a robust integration scheme which approximates the involved differential equation $(m(\partial^2 x(t)/\partial t^2) = F(x(t)))$ accurately. For this, different algorithms exist which offer varying advantages and disadvantages [29].

In general, the finite time step as well as the numerical imprecision make the simulation of a "true" trajectory defined by the initial atomic configuration impossible. In practice this presents no drawback however. There is sufficient evidence, that the effective trajectory an MD simulation yields, provides an adequate representation of the correct behavior of the statistical ensemble. In that, the numerical trajectory is close to the "shadow" orbit of the "true" trajectory [29]. Nevertheless, certain issues regarding this accuracy need to be considered in choosing an appropriate algorithm for the time integration. A most important indicator for the accuracy is the conservation of energy or effective energy, respectively, depending on the treated ensemble [57]. An algorithm needs to ensure this despite numerical errors which easily arise due to integration imprecisions. Here, one usually distinguishes between a short term and long term energy drift, where the former and latter do not necessarily correlate. Another factor is time reversibility, i.e. recovering the forward and backward particle movement when reversing time. This depends on the time symmetry of the algorithm, reflected in the approximate gradient during the integration procedure. In principle, this characteristic should be fulfilled in order to comply with Newton's equations of motion which are symmetric in time. Lastly, a more abstract concern is the phase space volume conservation, meaning the ability of an integration scheme to maintain a meaningful statistical ensemble over the course of a trajectory [29].

To achieve an accurate approximation, the velocity $v(t)$ and the momentum change via the force $f(t)$ at a point in time t and at a position $r(t)$ can be symmetrically approximated for a time step Δt. Hence, the movements to and from the position $r(t)$ are simultaneously considered. Two Taylor expansions are thus formulated as

$$r(t+\Delta t) = r(t) + v(t)\Delta t + \frac{f(t)}{2m}\Delta t^2 + \frac{\Delta t^3}{3!}\frac{d^3 r}{dt^3} + \mathcal{O}(\Delta t^4) \tag{2.11}$$

$$r(t-\Delta t) = r(t) - v(t)\Delta t + \frac{f(t)}{2m}\Delta t^2 - \frac{\Delta t^3}{3!}\frac{d^3 r}{dt^3} + \mathcal{O}(\Delta t^4) \tag{2.12}$$

where (Δt^4) represents the expansion term to fourth order. To obtain the resulting particle movement both terms in Eq. 2.11 are added. Here, terms with an uneven power in Δt which are opposite in sign cancel each other

$$r(t+\Delta t) + r(t-\Delta t) = 2r(t) + \frac{f(t)}{m}\Delta t^2 + \mathcal{O}(\Delta t^4). \tag{2.13}$$

This can be rearranged to

$$r(t+\Delta t) \approx 2r(t) - r(t-\Delta t) + \frac{f(t)}{m}\Delta t^2 \tag{2.14}$$

where the forth order expansion term is omitted and expressed as an error in the order of Δt^4. Eq. 2.14 introduces the Verlet algorithm which presents a fairly robust integration scheme. It thereby yields long term energy conservation, time reversibility and phase space conservation when using a sufficiently small Δt. On short timescales, the energy fluctuation, however, is not ideal. Nevertheless, this algorithm and its derivatives are most frequently applied. From the formulation in Eq. 2.14 it can be seen, that the velocity is not explicitly included. It can be calculated in an extra step, which yields a comparatively large error on the order of Δt^2. An alternative formulation which explicitly includes the velocity and is equivalent to Eq. 2.14 is the so-called velocity Verlet algorithm. This is given as

$$r(t+\Delta t) = r(t) + v(t)\Delta t + \frac{f(t)}{2m}\Delta t^2 \quad \text{with} \tag{2.15}$$

$$v(t+\Delta t) = v(t) + \frac{f(t+\Delta t) + f(t)}{2m}\Delta t. \tag{2.16}$$

It can be seen, that the velocity is still determined in an extra step. However, being directly included in the integration scheme, it is equivalent in accuracy [29]. A half-step variant of the velocity Verlet algorithm is implemented in the software LAMMPS [58] which is exclusively used in this thesis.

An alternative to Verlet type algorithms are higher order algorithms. As the name suggests, these include higher order terms of the Taylor expansion. For their evaluation, more derivatives need to be stored and computed involving a higher computational cost. Additionally, they often are not time reversible and phase space conserving [29]. Notwithstanding, they offer superior short term energy conservation which allows for larger time steps. In the case of MD simulations which are based on high level theory i.e. electronic structure, they might provide a more economic time integration scheme. Here, the disadvantages concerning long term energy and phase conservation are not relevant on the targeted short timescales. A popular example of such a higher order scheme is the predictor-corrector method [28, 29].

2.3.2 Thermostats

Newton's equations of motion solved in an MD simulation with constant volume and number of particles as described above in Sec. 2.3.1 correspond to the description of a microcanonical (NVE) ensemble. Experimental conditions, however, usually imply a constant temperature and pressure corresponding to an NPT or an NVT ensemble at the respective variable volume. In order to realize this situation in a simulation, thermostats and barostats may be used.

Temperature in an NVE simulation

In order to evaluate the applicability of an NVE ensemble to reproduce experimental conditions, the temperature fluctuations during a simulation can be estimated. Naturally, those fluctuations need to be as small as possible to mimic a constant temperature. An estimate can be made by considering the relative variance of the kinetic energy per particle. This directly corresponds to the second and forth moments of the Maxwell-Boltzmann distribution. A fixed expression can thus be derived to [29]

$$\frac{\sigma^2_{p^2}}{\langle p^2 \rangle^2} = \frac{\langle p^4 \rangle - \langle p^2 \rangle^2}{\langle p^2 \rangle^2} = \frac{2}{3} \tag{2.17}$$

where p is the particle momentum and σ_{p^2} the variance of its second moment. This quantity can be related to the relative fluctuation of the instantaneous temperature $\mathcal{T}$

$$\frac{\sigma^2_{\mathcal{T}}}{\langle \mathcal{T} \rangle^2_{NVT}} = \frac{2}{3N}. \tag{2.18}$$

The final expression scales with the number of particles. Therefore, it can be concluded, that an NVE simulation only adequately reproduces a constant temperature ensemble, if a large number of particles is explicitly treated. Since this is not always possible, a simulation might be directly performed in the according isothermal canonical (NVT) ensemble [29].

Constant temperature simulations

Different approaches exist to perform MD simulations in NVT ensembles. The basic idea is based on coupling the simulation box to an outer heat bath. According to thermodynamics, both systems will establish thermal equilibrium. In that, the heat bath can be assumed infinitely large or equivalently constant in temperature, thus imposing said temperature on the simulation [28].

One class of approaches is based on stochastic collisions of particles in the simulation with an external fictitious heat bath. Most noticeable such methods are the Andersen and Langevin thermostat. The former includes a simple formulation only based on random collisions following a time probability function to mimic the influence of a heat bath. More involved is the latter, where the Brownian motion of a heat bath is implicitly modeled. Hereby, the equations of motion are extended via a constant friction in combination with a collision term following a gaussian distribution which exerts a fluctuating (white-noise) force. Both approaches create configurations corresponding to a canonical distribution which include valid potential energy or pressure values independent of the specified collision rate constants. In comparison to that, the dynamic behavior, i.e. any parameters dependent on time, are less well reproduced. Here, the random forces influence the particle motion significantly which then deviate from a realistic behavoir. In the Anderson thermostat, only very narrow ranges of the collision rate allow for undisturbed particle dynamics. Less pronounced in the Langevin thermostat, such a behavior can still occur if collision rate parameters are not carefully chosen [28, 29].

A more elaborated class of approaches aims at deriving the equations of motion by incorporating the heat bath degrees of freedom deterministically into the Hamiltonian of the simulation. From this follows a new set of equations of motion which conserve an effective energy encompassing the particles in the simulation and the heat bath. This way, a thermal equilibrium results which gives a constant temperature. The original formulation by Nosé, later amended by Hoover, adds a set of explicit heat bath coordinates s which couple to the simulation of N particles with an effective mass Q. The original Hamiltonian, consisting of the kinetic energy contribution $\frac{p_i^2}{2m_i}$ of each particle i as well as of the potential energy of the system $U_{\text{pot}}(r^N)$, then changes from

$$\mathcal{H}_{NVE} = \sum_{i=1}^{N} \frac{p_i^2}{2m_i} + U_{\text{pot}}(r^N) \tag{2.19}$$

to the amended form

$$\mathcal{H}_{\text{Nose-Hoover}} = \sum_{i=1}^{N} \frac{p_i^2}{2m_i} + U_{\text{pot}}(r^N) + \frac{\zeta^2 Q}{2} + 3N \ln(s) k_B T \tag{2.20}$$

where k_B is the Boltzmann constant, T is the target temperature and ζ is a simplification added by Hoover representing a thermodynamic friction $\zeta = s' p_s' / Q$ with p_s' as the momentum of the heat bath. In this formulation, Q determines the coupling strength of the heat bath to the simulation and needs to be specified. In deriving a practical expression for an implementation, it is found that s acts as a scaling factor of the time step according to friction imposed by the heat bath. In general, it is difficult to incorporate s into the usual formulations since its coordinate system is undefined. For this reason, the Nose-Hoover style thermostats are expressed in a Lagrangian form which derives from the variation principle balancing potential and kinetic energy [28, 29].

Nose-Hoover Chains

The above described Nose-Hoover thermostat formally creates a correct canonical ensemble if the center of mass (COM) of the system is fixed and no external force acts on the cell. Even if these premises are violated, any deviation from a correct distribution is usually negligible. Nevertheless, in some cases the explored phase space might be compromised which means that a non-ergodic behavior is found. This may lead to a strong correlation of dynamic variables, e.g. of the diffusion coefficients. It should be noted that these coupling effects cannot occur in the alternative stochastic approaches which however suffer from other disadvantages [29].

The reason for the inherent dynamic correlation lies in the inclusion of a single dynamic variable ζ in the Nose-Hoover formulation. In its formulation not only the energy but also another more abstract property is conserved. This can be remedied by the usage of so-called Nose-Hoover chains where more thermostats are coupled to the original one including several ζ_k. In these, more abstract properties are conserved which in turn decouple the system again [29]. The additional computational cost is negligible and it thus presents the standard implementation in most MD codes. This is also true for the LAMMPS simulation package [58] employed in this thesis, where by default 3 thermostats are coupled.

Constant pressure simulations

If the density/volume of a system is unknown, it is worthwhile to perform simulations at the experimentally equivalent NPT ensemble. For this, a barostat may be added which alters the dimension of the simulation cell on the fly. An ensemble is created this way allowing for an automatic equilibration of the system to experimental conditions.

A simple approach is given in the rescaling of the system volume depending on the pressure. Such a term can be added into the equations of motion where a prominent example is the Berendsen barostat. A coupling to a pressure bath which determines the rescaling of the cell dimensions χ is formulated. This is based on the difference of the instantaneous pressure $\mathcal{P}$ to the target pressure P_{ext} as

$$\chi = 1 - \kappa_T \frac{\Delta t}{t_p} (P_{\text{ext}} - \mathcal{P}) \tag{2.21}$$

where κ_T represents the isothermal compressibility, Δt the time step and t_p is a relaxation time for the pressure fluctuations. The resulting distribution based on the simple rescaling is, however, not a canonical one. Thus, this thermostat is rather suitable for a “mild” equilibration of a system before sampling at a determined volume [28].

Following the Nose-Hoover (chain) style thermostats, a deterministic approach is also possible. In that, a Hamiltonian is again amended in combination with the temperature formulation above to derive the according equations of motion. A more rigorous expression follows which includes an effective mass W for the coupling of the volume, and an according momentum p_ϵ based on the change in volume $\epsilon = \ln(V/V_0)$. Interdependencies with the temperature variables s, p_s, Q and ζ arise yielding a Hamiltonian as

$$\mathcal{H}_{\text{Hoover}} = \sum_{i=1}^{N} \frac{p_i^2}{2m_i} + U_{\text{pot}}(r^N) + \frac{p_\zeta^2}{Q} + k_B T \zeta + \frac{p_\epsilon^2}{W} + P_{\text{ext}} V. \tag{2.22}$$

Naturally, for this expression also a chain type barostat can be derived in order to avoid correlation of dynamical properties [28, 29].

In general, the cell shape of a system can also be changed by the usage of a barostat. Here, rescaling occurs corresponding to the deviations of the different pressure tensor components $P_{\alpha\alpha}$ and $P_{\alpha\beta}$.

2.3.3 Adiabatic Core/Shell Model

When performing MD simulations with a polarizable core/shell force field (see section 2.2.2) special considerations have to be taken into account. This is due to the pseudo particles which are introduced to mimic the electron cloud. Physically, the core/shell pairs each represent a single ion which contributes with only three degrees of freedom from the perspective of statistical thermodynamics. Thus, the core/shell spring represents an imaginary or “technical” degree of freedom (DOF).

There are two methods proposed in literature to handle the shell and its imaginary degree of freedom. The “massless” core/shell model by Lindan *et al.* is the first alternative [59]. Here, the shell which represents electrons is considered to have a negligible mass compared to the core representing the nucleus. Thus, the Born-Oppenheimer picture is assumed where the shell relaxes instantaneously to any core configuration. In practice this means that after every MD step the shell positions are relaxed to minimize the forces on the shells. The system is then propagated in time following the resulting forces acting on the cores. Although this model appears intuitive based on the physical motivation, it suffers from a considerable issue in energy conversation. This is due to the fact, that the time integrated forces are discontinuous after the shell relaxation. Even though heuristic approaches to rescale velocities exist, stable simulations are hard to maintain [59].

An alternative method is the so-called “adiabatic” core/shell model by Mitchell and Fincham [53], which is also used in this thesis. Here, the shell is given a fraction of the core’s mass which allows it to be included into the overall propagation scheme. To approximate the instantaneous relaxation of the shell, the difference between the core and shell mass (m_c and m_s, respectively) needs to ensure an oscillation frequency $\nu_{\text{c-s}}$ sufficiently above the atomic vibrations in the simulated system. The required mass fraction can therefore be estimated from the frequency of the harmonic oscillator characterized by the spring constant k

$$\nu_{\text{c-s}} = \frac{1}{2\pi}\sqrt{\frac{\mu}{k}} \qquad \text{with} \qquad \mu = \frac{m_c m_s}{m_c + m_s}. \tag{2.23}$$

In this set-up the imaginary DOF is thus explicitly included in the equations of motion whereby special consideration needs to be taken into account when using a thermostat. In principle, the relative core/shell motion should be at a minimum according to the relaxed shell convention (zero forces on shells) of the massless core/shell model. Therefore, any core/shell motion should only correspond to the polarization as a product of the free response to the electrostatic environment. Following this premise, the system needs to be handled very carefully during initialization and equilibration. Firstly, when assigning initial velocities, no relative motion between the core/shell pairs must be introduced. Secondly, a thermostat must only rescale the COM motion of a core/shell pair, leaving the internal DOF untouched. This results in a quasi adiabatic motion of the core/shell pairs with low thermalization rates which should be monitored. Naturally, some energy is transferred into the imaginary DOF which account for the actual polarization. However, due to its decoupling from the thermostat and the high oscillation frequency of the core/shell pairs, this energy transfer remains minimal. The decoupling of the core/shell motion affects the thermostat to an increased sensitivity to numerical fluctuations. As a result, this can lead to the leakage of momentum into the simulation cell which needs to be corrected. After equilibration, the core/shell oscillators are considered to be in a correct thermalized state, where the oscillation behavior is in accord with the ions' polarization state. At this point, any further non-elastic interaction with neighboring ions unlikely leads to further noticable thermalization of the core/shell motion [53]. Although the original literature is not clear about this, most codes like DLPOLY [60] and GULP [61] allow the internal core/shell motion to be rescaled by a thermostat after this initial equilibration period.

With the addition of pseudo particles, the definition of the instantaneous temperature $\mathcal{T}$ and pressure $\mathcal{P}$ during an MD simulation needs to be reconsidered. Usually, these are defined by [28]

$$\mathcal{T} = \frac{2}{3Nk_B}K = \frac{1}{3Nk_B}\sum_i^N m_i v_i^2 \tag{2.24}$$

and

$$\mathcal{P} = \frac{2}{3V}K + \frac{1}{3V}W = \frac{1}{3V}\sum_i^N m_i v_i^2 + \frac{1}{3V}\sum_i^N r_i f_i \tag{2.25}$$

where V corresponds to the system volume, k_B to the Boltzmann constant and N to the number of particles. m_i, r_i, f_i, and v_i are the mass, positions, force and velocity of particle i. K represents the kinetic energy and W the internal virial. In the massless core/shell model, the temperature and pressure are clearly given by the core motion since the shells are not explicitely included in the time integration scheme. This is not the case for the adiabatic core/shell model however. Here, the temperature may depend on the COM velocity of the core/shell pairs (when the imaginary degree of freedom is decoupled) or on all velocities including the relative core/shell motion. In both cases, the $3N$ DOF defining the temperature correspond to the physical system, i.e. three for each core/shell pair [53, 59]. The pressure can be defined in two ways, either by unifying the core/shell particles as centers or by counting each particle as a separate atom. Each variant requires a different approach to the kinetic contribution K and the virial W. In the unified approach the internal core/shell contributions are ignored. It follows, that the kinetic energy corresponds to the COM motion K_C of the core/shell pairs and a centralized force component corresponding to the atom-atom virial without the core/shell spring contribution are considered

$$\mathcal{P} = \frac{2}{3V} K_C + \frac{1}{3V} W_C \qquad \text{with} \qquad W_C = W - \sum_m r_{cs,m} \, f_{\text{spring},m} \tag{2.26}$$

with $r_{cs,m}$ as the core/shell separation of m core/shell pairs and $f_{\text{spring},m}$ the harmonic spring force of each core/shell pair (note that this spring force constitutes the internal core/shell forces and is equivalent to the particle-center contribution). In the approach based on separate atoms, the atom based kinetic contribution and the full atom-atom force contribution W needs to be taken into account (including the spring contribution) [62]. Both variants are identical in the limit of the adiabatic approximation [62] and might be equally convenient for an implementation depending on the original core/shell code.

The adiabatic core/shell model requires a smaller time step during an MD simulation due to the resolution of the fast core/shell motion. Nevertheless, this additional computational cost is smaller than for the massless model which suffers from the high cost of the numerically demanding shell relaxation.

In the context of this thesis, the formalism for the adiabatic core/shell model was implemented and released into the official distribution of the MD code LAMMPS [58].

3 Methods and Analysis

In this chapter, the computational approaches which are used to systematically investigate disordered energy materials are elaborated. Besides the theoretical background, emphasis is put on practical aspects which are the key methodological developments in this thesis. Specifically, methods are presented which are essential for the composition of computational models and for the evaluation of properties from statistical mechanics and thermodynamics.

3.1 Force Field Parameterization

Force field potentials are effective models based on parameterized analytical expressions to describe interactions between atoms. As mentioned in Sec. 2.2, the involved expressions are chosen on the basis of the target chemical system and can differ significantly. Therefore, they are defined within a flexible framework in which atoms are distinguished by "types" rather than elements. These carry particular properties like mass and charge, and a connectivity may be assigned for predefined interactions to describe directed bonds, angle dependencies, and the like. The corresponding mathematical terms are designed following chemical intuition which is based on characteristics of the described systems' composition, e.g. coordination environments, oxidation states or hybridization [27, 38]. Clearly, the accuracy of a force field depends on the suitability of the physics conveyed in the analytical expressions for the target compound. On top of this, their parameterization is equally decisive in order to yield correct energies and derived forces. While the analytical terms are chosen based on physical insight, their parameters need to be derived numerically for which different strategies have been developed over time [38, 52, 63, 64].

In general, force field potentials are categorized via the reference data they are parameterized to. Broadly, two classes, empirical and higher level theory derived potentials are distinguished. The former is based on a fitting procedure of the parameters to minimize the squared deviation from experimental observables. Target values like densities, lattice constants, vibrational spectra, heat capacities as well as elastic and dielectric properties are commonly used. While this reference data comprises rigorous and accurate material properties, sufficient availability is not always given. Additionally, the derived potentials yield a behavior to reproduce the (experimental) macroscopic equilibrium. Therefore, interactions might be microscopically inaccurate and in any case of effective nature. For that reason, they are unlikely transferable to other chemical systems [28, 38, 52]. In contrast to empirical potentials, higher level theory derived potentials are based on *ab initio* data. These can be computed for any model system with a (theoretically) arbitrary chemical spectrum allowing for a maximum in transferability. For a fitting procedure, *ab initio* data provides atomistic properties as target values. Due to the microscopic nature of the force field interactions, these give a more direct and detailed comparability than effective ensemble averages taken from empirical data. An obvious choice for atomistic target properties are energies and forces — the very same properties the analytic terms in a force field yield [38, 52, 64]. A parameterization strategy based on such a direct match is coined "Force Matching" which is the method employed in this thesis.

3.1.1 Force Matching

Force matching is a state-of-the-art parameterization strategy which aims to fit the underlying interactions of a force field potential directly to their *ab initio* counter parts at 0 K. A potential is thus derived in a bottom-up approach giving accurate microscopic interactions which should yield correct macroscopic properties. The derived parameters are thereby purely empirical to reproduce the physical reference data [64].

Naturally, the quality of the obtained parameters depends strongly on the used reference data. The latter is contained in a so-called training set and consists of model structures representing the chemical system which the aspired potential shall describe. The selected structures should thus include all local environments, especially those far away from equilibrium, in order to provide a good description of the configurational variation. For this, a valid strategy is to amend the training set iteratively with structures which intermediate (unsuccessful) potentials explore (for example in an MD simulation) [64, 65]. It should be noted that the composition space of the training set determines the validity of a derived potential and therefore its transferability.

In the parameterization procedure energies, forces and stresses are target properties. The latter need to be included as a constraint within the usually vast solution space given by energies and forces. Otherwise, an accurate description of bulk properties is hardly obtained. Hereby, the full stress tensor $\sigma_{\alpha\beta}$ is taken into account as defined by the virial theorem

$$\sigma_{\alpha\beta} = -\frac{\sum_i^N r_{i\alpha} f_{i\beta}}{3V} \tag{3.1}$$

where V is the cell volume, N the number of atoms, $r_{i\alpha}$ the position and $f_{i\alpha}$ the force component of particle i in the Cartesian direction α or β, respectively. In direct comparison to the reference data in the training set, parameters are optimized by local or global fitting routines which minimize a cost function Γ [64, 65]

$$\Gamma(p_i) = w_e \Delta E + w_f \Delta F + w_s \Delta\sigma \tag{3.2}$$

where p_i is the parameter set describing all interactions in the force field, ΔE, ΔF and $\Delta\sigma$ are the deviations in energy, forces and stresses and w_e, w_f, w_s are weights assigned to the contributions. The formulation for the energy term ΔE is based on the squared deviation of the energies E

$$\Delta E = \frac{\sqrt{\sum_k^{n_c-1} \sum_{l>k}^{n_c} ((E_k^{\mathrm{cl}}(p_i) - E_l^{\mathrm{cl}}(p_i)) - (E_k^{\mathrm{ai}} - E_l^{\mathrm{ai}}))^2}}{\sqrt{\sum_k^{n_c-1} \sum_{l>k}^{n_c} (E_k^{\mathrm{ai}} - E_l^{\mathrm{ai}})^2}} \tag{3.3}$$

where E_k^{cl} and E_k^{ai} are the energy for structure k of the potential with the parameter set p_i and of the *ab initio* reference, respectively. The double sum $\sum_k^{n_c-1} \sum_{l>k}^{n_c}$ ensures to include all energy differences between valid pairs of the n_c reference structures in the training set. A normalization by the squared sum of the *ab initio* energies is also applied. It should be noted, that the energies only of structures with the same stoichiometry are compared. This way, the parameterization to total *ab initio* energies is avoided and only relative energies are considered. The force term ΔF for the squared deviation of the forces F is given as

$$\Delta F = \frac{\sqrt{\sum_{k=1}^{n_c} \sum_{l=1}^{N} \sum_\alpha |F_{k,l,\alpha}^{\mathrm{cl}}(p_i) - F_{k,l,\alpha}^{\mathrm{ai}}|^2}}{\sqrt{\sum_{k=1}^{n_c} \sum_{l=1}^{N} \sum_\alpha (F_{k,l,\alpha}^{\mathrm{ai}})^2}} \tag{3.4}$$

where the index k iterates over n_c reference structures, within which for every atom l the $\alpha = x, y, z$ spatial force components $F^{\mathrm{cl}}_{k,l,\alpha}$ and $F^{\mathrm{ai}}_{k,l,\alpha}$ of the potential with parameter set p_i are matched to those from the reference calculations. A normalization via the squared sum of the *ab initio* force components is applied. The stress term $\Delta\sigma$ is given as

$$\Delta\sigma = \frac{\sqrt{\sum_{k=1}^{n_c} \sum_{\alpha,\beta} |\sigma^{\mathrm{cl}}_{k,\alpha\beta}(p_i) - \sigma^{\mathrm{ai}}_{k,\alpha\beta}|^2}}{\sqrt{\sum_{k=1}^{n_c} \sum_{\alpha,\beta} (\sigma^{\mathrm{ai}}_{k,\alpha\beta})^2}} \tag{3.5}$$

where diagonal $\alpha\alpha$ and off-diagonal $\alpha\beta$ stress components for each reference k are compared. Also here, a normalization via the *ab initio* stresses is applied. Alternatively, the latter can be replaced with an expression including the bulk modulus B $(= 3B\sqrt{n_c})$. It is recommended that the weights should be set with $w_e \leq w_f, w_s$ to account for the abundancy of data points of each property per reference structure [65].

3.1.2 *Fitting the force field parameters*

The cost function Γ defines the fitness of a trial parameter set p_i with respect to the training data. The latter consists of *ab initio* properties in the here used “Force Matching” methodology (see above Sec. 3.1.1), but could equally be based on empirical macroscopic properties. Maximizing the fitness obtained from minimizing the cost Γ by varying the parameters in p_i thus leads to an improved force field potential. In that, the search for a force field presents itself as a global optimization problem, where the individual parameters span a multidimensional cost surface. The latter is high-dimensional since usually many parameters are included in the formulation of a force field. Additionally, complicated interdependencies of the parameters arise in the analytical expressions which yield a corrugated fitness-parameter space. Thus, their optimization does not present a trivial task. A thorough search is hence necessary which can be computationally intensive. Therefore, both the evaluation of the fitness for a trial parameter set as well as the global search strategy needs to be efficient. In that, the former determines the performance of a single evaluation step and the latter how many steps need to be taken to obtain a satisfactory result.

In the evaluation of the fitness function, many single point calculations over the training set structures need to be performed in order to retrieve their respective energies, forces, and stresses. This requires the largest share of computer time during an optimization procedure, for which efficient routines need to be implemented. In that, the minimization of input and output operations, meaning the reading and writing of files to the hard disk, presents a considerable acceleration. Additionally, parallel operations should be included in order to exploit computational resources ideally and reduce waiting time. In this thesis, this is realized by designing a framework based on PYTHON packages and the software LAMMPS [58]. Hereby, the software package ASE [66] is used for handling of atomic structures, which is directly linked to LAMMPS using PYTHON bindings. This way, a quick data transfer from the actual force field calculations to other optimization routines is facilitated. Furthermore, the PYTHON package MULTIPROCESSING is used to setup a task pool parallelization scheme. With this, the evaluation of the training set is split into a number of tasks which are distributed over the available processors.

In comparison to the improvement of the fitness evaluation, the global optimization strategy provides stronger leverage for an efficient procedure. However, it also presents a more difficult problem. This is based on the typically high dimensionality of the parameter space which is likely subject to many superbasins and local minima. Here, an exact solution which would require a most thorough sampling cannot be determined. Therefore, heuristic methods need to be employed. In literature, many different approaches are proposed for application, where the most consistent are either a mixture of simulated annealing and local optimizations, or the differential evolution algorithm (DEA), a variant of the genetic algorithm (GA) [64, 67, 68]. In this thesis, evolutionary motivated algorithms are used as implemented in the PYTHON package INSPYRED [69]. Besides the DEA, another evolutionary algorithm, the particle swarm optimization (PSO) [70] is employed. It is found that the latter provides a more efficient and successful global optimization procedure for treating this particular parameter space. Nevertheless, both methods provide viable solutions whereby neither finds a good local minimum but rather locates a related basin. Thus, after the global optimization procedure a subsequent local optimization is performed. In this regard, the most practical optimizer is found in the L-BFGS method as taken from the FITPACK library, conveniently interfaced through SCIPY [71].

Differential evolution algorithm

Motivated by the concept of natural selection, the DEA [67] treats a number of trial solutions in parallel and evolves them using “genetic operations”. In that sense, the solutions are called chromosomes which are held by individuals forming a population. The latter is altered via the operations mutation, crossover and selection over a course of generations. A population is thus expressed as an array holding each individual i with its chromosome, the trial parameter set p_i at generation g as $P_g = [p_{i,g}]$. The starting parameter sets are randomly initialized within valid bounds, e.g. normally distributed around an initial guess or uniformly distributed in the complete parameter space. Each generation, the individuals are evolved using the following genetic operations:

1. Differential mutation: For each individual i, a newly mutated parameter set $v_{i,g}$ is created via a linear combination of three randomly chosen individuals r_1, r_2 and r_3 from the current generation g according to

   $$v_{i,g} = p_{r_1,g} + F(p_{r_2,g} - p_{r_3,g}) \tag{3.6}$$

   where F corresponds to a random number $\in [0, 2]$ to control the amplification of the mutation.

2. Crossover: To diversify the linear combinations of mutation vectors, an analog to “mating” is introduced. The individual components x of the mutant parameter set of individual i are exchanged with the components x of the current parameter set of individual i. From this, a new (“mutated” and “mated”) trial parameter set $u_{i,g}$ is created following

   $$u_{i,g} = u_{i,g,x} = \begin{cases} v_{i,g,x} & \text{if} \quad n_r[0,1) < C_r \\ p_{i,g,x} & \text{if} \quad n_r[0,1) \geq C_r \end{cases} \tag{3.7}$$

   where n_r is a random number $\in [0, 1)$ drawn for every component and C_r is a fixed cross over constant. Following this, the resulting trial parameter set consists of mutations from linear combinations where single components are left unchanged.

3. Selection: The trial parameter sets $u_{i,g}$ are evaluated using the cost function Γ and exchanged for the current set for an individual i following

$$p_{i,g+1} = \begin{cases} u_{i,g} & \text{if} \quad \Gamma(u_{i,g}) \leq \Gamma(p_{i,g}) \\ p_{i,g} & \text{if} \quad \Gamma(u_{i,g}) \geq \Gamma(p_{i,g}) \end{cases} \tag{3.8}$$

The algorithm is terminated if an individual reaches a fitness below a specified threshold (if known) or the rate of improvement is exhausted.

An implementation of the DEA is comparably simple and its execution is not time critical. In that, it does not hold a large working memory, since at any time, only three arrays with the size of the population × number of parameters need to be stored. Namely, the current population P_g, the mutated population v_g and the trial population u_g.

In characterizing the algorithm, this variant of the GA finds a best parameter set confined within the initial set of parameters. Thus, the diversity of the initial population decides over the sampling width within the parameter space. In comparison, the general GA has a different mutation and selection mechanism [72] which allows it to explore a broader search space. Here, the convergence is, however, considerably slower and does not prove viable for the corrugated parameter space encountered in a force field parameterization [73].

Particle swarm optimization

The particle swarm optimization (PSO) algorithm [70] is also inspired by search patterns observed in nature, specifically those of fish or bird swarms searching for food. Here, the terminology encompasses particles in a swarm which move through the search space with time. In that, each particle possesses a position which corresponds to a trial parameter set p_i with coordinates corresponding to its individual components. The particles then move with a velocity defined by the search algorithm. At a time $t = 0$ particles are initialized as in the case of the DEA, normally distributed around an initial guess or uniformly distributed within the parameter bounds. They hold an initial individual velocity which is defined from their positions as

$$v_i(0) = \frac{p_i(0) - p_{\text{min}}}{\Delta t} \tag{3.9}$$

where p_{min} is the lower bound of each parameter in the parameter set and Δt is a specified step width. Each time step the particle position is updated to a new position $p_i(t+1)$ as

$$p_i(t+1) = p_i(t) + v_i(t+1) \cdot \Delta t \tag{3.10}$$

whereby the particle velocity $v_i(t+1)$ is composed of information including an individual and collective memory. Here, a personal best position p_i^b and collective best position p_g^b are stored at any time. Both, quantities influence the particle velocity, following

$$v_i(t+1) = c_0 v_i(t) + c_1 n_r^1 \frac{p_i^b - p_i(t)}{\Delta t} + c_2 n_r^2 \frac{p_g^b - p_i(t)}{\Delta t} \tag{3.11}$$

where n_r^1 and n_r^2 are uniform random numbers $\in [0, 1]$ and $p_i^b - p_i(t)$ and $p_g^b - p_i(t)$ are the distances of a particle at its current position $p_i(t)$ to its personal best and collective best, as illustrated in Fig. 3.1. The included random numbers allow for a randomized exploration of the parameter space. The constants c_0, c_1 ,and c_2 are weights which are specified to decide the influence of each contribution to the velocity. According to their origin, these are termed inertia, self-memory (or cognitive rate) and collective-memory (or social rate) constants. For these, recommended values in typical applications are (1,2,2) or (0.5,1.5,1.5) [72].

Similarly to the DEA, a simple and lean implementation of the PSO is possible. Virtually no computer time goes into its evaluation and only the current swarm $p(t)$ and the best positions p^b, need to be stored at any time.

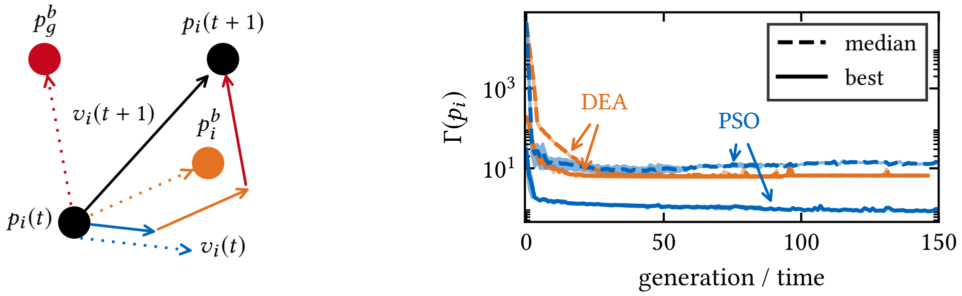

Fig. 3.1: (left) Schematic of the particle velocity in the PSO. The contributions of the inertia $v_i(t)$ (blue), the self-memory p_i^b (orange) and the collective memory p_g^b (red), are graphically depicted. These, are combined as described in Equ. 3.11 to yield the velocity $v_i(t+1)$ (black) for the propagation of the individual particles (black). (right) Comparison of the performance of the DEA (orange) against the PSO (blue) for a force field potential parameterization of Li_3OCl (see Sec. 5.3). For each algorithm the average of three optimizations is shown using 1000 particles/individuals where each is randomly initialized following a uniform distribution within the parameter bounds. The filled-in region shows the variance of the three runs for the best and median cost, respectively.

In evaluating the PSO for a force field parameterization, it is found that its performance is superior to the often applied DEA. This is shown in Fig. 3.1 where the PSO finds better minima on average. Here, the overall swarm maintains an explorative behavior which can be seen in the high lying cost-median. Single best particles only draw the swarm slowly to the current minima. In contrast, the DEA converges the individuals much faster to a minimum (seen in the early coincidence of cost-median and -minium). This behavior is prone to an early arrest of the exploration, rendering this algorithm less suitable for the corrugated high-dimensional optimization problem.

3.1.3 Parameterization of Polarizability in the Core/Shell model

A special case for a parameterization problem are augmenting models which add a new functionality to a basic force field. One of those lies in the inclusion of the electronic polarizability important for an accurate description of many ionic and polar systems. For this, the core/shell model is used in this thesis due to its accuracy and simplicity as described in detail in Sec. 2.2.2. Here, a satellite particle (the shell) carrying an extra charge q_s is attached to the original ion (the core). Restored via an harmonic force, the shell mimics the polarization of an electron hull by reacting to the electrostatic environment. Two parameters are therefore included in the core/shell model, namely the spring constant k and the shell charge q_s which directly combine to the polarizability $\alpha = q_s^2/k$. Since the latter presents the only effective parameter, either k or q_s are required to be parameterized. Usually, an intuitively chosen q_s is kept fixed and k is optimized following different strategies.

One frequently used strategy is based on fitting k simultaneously with the remaining parameters of the force field to the elastic constants (C_{11}, C_{12}, C_{44}), phonon frequencies (e.g. from infrared spectroscopy) and the high frequency and static dielectric constants (ϵ_∞ and ϵ_0). In this rigorous approach the combination of these physical properties is chosen to yield a reliable model [52, 63, 74]. As mentioned before, it is difficult to control a fit to coerce each parameterized term to cover exactly the purpose of its physical origin when referencing to empirical ensemble averages. Considering the added flexibility introduced by the core/shell terms, this effect becomes very likely. Thus, a phenomenological model results, yielding correct macroscopic properties which derive from incorrect microscopic relations [52]. For example oxygen polarizabilities of 0.1156 Å^3 which strongly deviate from *ab initio* and experimental references of 1.58-2.07 Å^3 [75] in a tetrahedral Li coordination environment have resulted in the parametrization of Li_2O and Li_3OCl [76]. Here, the core/shell interactions compensate an inaccurate underlying force field rather than providing a correct polarizability. Knowing that this flaw is strongly enhanced by the reference data, a simultaneous fit of all parameters against *ab initio* reference properties is alternatively performed [63]. This likely yields a more physical interaction model due to the better comparability to the reference data. However, even here resulting core/shell parameters have sometimes shown to be void of any physical meaning.

Considering the underlying purpose of the core/shell model, a physically motivated parameterization is feasible. Thereby, an isolated fit of only the core/shell parameters to an according reference is possible. In comparison to the macroscopic dielectric constants, defect [52] and reorganization energies [68] from *ab initio* data present a better reference with a higher microscopic accuracy. It should be noted, that these are dependent on the static dielectric constant ϵ_0 only. Since force field potentials are mainly employed in simulations where the importance in accuracy of structure outweighs that of optical properties, this reference appears more advantageous than the high frequency dielectric constant ϵ_∞. In practice, the microscopically motivated parameterization strategy should be combined with a force field potential which is previously parameterized in a 0 K picture to *ab initio* data of only non-defective structures. Subsequently, the core/shell parametrization can be followed based on defective structures. This yields a consistent potential, allowing for some control in the physicality of the individual force field terms. In that, it prevents non-core/shell parameters to produce an overly averaging description (of the defective and non-defective system) which has been reported to give a high penalty in accuracy [52]. Besides its above mentioned advantages, the physically motivated strategy additionally allows to reduce the computational cost of the fitting procedure. This is due to the fact, that the core/shell parameterization can be executed separately. In the latter each reference calculation to evaluate the core/shell parameters includes the relaxation of all shell positions. An increase of the computational cost by 1-2 orders of magnitude of each evaluation step can thereby be expected. If parameterizing core/shell parameters in combination with others, this increase affects every evaluation of the fitting procedure, then within the usual rigorous global search. Thus, a separate, physically motivated parameterization renders as considerably more feasible and is thus the employed procedure in this thesis (see Sec. 5.3).

3.2 Monte-Carlo sampling approaches for thermodynamic ensembles

In atomistic simulations, the model structures of materials are often taken from experimental input. This works especially well when treating high symmetry crystals where the atomic positions can be determined by experimental techniques with a high accuracy. Unfortunately, this is not the case in most complex materials where uncertainty about the atomic structure prevails. Many battery materials belong to this category, due to their inherent disorder. Since their simulation is subject of this thesis, a strategy for the determination of relevant atomistic structural models is required. A powerful approach is based on Monte-Carlo simulations which can be used to explore structural ensembles.

For this, a perspective following statistical thermodynamics is taken: Each microscopic configuration of a material, that is the structure defined by the individual atomic positions, can be interpreted as a microstate of a thermodynamic ensemble. To estimate whether such a microstate is relevant, its probability p to occur in the equilibrium ensemble (defined by temperature and pressure) needs to be determined [77, 78]

$$p(r^N) = \frac{\exp\left(-\frac{E(r^N)}{k_B T}\right)}{Z} \qquad \text{with} \qquad Z = \int \exp\left(-\frac{E(r^N)}{k_B T}\right) dr^N \tag{3.12}$$

where r^N are the positions of the N particles belonging to the configuration of a microstate with a potential energy $E(r^N)$, k_B is the Boltzmann constant and T the temperature. The potential energy-based partition function Z represents the integral over all possible microstates of the material. Considering the $3N$ degrees of freedom for the atoms in the system, Z is composed of an unseizable amount of configurations which cannot be explicitly computed. This holds in most materials even when discretizing the space of relevant structures (e.g. to local minima, see Sec. 4.4) [77, 78]. The overall problem in determining the probabilities $p(r^N)$ for trial structures lies within the partition function Z which is in practice inaccessible. However, good estimates can be obtained using Monte-Carlo importance sampling as described in the following.

3.2.1 Metropolis Monte-Carlo and Beyond

The Metropolis importance sampling

In importance sampling the ratio defined by Equ. 3.12 is estimated by a Monte-Carlo scheme. In the latter, a simulation is propagated between structures S_n based on the evaluation of a random number $n_r \in [0, 1]$ against a transition probability p_A. Starting from a random initial structure, at each step n a random trial structure S_{trial} is proposed and based on the outcome of n_r and p_A accepted or rejected as

$$S_{n+1} = \begin{cases} S_n & \text{if } n_r > p_A \\ S_{\text{trial}} & \text{if } n_r < p_A \end{cases} \tag{3.13}$$

where S_n is the structure at the current step n and S_{n+1} is the structure in the next step. Since p_A only depends on the previous state, a Markov chain of sampled states is created. For the importance sampling the most prominent method is based on the Metropolis acceptance criterion [79]. The associated transition probability p_A derives from the microstate probability $p(r^N)$ between the current and the trial structure (see Equ. 3.12) as

$$p_A = \min\left(1, \frac{p(r^N_{S_\text{trial}})}{p(r^N_{S_n})}\right) = \min\left(1, \exp\left(-\beta\left(E_{trial} - E_n\right)\right)\right) \tag{3.14}$$

where E_trial and E_n correspond to the potential energy $E(r^N)$ of the trial structure and the originating step respectively and $\beta = 1/k_BT$ is the reciprocal product of the Boltzmann constant k_B and the temperature T. The minimum function min tops the acceptance probability at 1 which is a guaranteed acceptance if $E_{n+1} < E_n$. It should be noted, that this criterion complies with detailed balance. Here, the transition probability p_A guarantees that the number of accepted trial moves to a state a is exactly equal to the number of accepted trial moves from state a. This way the estimated ratio in Equ. 3.12 stays consistent in the long time limit [29, 77].

Accelerated sampling

The Metropolis criterion as presented above creates a canonical ensemble for a temperature T in the long time limit. Here, the necessary amount of sampling (the simulation time) depends on the ease of exploring the configuration space of the underlying system. Corrugated potential energy landscapes therefore require longer sampling due to the fact that the probability to cross high energy barriers based on the condition in Equ. 3.14 is small. Several ways exist to accelerate the sampling, where early approaches focused on improving the selection of new trial structures based on schemes which preserve the condition of detailed balance [29, 77]. Besides these problem dependent approaches, more general methods have been proposed, the most notable of which is parallel tempering [80, 81].

In parallel tempering (also known as replica exchange) several Metropolis Monte-Carlo sampling runs are conducted in parallel. Each replica samples in a canonical ensemble at different temperatures which increase starting from the temperature of interest. High temperatures allow for the sampling of larger fractions of the configuration space while low temperatures probe the local energy landscape more thoroughly. To spread the degree of sampling evenly over the configuration space, replicas exchange their temperatures (or configurations, respectively) based on an additional Monte-Carlo step. The probability p_exchange for the exchange of temperatures T_i (contained in β_i) and T_j (contained in β_j) of two replicas i and j is expressed as

$$p_\text{exchange} = \frac{\exp\left(-\beta_j E_{n,i} - \beta_i E_{n,j}\right)}{\exp\left(-\beta_j E_{n,j} - \beta_i E_{n,i}\right)} = \exp\left[\left(\beta_j - \beta_i\right)\left(E_{n,i} - E_{n,j}\right)\right] \tag{3.15}$$

where $E_{n,i}$ and $E_{n,j}$ are the potential energies of each replica at step n. As represented by the first expression in Equ. 3.15 this Monte-Carlo step also maintains detailed balance (including the forward and backward swap acceptance probability). The trial moves can be attempted after every step or after a constant number of steps. An implemented trial frequency should target an overall temperature swap at an acceptance ratio of 20 %, which ensures an efficient sampling [80]. Decisive for this ratio are also the temperatures of the ensembles. Attempted swaps are usually conducted between replicas with adjacent temperatures to be successful. Therefore, a geometric progression of the involved temperatures (T_i/T_{i+1} = constant) has been frequently suggested. The parallel tempering formalism creates canonical distributions for all temperatures involved and ensures a fast and efficient sampling. It should be mentioned that besides temperature, also other physical and non-physical parameters can be swapped between the replicas [29, 80].

3.2.2 Wang-Landau Sampling

The above described methods sample configurations for a canonical ensemble which is bound at a temperature (or several temperatures). In contrast to that, the Wang-Landau sampling directly estimates the partition function Z (see Equ. 3.12) [82–88]. In that, it produces an estimate of the configurational density of states (cDOS) (denoted as $g(E)$) which gives the number of all possible configurations for an energy E. This relates to the partition function Z as

$$Z = \int g(E) \exp\left(-\frac{E}{k_B T}\right) dE \equiv \sum_i g(E_i) \exp\left(-\frac{E_i}{k_B T}\right) \tag{3.16}$$

Similar to the estimated ratio over Z in the Metropolis importance sampling (see above Sec. 3.2.1), the Wang-Landau sampling gives a relative cDOS $g(E)$ which yields a comparative weight of the amount of configurations at a certain energy. In simulations, these energies are usually discrete or in the case of continuous variables represent an energy bin E_i (see right term in Equ. 3.16). With the goal to estimate a representative structural/configurational ensemble of a material at a temperature T, the according probability for a structure with an energy E_i can be retrieved in the canonical distribution $P(E,T)$. The latter relates to $g(E)$ as

$$P(E_i, T) = g(E_i) \exp\left(-\frac{E_i}{k_B T}\right) \tag{3.17}$$

It should be noted that the cDOS can also be defined as a function of other physical quantities, for example of the magnetization as often done in Ising models.

The Wang-Landau sampling is conducted as a random walk in energy space. It is thereby based on a transition probability between energy levels E_i which depends on a continuously updated $g(E_i)$ as

$$p(E_n \rightarrow E_{\text{trial}}) = \min\left[1, \frac{g(E_n)}{g(E_{\text{trial}})}\right] \tag{3.18}$$

where E_n is the energy of the originating and E_{trial} the energy of the target configuration. After an accepted step the new energy level becomes the origin and its bin is updated, while a rejected step ends with an update of the originating bin. Bins are updated by multiplication with a modification factor f resulting in $g(E_i)' = f g(E_i)$. Initially, each bin is given a value of 1 and f is set to e. To ensure an even sampling of the chosen energy range, a histogram $H(E)$ with the dimension of $g(E)$ accumulates each visit and is periodically checked for its flatness (usually 1000 MC times, MC time = trial MC steps / bins in $g(E_i)$). Based on the relative deviation of each entry $H(E_i)$ from the mean $\langle H(E) \rangle$ the flatness h_f is reached when $\|H(E_i) - \langle H(E) \rangle\| \leq (1 - h_f) \langle H(E) \rangle$. Once a required flatness is arrived at (usually $h_f = 80\,\%$ [82, 84, 85]), the modification factor f is refined as $f' = \sqrt{f}$. This way the sampling is propagated until f converges to a target value while becoming progressively more accurate [82, 84].

Since the sampling depends on a predefined, discretized energy range which determines the bins in $g(E)$, the treated problem must be previously explored [86]. Alternatively, there are proposed schemes which adapt this energy range on the fly [89]. In some cases, a sampling may be conducted within restricted bounds located on the known energy range (for example when trivially parallelizing — see below). Here, sampling at a boundary is inevitable. To capture such boundary effects, steps outside the assigned range need to be counted into the originating bin [83].

Obtaining the cDOS for complex systems

The Wang-Landau sampling provides in principle a good assessment of the whole configurational space since not energies but the cDOS defines the acceptance probability. Here, $g(E)$ acts as a bias which in combination with the flatness criterion forces the system into non-explored energy regions ensuring an overall broad sampling. Unfortunately, the convergence of $g(E)$ may be very slow. Despite accelerating schemes like the so-called $1/t$ algorithm [85, 88] the Wang-Landau sampling remains a challenge for complex practical applications like the configuration space of disordered materials. A major reason for this is the enforced flatness. It requires Monte-Carlo steps to drive the system very evenly across the full energy range in every refining cycle of the cDOS (during which f remains constant). For this reason, parallelized sampling has been suggested with random walkers sampling simultaneously in a replica-exchange type strategy [87]. While this facilitates a faster sampling across the energy range, it requires a large pool of computational resources for a single calculation. An alternative is trivial parallelization as employed in this thesis. Here, several walkers sample independently on overlapping energy ranges [82, 84, 87]. While this solution is less elegant, it allows for a flexible distribution of computational resources.

In the trivial parallelization each walker i performs an individual Wang-Landau sampling. The resulting $g(E)_i$ are joined in a post-processing step within their overlap regions. A best coinciding point is thereby based on the gradient of the logarithm of $g(E)_i$, which corresponds to the inverse microcanonical temperature ($1/T = d(S(E))/dE = d(\ln(g(E)))/dE$). In literature [87], $d(\ln(g(E)))/dE$ is approximated via finite differences. This leads to errors propagating along the energy axis E which amplify with the roughness of $g(E)_i$ (see Fig. 3.2). A tolerable error is only obtained if the sampling is propagated until convergence to a smooth $g(E)_i$. An alternative to this finite difference method, developed in this thesis, conjoins the sampled $g(E)_i$ based on a noisy data approach. For this, B-spline functions are used to obtain a smoother gradient [1] (see Fig. 3.2):

1. Each $\ln(g(E)_i)$ is fitted via a spline function, where data points are weighted by their reciprocal distance to a linear fit of $\ln(g(E)_i)$. Thus, outliers weigh less which allows for a minimal smoothing parameter. Robust scaling factors $\Delta \ln(g(E))$ between adjoined $\ln(g(E)_i)$ are then obtained from a best coinciding gradient ($d(\ln(g(E)))/dE$).

2. The raw data sets $\ln(g(E)_i)$ of each walker are scaled via $\Delta \ln(g(E))$ and a smooth global function is fitted by another spline.

As seen in Figure 3.2, this procedure leads to a robust approximation of $g(E)$. In comparison to that, the finite difference method yields a conjoined $g(E)$ with a strong non-continuity even at late convergence cycles, which originates in an inaccurate assembly. Thus, the application of the noisy data approach renders superior. In that, it is even possible to sample at a lowered flatness as well as to apply an early termination criterion. This is due to the fact, that the smoothness of the raw data is not that critical anymore as further elaborated in Sec. 4.4.

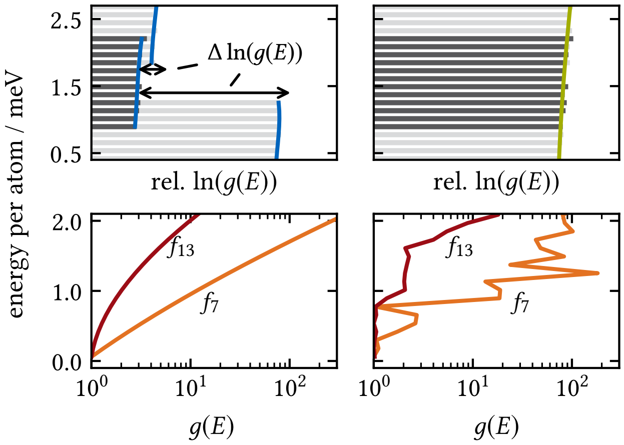

Fig. 3.2: (top left) Relative $\ln(g(E)_i)$ of neighboring random walkers i (in shades of gray). The individually fitted spline functions are shown in blue and the resulting scaling factors $\Delta\ln(g(E))$ which relate the relative $\ln(g(E)_i)$ are indicated. (top right) Scaled $\ln(g(E)_i)$ of the same individual walkers with the globally fitted spline function (green). (bottom left) $g(E)$ for early and late refining cycles f_7 and f_{13} resulting from the spline function based procedure in comparison to the finite difference approach (bottom right). The data is based on the configuration space sampling of $Li_4Ti_5O_{12}$ (see Sec. 4.4) using the typical inspection interval and flatness of 1000 MC time and 80 %

3.3 Material properties from simulations

3.3.1 Ion transport

Ion transport is a central property in battery materials. From computer simulations it can be determined with comparably high accuracy for an investigated model. On the one hand, using statistical mechanics gives access to average ensemble properties which exhibit apparent macroscopic coefficients. On the other hand, the examination of detailed atomistic processes allows for effective estimates and the determination of a transport mechanism.

Transport coefficients from microscopic quantities

To evaluate transport coefficients from equilibrium MD simulations, two approaches are commonly used. The first is the Green-Kubo (GK) formalism which is based on linear response theory or more precisely the fluctuation-dissipation theorem. Here, the response of a dynamic variable A near its equilibrium $\langle A\rangle_0$ to a weak, time dependent perturbation $\langle\Delta A(t)\rangle$ is considered. The latter can thereby be assumed in a linear regime due to its small magnitude. For the transport at equilibrium, i.e. when no external driving force is present, a perturbation in a mechanical property is decisive. This can be derived to yield a time correlation function relating the time derivative of the perturbation variable $\dot{A}(t)$ to its macroscopic transport coefficient λ [28, 29]

$$\lambda = \int_0^\infty \langle\dot{A}(t)\dot{A}(0)\rangle dt \tag{3.19}$$

A second approach is based on the closely related Einstein formalism. Originally derived for Brownian motion, it yields an analogous expression which holds at long sampling times Δt [16, 28, 29] and is given as

$$2\Delta t\lambda = \langle \left(A(t) - A(0)\right)^2 \rangle \tag{3.20}$$

The GK and Einstein formalism are strictly equivalent. Both are used in the evaluation of transport coefficients whereby different advantages and disadvantages in their application are found as outlined in the following.

Macroscopic diffusion coefficients

Based on the above mentioned relations for transport coefficients, the macroscopic diffusion coefficients can be obtained from MD simulations. The central observable in this case is the position operator $\vec{r}(t)$ and its derivative in time, the velocity $\vec{v}(t)$. For the GK formalism follows the integral of the velocity autocorrelation function (VACF) to determine the diffusion coefficient D^* [28, 29]

$$D^* = \frac{1}{3}\int_0^\infty \langle \vec{v}_i(t)\vec{v}_i(0)\rangle dt \tag{3.21}$$

where $\vec{v}_i$ corresponds to the velocity of every particle i and the factor $\frac{1}{3}$ normalizes by the dimensions, i.e. the three spacial coordinates. The corresponding Einstein formulation, valid in the long time limit, contains the central property $\langle|\vec{r}_i(t) - \vec{r}_i(0)|^2\rangle$ called the mean square displacement (MSD) as originating from the position operator. It is given as [16, 28, 29]

$$D^* = \frac{1}{3}\frac{\langle|\vec{r}_i(t) - \vec{r}_i(0)|^2\rangle}{2\Delta t} \tag{3.22}$$

where $\vec{r}_i$ is the position of particle i, Δt is the sampling time and the formula is again normalized by the dimensions. To reduce statistical errors, the VACF and MSD can be time averaged. In that, a sampling over a lag time may be repeatedly initialized at constant time intervals in an MD simulation [90]. Hereby, the sampling sections should overlap to a reasonable degree, in order to exploit the obtainable statistics from the MD data. The computed diffusion coefficients are so-called tracer diffusion coefficients (denoted D^*). This is based on their original derivation where no particle interactions are considered. Thus, they refer to the motion of a tracer particle in a (homogeneous) medium in a random walk fashion [16, 91].

The central quantities to each formalism, the VACF and MSD exhibit system dependent behavior. This is demonstrated for the transport of Li in different systems as shown in Fig. 3.3. Here, the VACF decreases in time and, independent of its profile, drops to zero at a point of complete decorrelation. Its integral, however, behaves differently. In the liquid (melt of Li_3OCl, Fig. 3.3 top) a smooth integral converges to a finite value and thus gives a finite diffusion coefficient following Eq. 3.21. The convergence of the integral within the short correlation time is owed to the mean continous motion of particles in the liquid. In contrast to this, the integral drops to zero for the corresponding high temperature crystal (Li_3OCl, Fig. 3.3, bottom). Here the motion depicted during the correlation time only corresponds to vibrations of Li ions within the potential of their lattice sites. This behavior can be recognized from the strong oscillations around zero in the VACF. Long range motion in this crystal, corresponds to rare hopping events between vacancies (vacancy mechanism). Despite the high temperatures where the crystal shows many hopping events, this motion still correlates on a very long timescale. Even when going to considerably larger correlation times, the required statistics to capture this correlation in the long range tail of the VACF are unfeasible — an effect also observed for other quantities [92].

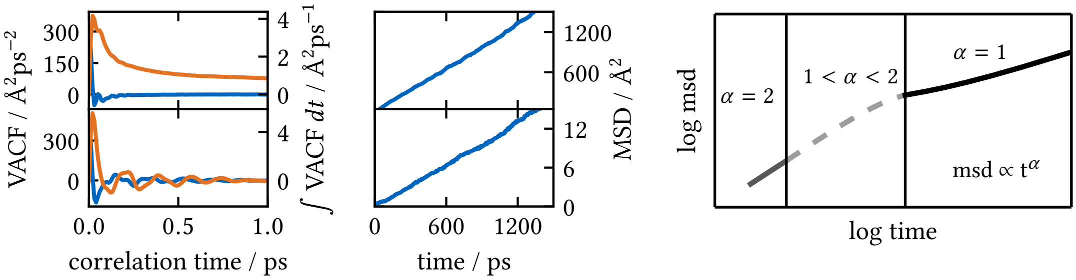

Fig. 3.3: Exemplary VACFs (blue) and their integral (orange, left) as well as the MSDs (blue, center) from the same simulation for Li in an ionic melt of Li_3OCl at 900 K (top) compared to the corresponding crystal with an included vacancy at 1200 K (bottom). (right) Schematic of motion regimes found in an MSD with the corresponding anomalous diffusion exponent α.

In contrast to that, the corresponding MSDs show a continuous increase for both systems. Thus, independent of the diffusion mechanism, a finite value of the MSD can be obtained and a macroscopic diffusion coefficient determined. It needs to be mentioned that long sampling times are necessary in order to reach statistically meaningful coefficients. In general, these depend strongly on the treated system. To determine the sampling time, the phenomenological diffusion regimes have to be distinguished. As shown in Fig. 3.3 on the right, these consist of a ballistic motion, an intermediate correlated motion and a long range transport. Each regime can be identified from the time dependency MSD $\propto t^{\alpha}$, where the anomalous diffusion coefficient α is decisive [93]. Only when $\alpha = 1$, one speaks of "normal diffusion" which in the long time limit is the only relevant transport regime. Thus, statistics need to be sufficient for the extraction of an accurate gradient MSD / Δt of the normal diffusion. While, the intermediate regimes are usually not recognizable in the MSD of a liquid or of solid at very high temperatures, in disordered media they show a strong influence (see for example 5.5). Here, the specific extraction of a gradient MSD / Δt only from the linear regime is crucial.

In conclusion, the MSD allows for a more transparent investigation of the macroscopic diffusion. This is true unless investigating a highly dynamical system where diffusion behavior can be derived from the short time scale. Thus, the Einstein formalism presents a more suitable approach in disordered materials and crystals with a vacancy-mediated diffusion mechanism.

Ionic conductivity

Closely related to the diffusion of ions is the ionic conductivity. Considering the influence of an external electric field on an ionic system, a current is induced yielding a non-equilibrium steady-state. When the external electric field slightly changes, an electric (vector) potential response from the ions of the system follows as a linear perturbation. This can be reformulated as an infinitesimal response of microscopic currents $\vec{j}^{\text{ion}}$ which are expressed as [29]

$$\vec{j}^{\text{ion}} = \sum_{i=1}^{N} q_i \vec{v}_i \tag{3.23}$$

where N is the number of particles i with charge q_i and velocity $\vec{v}_i$. Inserting this pertubation term into Equ. 3.19 for the GK formalism an expression for ionic conductivity σ_{DC} can be derived following the fluctuation dissipation theorem [29]

$$\begin{aligned}\sigma_{DC} =& \frac{1}{3Vk_BT}\int_0^\infty \langle \vec{j}^{\text{ion}}(t)\vec{j}^{\text{ion}}(0)\rangle dt \\ =& \frac{1}{3Vk_BT}\int_0^\infty \left\langle \sum_{i=1}^{N}\sum_{j=1}^{N} q_i q_j \vec{v}_i(t)\vec{v}_j(0)\right\rangle dt\end{aligned} \tag{3.24}$$

where k_B is the Boltzmann constant, T the temperature, and V the volume. This expression can be rearranged to recover the tracer diffusion coefficients D^*

$$\begin{aligned}\sigma_{DC} =& \frac{1}{3Vk_BT}\int_0^\infty \left\langle \sum_{i=1}^{N} q_i^2 \vec{v}_i(t)\vec{v}_i(0) + \sum_{i=1}^{N}\sum_{j\neq 1}^{N} q_i q_j \vec{v}_i(t)\vec{v}_j(0)\right\rangle dt \\ =& \frac{1}{3Vk_BT}\left(\sum_{\beta}^{n_\beta} q_\beta^2 N_\beta D_\beta^* + \int_0^\infty \left\langle \sum_{i=1}^{N}\sum_{j\neq 1}^{N} q_i q_j \vec{v}_i(t)\vec{v}_j(0)\right\rangle dt\right)\end{aligned} \tag{3.25}$$

where n_β is the number of different species β, N_β the number of particles belonging to that species and q_β its charge. From the rearranged expression in Eq. 3.25, it can be seen that the current correlation function includes the tracer diffusion of each species as well as a cross-correlation term. The latter thereby consists of the diffusion and charge interaction correlation [94, 95]. Neglecting the cross-correlation one can reformulate this expression to

$$\sigma_{DC} = \frac{1}{3Vk_BT}\sum_{\beta}^{n_\beta} q_\beta^2 D_\beta^* N_\beta . \tag{3.26}$$

This expression serves as an approximation for an idealized conductivity. The formulation 3.26 is often called the Nernst-Einstein relation and can be directly derived from the Einstein relation on basis of non-interacting particles [16]. An alternative approach based on the Einstein formalism of the current correlation was recently suggested by Haskins *et al.* [96]. Simply inserting the integral of $\vec{j}^{\text{ion}}$ into Equ. 3.20 as the analogous to the GK formulation yields

$$\sigma_{DC} = \frac{1}{6Vk_BT}\frac{1}{\Delta t}\left\langle \left\| \sum_{i}^{N} \left[q_i\vec{r}_i(t) - q_i\vec{r}_i(0)\right] \right\|^2 \right\rangle \tag{3.27}$$

where $\vec{r}_i$ is the position of particle i. This can be also written as

$$\sigma_{DC} = \frac{1}{6Vk_BT}\frac{1}{\Delta t}\left\langle \left\| \sum_{i}^{N} q_i\vec{d}_i(\Delta t) \right\|^2 \right\rangle \tag{3.28}$$

where $\vec{d}_i(t)$ indicates the displacement vector for each particle over the sampling time Δt. This way it may become apparent that Equ. 3.27 corresponds to the total charge transport, i.e. the cumulative distance which a "center of charge" moved. It should be noted, that this expression is not related to Eq. 3.26 but strictly follows the Einstein formulation for interacting particles.

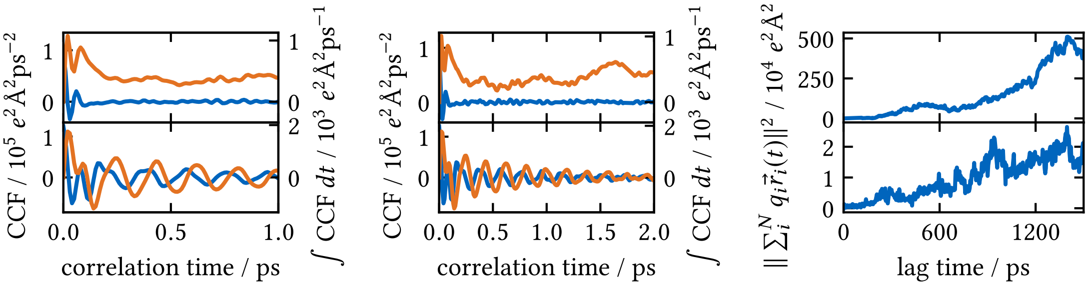

Fig. 3.4: Exemplary current correlation functions (CCF) in blue and their integral in orange as well as the total charge migration $\| \sum_i^N q_i \vec{r}_i(t) \|$ in blue for an ionic melt of Li_3OCl at 900 K (top) compared to the corresponding crystal with an included vacancy at 1200 K (bottom). Shown is the CCF with a maximum correlation time of 1 ps (left) and 2 ps (middle). The total charge migration following the Einstein formulation in Eq. 3.27 is shown on the right.

When obtaining the conductivity with either the GK or the Einstein formulation (as in Eq. 3.24 or 3.27), similar practical issues as described for the tracer diffusion coefficient arise (see above). As shown in Fig. 3.4 the GK formalism shows an oscillating behavior in a non-liquid and long range transport cannot be resolved within short correlation times. Slow convergence is observed due to the interaction correlation which even shows problematic behavior in the liquid. Although seemingly converged within 1 ps in the latter a recurrence of the correlation function becomes obvious going to longer correlation times. This badly converging behavior is well-known [94, 95] and results in large errors. Nevertheless, successful application with reasonable convergence of the GK formalism can be found in ionic melts at temperatures above 3000 K [97]. At such elevated temperatures a melt behaves like a true liquid with little ionic cross correlation, which is comparable to ionic motion in a solvent at dilute concentrations. In comparison to that, the equivalent Einstein formulation gives a more consistent conductivity. Due to the fact that long averaging times for the GK formalism are required in any case, the long time limit required for the Einstein formulation is not a disadvantage.

Atomic diffusion processes

It is not always convenient to perform equilibrium MD simulations to investigate transport. For example, a vacancy diffusion mechanism in a crystal will only exhibit sufficient motion events at unachievable simulation times or at high temperatures. Since a temperature dependence might change the actual diffusion mechanism, other approaches are required. Furthermore, macroscopic diffusion coefficients represent ensemble averages and do not elucidate on the diffusion mechanism which might reveal interesting insights relevant for the improvement of battery materials.

An alternative approach to investigate ion diffusion is by resolving single atomic diffusion processes, i.e. hopping events at 0 K [2, 9]. For these, the minimum energy paths are investigated reveiling an associated activation barrier ΔE_a. Tentative hopping events are thereby guessed and an accurate minimum energy path can be practically computed using the nudged-elastic-band (NEB) method or modified versions thereof [98, 99]. Based on the activation energies different possible migration pathways can be compared and thus the most likely diffusion mechanism identified. Neglecting entropy, an approximate hopping frequency Γ can be obtained from the activation barrier and a vibrational prefactor ν^*

$$\Gamma = \nu^* \exp\left(-\frac{\Delta E_a}{k_B T}\right). \tag{3.29}$$

Γ represents the probability for a hop to succeed which is attempted at the frequency ν^*. Here, the latter may be approximated via the lattice vibration or Debye frequency, respectively [2, 9, 16]. If the involved diffusion mechanism requires the presence of a vacancy, the hopping rate strongly depends on a defect formation energy $\Delta E_{\text{formation}}$. An approximate, effective hopping rate results as [16]

$$\Gamma' = \nu^* \exp\left(-\frac{\Delta E_a + \Delta E_{\text{formation}}}{k_B T}\right). \tag{3.30}$$

Since the vacancy formation probabilities are usually low, they affect the apparent diffusion considerably. Thus their determination is critical for the investigation of the diffusion and is discussed in more detail in the next section 3.3.2. Many studies follow the described approach to investigate a material. Some of these are conducted systematically in an attempt to derive material design principles for material classes [3, 7].

The above mentioned methodology relies on a good chemical intuition in order to guess all relevant elementary diffusion processes. Here, the dependencies on neighboring atoms - their chemical environment - needs to be taken into account. In that, success depends strongly on the complexity of the investigated system. In practice, working out all possibilities for a jump process by hand is only feasible for high-symmetry crystals. Although computer algorithms may aid in this task, the combinatorial problem quickly exceeds practical limits when investigating highly disordered materials. For that reason, an approach combining MD simulations and 0 K NEB calculations is used in this thesis (compare Sec. 4.5). Migration processes are sampled during a conventional equilibrium MD and then used as input processes for NEB calculations. This allows for a high degree of automatization and eliminates any dependency on chemical intuition.

Naturally, the sampling of processes is not a straight forward task in a model with continuous positions in space. Thus, a discretization of the atom positions in the MD simulation is necessary as visualized in Fig. 3.5. In the approach developed in this thesis, the continuous positions are projected onto a lattice, whereby for a crystal the according crystallographic symmetry lattice is used. The underlying host lattice, i.e. the fcc or hcp structure is adjusted to the mean thermal positions of the host ions in a first step and the interstitial sites placed on the resulting coordination centers. Atoms are then assigned to their closest crystallographic sites. In the case of a conflicting assignment, the closest ion is chosen for a site and the clashing ions are sorted to their next surrounding site. To capture atomic motion correctly for each snapshot in an MD trajectory, core sets around each crystal position are defined presenting a minimal radius for site association to filter recrossing events [100, 101]. Hereby, an acceptance radius corresponding to a fraction of the smallest distance between adjacent sites must be chosen. This choice needs to be carefully examined to compromise between a minimal recrossing ratio and loss of information. In comparison to other approaches found in literature [102, 103], the complete structure is mapped onto the lattice rather than only the mobile species. This gives the flexibility to extract the atomistic surrounding from different trial host structures in order to differentiate hopping processes via their chemical environment. The latter can be conveniently distinguished by e.g. comparing all atom-atom distances within a enclosing volume defined by the distance between the initial and final lattice site and a reasonable cutoff as shown in Fig. 3.5 [1].

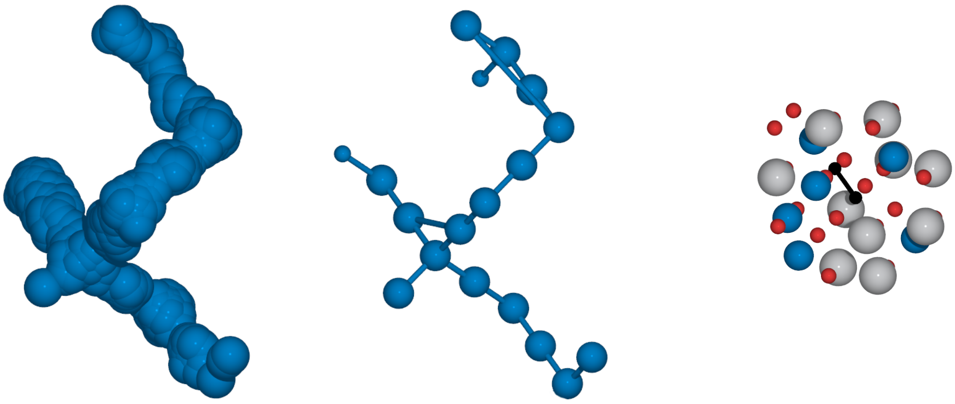

Fig. 3.5: Depiction of the discretization of the Li ion motion to the crystallographic sites in a trajectory for the example of $Li_4Ti_5O_{12}$ (compare Sec. 4.5). (Left) undiscretized trajectory depicted as a Li ion density plot where all continuous positions sampled during the trajectory are shown. (Middle) the corresponding discretized trajectory with all occurring hops marked by a connection. (Right) schematic of an enclosing cavity to isolate the chemical environment surrounding a hopping process (indicated in black). Li ions are depicted in blue, Ti ions in grey and O ions in red.

Although only effectively appearing processes are investigated in the according NEB calculations, a large number of distinguishable processes can still be found. Considering also the computational cost of MD simulations in general, this rigorous approach is only feasible when used with classic force field potentials or semi-empirical methods.

Correlation factors and Haven ratio

In characterizing the macroscopic diffusion or conductivity, useful quantities are the correlation factor f_{corr} or the Haven ratio H_R, respectively. These allow for mechanistic interpretation by relating the apparent ion transport to the uncorrelated and/or dilute case, respectively. In the case of a crystals, i.e. the diffusion on a lattice, the correlation factor relates the overall particle displacement $R = \sum_{i=1}^{n} \vec{r}_i$ within n steps of displacements $\vec{r}_i$ (hops on a lattice) to a random walk. For this, the explicit expansion of the mean squared displacement is considered [16, 104]

$$\left\langle R^2 \right\rangle = \sum_{i=1}^{n} \left\langle \vec{r}_i^{\,2} \right\rangle + 2 \sum_{i=1}^{n-1} \sum_{j=i+1}^{n} \left\langle \vec{r}_i \vec{r}_j \right\rangle \tag{3.31}$$

where the left part of Eq. 3.31 refers to the ensemble averaged squared displacement and the right part to the ensemble averaged cross terms. The latter expresses the correlation of every step to all consecutive steps. Considering a pure Markovian random walk, the cross correlation term will vanish in the long time limit and only the ensemble averaged absolute displacement will remain [105]. If follows for the correlation factor [16]

$$f_{\text{corr}} = \lim_{n\to\infty} \frac{\left\langle R^2 \right\rangle}{\left\langle R^2_{\text{random}} \right\rangle} = 1 + 2 \lim_{n\to\infty} \frac{\sum_{i=1}^{n-1} \sum_{j=i+1}^{n} \left\langle \vec{r}_i \vec{r}_j \right\rangle}{\sum_{i=1}^{n} \left\langle \vec{r}_i^{\,2} \right\rangle} \equiv \frac{D^*}{D_{\text{random}}} \tag{3.32}$$

where the left part (+1) of Eq. 3.32 is the Markovian random motion and the right part the normalized correlation term. In general, the right part turns out to be ≤ 0 . This derives from the fact, that the diffusion in crystals is vacancy mediated which will always lead to a back-correlation in the atomic motion. This means that there is always a probability for an hop to be reversed. When treating high-symmetry crystals, the lattice symmetry allows to determine analytical expression for the correlation factors. From these, a rule of thumb was derived depending on the probability of back-correlation which relates to the number of coordinating neighboring sites Z [16]

$$f_{\text{corr}} \approx 1 - \frac{2}{Z}. \tag{3.33}$$

The correlation factor for lattice diffusion in more complex systems are traditionally determined from Monte-Carlo (MC) simulations [105]. Unfortunately, this requires an involved setup for complex systems which is usually beyond any applicability. As an alternative, the same information as obtained in an MC simulation can be extracted from an MD simulation by employing the discretization procedure described in Sec. 3.3.1. This allows for a convenient determination of the correlation factor. In general, correlation factors give characteristic values between 0.45-1.0. These allow to deduce the complexity in a diffusion mechanism or directly to identify the same if an analytical solution is available [16, 91].

A similar concept which is used in solid state ionics is the Haven ratio H_R which relates the charge transport to the tracer diffusion. In comparison to the correlation factor it is universally applicable but only describes a phenomenological quantity for which no analytical expressions are formulated [16, 91, 104]. It defines as

$$H_R \equiv \frac{D^*}{D_\sigma} \tag{3.34}$$

where D_σ represents a charge diffusion coefficient. This latter quantity is not equivalent to a real diffusion coefficient as it does not relate to Fick's law of diffusion. Instead, it is directly correspondent to the exact Nernst-Einstein formulation and can be determined if σ_{DC} is known as

$$D_\sigma = \frac{3Vk_BT\sigma_{DC}}{q^2N}. \tag{3.35}$$

From Eq. 3.34 follows, that the Haven ratio H_R compares tracer diffusion — the diffusion in a chemically homogeneous host — to the diffusion under influence of an electric field. Differences between D^* to D_σ arise from the ion-ion correlation included in the formulation of the conductivity as pointed out in Eq. 3.25. Contained are thereby back-correlation, collective ion motion, as well as effects summarized as conductivity correlation [91]. In most systems, H_R shows values ≤ 1 which derives from the fact, that the electric field induced diffusion adds on top of the tracer diffusion. In traditional crystals based on a vacancy diffusion mechanism $0.5 \leq H_R \leq 1.0$ can be expected [104]. In comparison to that, ion conducting glasses exhibit Haven ratios between 0.1-0.6 which is believed to derive from a broad distribution of migration energies as well as collective ion motion. The latter, originates from the lowered dimensionality of the diffusion network in the glass host structure [104]. To obtain the Haven ratio in an MD simulation, D^* and D_σ need to be determined. The former can be readily obtained by the respective GK or Einstein formulation as described in Sec. 3.3.1. For the latter, σ_{DC} has to be computed first as described in Sec. 3.4 and can then be calculated from Eq. 3.35. In general, the Haven ratio is defined for a single ion species. However, it can also be determined for the net conductivity in a system which relates an idealized to a charge correlated conduction mechanism [96, 106]. For this, the ratio

$$H_R \equiv \frac{\sigma^*_{DC}}{\sigma_{DC}} \tag{3.36}$$

can be determined where σ^*_{DC} represents the correlation-free conductivity as obtained from Eq. 3.26. This Haven ratio of the net conductivity is useful in determining the coupled motion of ionic species of opposite charges.

3.3.2 Defects

Defects determine many material properties and are most relevant for diffusion since vacancies facilitate atom migration. This is true for every diffusion mechanism with the exception of interstitial diffusion which however presents a special case in many regards, anyways. In highly symmetric ionic crystals Frenkel and Schottky defects are the only possibility for defect realization. In the former an ion is displaced from its original position to an interstitial and in the latter an anion-cation pair is missing from the crystal lattice creating two vacancies. Higher structural complexity in the case of transitions metal oxides allows more flexibility. Here, charge neutrality can be compensated by a varying oxidation state of the cations and strong covalent character allows for flexibility in the electronic structure. A usually lower symmetry lattice thereby enables antisite defects (cation exchange) which present irregularities in the usual occupation of crystallographic sites. Finally, ambivalent doping can lead to stabilized vacancies and is often introduced into materials to facilitate ion mobility [16, 24].

In battery materials, these kind of defects may be very relevant for the Li ion mobility. It depends on the composition of the material and its functionality whether and what kind of defects play a role. In intercalation materials intrinsic vacancies are created during the intercalation process which are usually the main facilitator for diffusion [2, 3, 9]. However, in some intercalation compounds defects play a major role where a prominent example are antisite defects in $LiFePO_4$ [24, 107–110]. With the exception of collective conductors like LGPS [111], vacancies created by defects and doping present the charge carriers in most crystalline solid state electrolytes [22, 26, 112]. It follows, that determining the role of defects is a crucial task in understanding the diffusion in battery materials.

The Mott-Littleton method

The Mott-Littleton method presents the most popular approach to calculate defect energies in crystals using computer simulations [38, 113, 114]. It aims at the computation of isolated defects, i.e. in the dilute limit which approximates the case in ionic crystals very well [16]. Here, vacancies, interstitials, or impurities which form the components of a formal defect are evaluated individually.

Thus, charged defects are treated and a cluster approach (no periodic boundary conditions) is used. A large amount of explicit atoms is required to treat the extended reaction of the lattice to a defect in a geometry optimization accurately. Therefore, force field potentials are used for this procedure.

In the computational set up of a model for an isolated defect, the system is split into an inner (1) and outer region (2). In region 1 a defect may be placed and atomic coordinates r are given full flexibility. In comparison to that, the atoms in region 2 are only subject to a displacement ζ within a harmonic potential. This is justified since compensating displacements far away from the defect can be assumed to be small. In the original approach, at the outer boundary of region 2, a continuum model simulates the electrostatic response of the infinite crystal. The dimensions of the individual regions R_X should be in the bounds defined by the cutoff r_{cutoff} of the applied force field as: $r_{\text{cutoff}} < R_1 < (R_2 - R_1) < R_2$. In this setup, the self energy of region 2, i.e. the potential based atom-atom interactions depending on the displacements of the atoms within the harmonic potential, can be neglected from the total energy calculation. Their influence is already included in the interaction energy with region 1 and thus the computational cost of the approach is tremendously reduced [61]. To evaluate the defect energies, it is necessary to compute the system with the perfect lattice and the defect included giving:

$$U_{\text{defect}}(r,\zeta) = U^{\text{tot}}_{\text{defect}}(r,\zeta) - U^{\text{tot}}_{\text{perfect}}(r,\zeta) \tag{3.37}$$

If the actual formation energies are of interest, a correction according to the chemical potential of the isolated removed or added defect species is necessary. In contemporary studies the program GULP [61] is mostly used which includes an efficient implementation of the Mott-Littleton method. Here, the originally applied continuum model is replaced by the sum of the induced polarization in the charged system.

It should be noted, that the treatment of vibrational entropy increases the accuracy of defect energies often in the order of 10 meV. This energy difference may be a decisive factor when deducing the thermal properties of a material. The entropy can be estimated via phonon calculations whereby exact formulations are rigorous in their application [115]. In practice these are therefore rarely applied and contemporary programs include many simplifications [61].

The Mott-Littleton method has been successfully employed in the investigation to many kinds of defects in various material classes [116]. This is also true for studies on battery materials as outlined above [3, 24].

Defect formation probability for non-dilute defects

Battery materials often exhibit low symmetry crystal structures which are prone to disorder. This opens the possibility for stabilization effects, which likely renders the approximation of dilute defects inadequate. This is for example the case in $LiFePO_4$ where a clustering of antisite defects is observed [117, 118]. Additionally, the location of a defect in a disordered material is ambiguous. Here, many possibilities exist to include a dislocation or vacancy which differ in their chemical environments. The associated configurational entropy may be decisive which needs to be estimated by a thorough sampling. In the Mott-Littleton method, interactions between non-dilute defects are not represented and a thorough sampling is not feasible. Therefore, in this thesis defect energies are approximated using periodic cells.

To sample non-dilute defects in periodic cells, all constituents of the defect need to be included into the cell to maintain charge neutrality. It follows that the interactions between defect components as well as the interaction with their periodic images are present. Hereby, the choice of the supercell size formally defines a defect concentration at which long range defect interactions are sampled. Thus, large enough supercells need to be chosen in order to minimize the periodic interaction and also to allow for enough configurational stabilization. To obtain relative energies, defects are randomly introduced into a supercell of configuration Λ followed by a subsequent geometry optimization. This yields a series of relative defect energies $\Delta E^{\text{defect}} = U^{\Lambda,\text{defect}} - U^{\Lambda}$. In the case of neutral, stoichiometric defects like antisite or Frenkel defects these energies correspond to the formation energies. Otherwise a correction may be applied. Sampling enough representatives, a distribution of relative defect energies $C_\Lambda(\Delta E^{\text{defect}})$ can be approximated by a fit to a Gaussian or skewed Gaussian function. Although the latter might give a better fit, the quantitative differences are minute in practice. The resulting distributions are then normalized to yield a defect energy probability $p_\Lambda(\Delta E^{\text{defect}})$

$$p_\Lambda(\Delta E^{\text{defect}}) = \frac{C_\Lambda(\Delta E^{\text{defect}})}{\int_{-\infty}^{\infty} C_\Lambda(\Delta E^{\text{defect}}) d\Delta E}. \tag{3.38}$$

Considering the configurational disorder which allows for a stabilization of non-dilute defects in the first place, many configurations Λ might belong to a relevant thermal ensemble. Hence, this procedure may be repeated for a representative number of configurations from which an averaged probability of relative defect energies is taken $p(\Delta E^{\text{defect}}) = \langle p_\Lambda(\Delta E^{\text{defect}}) \rangle$.

From the approximated defect energy probability a defect formation probability p^{defect} per defect realization at temperature T can be obtained by Boltzmann-weighted integration

$$p^{\text{defect}} = \int_{-\infty}^{\infty} p(\Delta E^{\text{defect}}) \exp(-\Delta E^{\text{defect}}/k_B T)\ d\Delta E^{\text{defect}} \tag{3.39}$$

where k_B is the Boltzmann constant. A defect density ρ^{defect} can then be determined by multiplying with the number of possible realizations m per supercell cell and dividing by the average supercell volume $\langle V_{\text{cell}} \rangle$

$$\rho^{\text{defect}} = \frac{m \cdot p^{\text{defect}}}{\langle V_{\text{cell}} \rangle}. \tag{3.40}$$

It should be noted, that the components of non-dilute defects are in proximity which might lead to a recombination and reinstatement of the original lattice. Therefore, it is necessary to probe for the likelihood of defect recombination using for example NEB calculations. While less important in a case of Schottky or antisite defects, this might be especially relevant for Frenkel defects.

3.3.3 Thermodynamic and mechanic properties for glasses

In the description of glasses, the viscosity and heat capacity are important thermodynamic and mechanical properties. Especially in the characterization of the glass transition they present defining variables [119–121]. With respect to chapter 5, techniques to obtain these from MD simulations are presented in the following.

Shear viscosity

The shear viscosity η is a measure of the ease of flow of a material. It quantifies how layers of a fluid can flow parallel to each other with different velocities. Microscopically, this relates to the propensity of a fluid to transmit momentum in a direction perpendicular to the direction of velocity or momentum flow. This multiparticle reaction can be expressed by the off-diagonal elements of the stress tensor $\sigma_{\alpha\beta}$, hence an infinitesimal coordinate deformation. A linear response can therefore be defined relating the perpendicular gradient of a velocity $\frac{\partial v_\alpha}{\partial \beta}$ to the deformation proportional to $\sigma_{\alpha\beta}$. From this, a GK relation can be derived [28, 29]

$$\eta = \frac{1}{k_B T V} \int_0^\infty \langle \sigma_{\alpha\beta}(t) \sigma_{\alpha\beta}(0) \rangle dt \tag{3.41}$$

Since the stress tensor elements are multiparticle properties, this time correlation function is slowly converging. One hence averages over all three off-diagonal components σ_{xy}, σ_{xz}, and σ_{yz} which leads to a noticeable improvement. In practice, this method works well for liquids. In contrast to this, in highly viscous materials or solids the correlation times exceed any reasonable computer time. Thus, one resorts to approximate the convergence. Similar to other slowly converging properties the autocorrelation function shows a mixture of an exponential and linear decay [92]. After simulating for a long enough correlation period which allows to estimate the function profile, the autocorrelation function can be fitted and an integral approximated. As discussed in Sec. 5.4, such a procedure is, however, not very robust and conveys large errors. Nevertheless, the relevant order of magnitude defining a material as a liquid or a glass can be estimated.

Alternatively to the GK description of the viscosity, there is an Einstein formalism for equilibrium MD simulations [28]. Furthermore, non-equilibrium MD simulations provide direct means of measuring the shear stress and obtain the viscosity. Although more accurate in the case of solids, these simulations include long simulation times and involved computational setups [122]. It should be mentioned that the bulk viscosity can be similarly obtained via an GK or Einstein approach based on the diagonal components of the stress tensor $\sigma_{\alpha\alpha}$. Here, a correction must be applied to compensate for non-vanishing equilibrium averages [28].

Heat capacity

The specific heat capacity describes the change in energy of a system with temperature. Here, one differentiates between two relevant thermodynamic ensembles, i.e. a heat capacity at constant volume C_V and constant pressure C_P. These are defined as $C_V = \left(\delta E / \delta T\right)_V$ and $C_P = \left(\delta E / \delta T\right)_P$, respectively. The heat capacity can be directly obtained from MD simulations. Here, the fluctuations, i.e. the mean changes around the equilibrium of the total energy E_{tot} are considered. It follows for C_V [28]:

$$\langle \delta E_{\text{tot}}^2 \rangle_{NVT} = \langle E_{\text{tot}}^2 \rangle_{NVT} - \langle E_{\text{tot}} \rangle_{NVT}^2 = k_B T^2 C_V. \tag{3.42}$$

The total energy term contains the potential energy E_{pot} and kinetic energy E_{kin} which need to be treated uncorrelated as:

$$\langle \delta E_{\text{tot}}^2 \rangle_{NVT} = \langle \delta E_{\text{pot}}^2 \rangle_{NVT} + \langle \delta E_{\text{kin}}^2 \rangle_{NVT}. \tag{3.43}$$

The corresponding heat capacity at constant pressure is calculated from the instantaneous enthalpy $E_{\text{tot}} + PV$. Here it follows:

$$\langle \delta (E_{\text{tot}} + PV)^2 \rangle_{NPT} = k_B T^2 C_P. \tag{3.44}$$

Again the uncorrelated terms $\langle \delta E_{\mathrm{tot}}^2 \rangle_{NPT}$, $\langle \delta V^2 \rangle_{NPT}$, and the correlation term $\langle \delta E_{\mathrm{tot}} \delta V \rangle_{NPT}$ should be considered individually [28]. In general, the simulation from which the instantaneous quantities are sampled needs to insure to capture sufficient configurational relaxation events to get a good representation of the heat capacity. Thus sampling lengths need to be checked for convergence.

When comparing heat capacities to experimental values or trends, the most appropriate comparison will give a heat capacity at constant pressure which is usually measured based on ambient conditions. However, simulations are often limited to the NVT ensemble, where this property cannot be obtained (see Sec. 5.4). Notwithstanding, a relative comparison is still possible. In that, C_P will be quantitatively lower than C_V. This is based on the work of expansion in the NPT ensemble which leads to a lowered thermal energy. In comparing different systems, e.g. a crystal and a glass, expected trends should remain constant. Here, the internal energy restraining a system from expansion will similarly restrain it from configurational sampling — both effects will lead to equal trends in the fluctuations of the energy $\langle \delta E^2 \rangle$.

4 Occupational disorder and ion mobility in $Li_4Ti_5O_{12}$ battery materials [‡]

The focus of this chapter is to elaborate the influence of disorder in a Li ion conducting and intercalating crystalline material with the example of lithium-titanium-oxide ($Li_4Ti_5O_{12}$, LTO). Crystals may exhibit an inherent disorder in their bulk structure due to partial or mixed occupation of crystallographic sites. A rich configuration space may result, depending on the underlying crystal symmetry. This potentially complicates the already involved ion diffusion in Li intercalating materials. Already without such disorder, the applicability of dilute ion diffusion theory is not given, i.e. the assumption that one rate-limiting microscopic migration barrier is relevant for macroscopic diffusion in an Arrhenius-type relation [9, 16]. Instead, varying chemical environments can be expected which yield many competing microscopic activation barriers. In any intercalation material this arises from interacting Li ions which effectively change with concentration throughout the lithiation process (see Sec. 3.3.1) [2, 9]. In the meantime, occupational disorder will add yet another layer of complexity to the ion diffusion [10]. In contemporary computational studies, the investigation of such disorder and its configuration space is, however, always limited to a few stable configurations at most. Therefore, no computational strategy has so far been designed to systematically investigate possible relationships arising between occupational disorder and Li ion transport.

4.1 Introduction

The commercialized anode material LTO is unique among battery materials due to its exceptional cyclability and high rate capability. The latter has even been shown to exhibit record-breaking quantities allowing for rapid dis-/charging in high current applications. The good cyclability of LTO is found to result microscopically, from a zero-strain behavior. Here, the lattice constant of the non-intercalated phase $Li_4Ti_5O_{12}$ and the intercalated phase $Li_7Ti_5O_{12}$ shows variations of less then 1 % [11, 12, 18, 123]. In contrast to that, the high rate performance is owed to micro or nano sized particles with an increased surface area for lithium uptake on the one hand and to a fast intrinsic Li transport on the other [18, 124–127]. For this latter microscopic property a number of largely controversial findings have hitherto prevented a clear atomistic understanding.

On the atomic scale, rate capability arises from Li insertion. The latter critically depends on Li ion diffusion and electron conduction in the bulk, as well as on interfacial processes between intercalated and non-intercalated phases [9, 25, 128]. Due to the mutual influence of these transport phenomena, an involved complexity of the insertion process can be anticipated. This is in fact the case for LTO, where a strongly varying Li ion mobility with Li concentration according to the battery charge state is observed [129, 130]. During charging, the occuring phase transformation from $Li_4Ti_5O_{12}$ to $Li_7Ti_5O_{12}$ leads to a dramatic increase in electronic conductivity from an insulator

---

[‡] Adapted in parts with permission from Ref. [1]. © 2017 American Chemical Society.

at 10^{-7} to a conductor at 10^{-1} S cm^{-1} [131]. Additionally, $Li_7Ti_5O_{12}$ forms a separated phase in operational (non-equilibrium) conditions [132–135]. Based on this, an intercalation mechanism has been linked to a $Li_7Ti_5O_{12}$ phase forming an electron conducting network in the pristine material which aids Li ion transport into the bulk [136]. Recently, respective Li percolation channels have been detected within primary grains which elucidate a $Li_7Ti_5O_{12}$ phase growth as a spatially non-homogeneous, non-surface bound process [137]. A likely origin of the formation of these inhomogeneous percolation channels may lie in the occupational disorder of LTO or more specifically, in the atomistic relationships following therein.

Computational atomistic simulations are a suitable means to resolve the length and timescales of Li transport. Many studies thereby focus on the elementary processes, considered the basic building block for the ionic diffusion [2, 10, 16] (see Sec. 3.3.1). This strategy targeting simplified elementary steps might, however, miss decisive details of the collective motion following long range charge carrier interactions. Additionally, such studies are mostly conducted in periodic crystal models describing a highly symmetric, infinitely extended bulk. Here, significant difficulties are encountered when depicting disordered structures, which are unfortunately common for Li ion battery materials. These challenges are also met in the occupational disorder of LTO. The latter is defined by a spinel-like structure following the $Fd\bar{3}m$ space group where oxygen ions form a distorted fcc lattice. Tetrahedral $8a$ sites are occupied by Li ions and octahedral $16d$ sites are occupied by Li and Ti ions with a ratio of 1:5 which can be expressed as $Li_3^{8a}(Li_{1/5}Ti_{5/6})_6^{16d}O_{12}$ [138, 139]. The mixed occupation of the octahedral sites opens up a combinatorial space which results in an unseizable amount of possible structures. First-principle studies — albeit providing useful insight into thermodynamics and kinetics [11, 12, 123, 140] — have hitherto neglected a detailed treatment of this structural ensemble and its effect. However, it is very likely that this might impact the diffusion behavior. Already in the corresponding ideal spinel stoichiometry of $LiTi_2O_4$ ($Li_3Ti_6O_{12}$) which is not subject to a mixed occupation of the $16d$ sites (only Ti occupation), involved relationships arise. A multitude of different local environments creates a multitude of interrelated microscopic diffusion barriers in the three-dimensional diffusion network spanned between the $8a$ sites [10, 32].

In this work [1], the configurational ensemble in the pristine LTO spinel accessible during high-temperature LTO synthesis is explored and rationalized. This is facilitated via Monte Carlo techniques based on a numerically efficient, DFT validated interatomic potential [141]. Realistic nanoscopic structures are obtained which feature a high degree of configurational disorder. This in turn stabilizes a manifold of possible microscopic occupation patterns even including Ti^{16c} antisite defects. In a second step, the Li ion mobility is probed via MD simulations at a broad temperature range. Around defects, localized and correlated interstitialcy-like diffusion occurs which however appears isolated at 300 K and is therefore only complementary to the regularly assumed vacancy mediated diffusion [2, 9]. Nevertheless, a likely relation to Li migration during the intercalation processes can be made. This provides a reasonable atomistic explanation for the recently observed Li transport phenomena (see above) which form the basis for the extraordinary rate capability of this material. Additionally, effects at high temperatures (600 K) are evaluated where separately initiated localized mobility regions overlap and diffusion thus becomes non-local. This compares well to an experimentally and theoretically characterized surge in the diffusion coefficient by three orders of magnitude at temperatures above 600 K [141–143].

4.2 Computational details

All DFT reference calculations are conducted using the FHI-aims code [144]. The PBE functional is used and electronic states are described with an all-electron basis set as implemented in the FHI-aims code. Gaussian occupation type broadening of 0.2 eV is enforced. The electronic structure is converged until a total energy convergence of 10^{-5} eV and self-consistend forces until 10^{-3} eV/Å. Structures are relaxed via a BFGS optimizer until residual forces are less than 10^{-2} eV/Å. All calculations are conducted periodically where the Brillouin zone is sampled with a Γ-point centered Monkhorst-Pack grid [145]. The k-point grid and basis set accuracy are chosen according to structural dimensions. For the configuration space and defect references (see Sec. 4.3.1), a "tight" basis set as well as a $4 \times 4 \times 2$ k-point grid for the $1 \times 1 \times 1$ and a $3 \times 3 \times 2$ k-point grid for the $2 \times 2 \times 1$ supercells of the $R\bar{3}m$ representations of LTO are chosen. The larger structures including up to 350 atoms for the validation of the defect stability (see Sec. 4.3.2) are computed with a "light" basis set as well as a $2 \times 2 \times 2$ k-point grid in order to account for the increased computational cost.

All force field based calculations are performed using the code package LAMMPS [58] developed at Sandia National Labs. The potential terms applied in this study are based on the Born model of ionic solids [39] using a pair potential including a term describing Coulomb, short-range repulsion and van der Waals interactions as described in Sec. 2.2.1. To include polarization, the core/shell model is applied (see Sec. 2.2.2). Parameters for the Buckingham potential and the shell model for $Li_4Ti_5O_{12}$ have been adopted from Kerisit *et al.* [141]. In $Li_4Ti_5O_{12}$, only the O^{2-} ions are treated as polarizable ions. In accordance with the primary literature/potential, a cutoff of 9 Å is chosen for the short range interactions and periodic boundary conditions are applied where the Coulombic long-range forces are treated by a particle-particle particle-mesh solver [146]. The employed potential parameters are validated for the treatment of the configuration space and the description of Ti^{16c} antisite defects as shown in Sec. 4.3.

All presented geometry optimizations follow a two step protocol to avoid artifacts appearing due to gradients induced by a strong core/shell interaction which occasionally appears in high symmetry structures. In the first step only the atom positions are optimized without allowing the core/shell degree of freedom (DOF) to relax. In the second step atom positions, core/shell DOFs and the cell constant are allowed to relax. The obtained structures are evaluated for glass-like distortions which are occasionally found at high energies. Non-crystalline structures are identified via cell volume deviation of more than 3 % from the experimental value and deviation of the first two coordination spheres in the O-O radial distribution function (RDF) from the ideal fcc coordination spheres (more than 1.75 and 2.75 atoms respectively). To evaluate the crystallographic configuration after a geometry optimization, structures are discretized via a projection onto the fcc crystal lattice as described in Sec. 3.3.1. In comparison to the MD based method, a distortion of the lattice is compensated in accordance to the displacement of the oxygen ions during the geometry optimization.

For all presented NEB calculations, a harmonic NEB interaction force between images of 0.5 eV/Å is applied and a convergence criterion of 0.02 eV/Å between image interaction is set. By including only ions in the vicinity of the investigated event into the NEB image interaction, artificial long range effects are avoided.

Images of crystal structures and atomic depictions are created with VESTA [147] and the atomic-simulation-environment (ASE) [66].

4.2.1 Details for the Wang-Landau sampling

A predetermined energy range for the sampling is discretized into energy bins, each representing a cDOS entry as desribed in Sec. 3.2.2. Hereby, the number of bins is chosen proportional to the number of sampled lattice sites in our model [82] leading to a bin width of 0.18 eV per atom. Due to the rough energy landscape encountered in the configurational space of $Li_4Ti_5O_{12}$ and the high computational cost following the large number of performed geometry optimizations, sampling parameters are adjusted. A localized search is avoided by drawing new structures randomly from the priorly assessed configuration space after 100 consecutive non-accepted steps as established in [82]. Additionally, a low flatness criterion of 50 % is chosen and checked every interval of 100 MC times (MC time = trial MC steps / bins) instead of the usual flatness of 80-95 % and an interval of 1000 MC times [82, 84, 85] (compare Sec. 3.2.2). This leads to an earlier convergence of each refining cycle. In comparing to the usual sampling criteria (here flatness of 80 % and interval of 1000 MC time) for the low end of the energy range as shown in Fig. 4.1, a deviation of the cDOS ($g(E)$) is only found in the first 5-7 sampling cycles. Here, it can be seen that the tightly chosen standard criteria lead to a similarly irregular $g(E)$ in the early stages of the sampling. Close to convergence, the resulting $g(E)$ are equivalent whereby the standard sampling criteria exhibit an increased computational cost of two orders in magnitude.

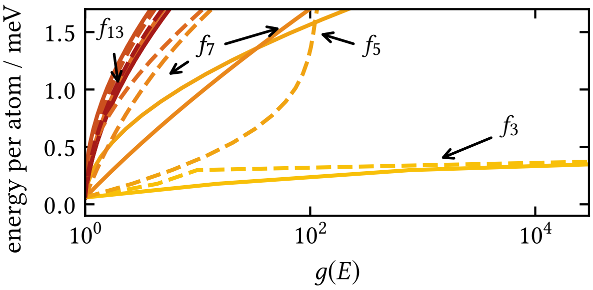

Fig. 4.1: Comparison of the convergence of $g(E)$ with different sampling criteria (see text). Compared are the light sampling criteria applied in the present work (solid lines) and the standard sampling criteria (dashed lines). The convergence is depicted in terms of the refining parameters f_i whereby cycles are colored from yellow to red in ascending order and selected cycles are labeled.

A further adjustment in the sampling is a rather light final convergence criterion of $f_{\text{final}} = \exp(10^{-4})$ which differs from $f_{\text{final}} = \exp(10^{-6}) - \exp(10^{-8})$ as often applied for the Ising model. The early convergence coincides with the beginning of the so-called 1/t domain where gained accuracy with simulation time decreases [85, 88]. The target property as obtained from $g(E)$ is a canonical distribution $P(E, T) = g(E)e^{-E/k_B T}$ at a temperature T, where k_B it the Boltzmann constant. In that, the dominating contribution of the Boltzmann factor drowns the incremental higher accuracy gained at late refinement cycles via a small f as shown in Fig. 4.2. This justifies an applied early f_{final}.

The sampling is trivially parallelized as described in Sec. 3.2.2 using 33 random walkers each covering 14 bins, thus leading to an overlap of four bins between adjacent walkers. Starting configurations for each walker in its respective energy range are drawn from the pre-sampling. To capture boundary effects, steps outside the assigned range are counted into the originating bin [83]. In joining the individual $g(E)$ from each walker a procedure using a spline interpolation is used.

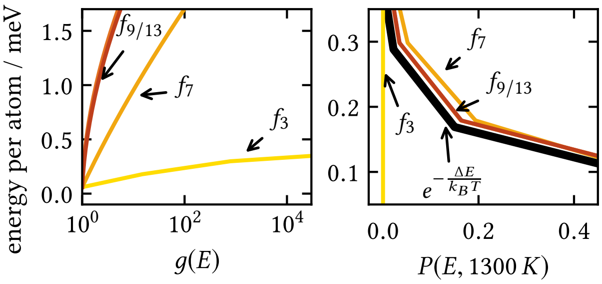

Fig. 4.2: (left) Convergence of $g(E)$ and (right) its effect on the relative canonical distribution $P(E, T)$ in comparison to the Boltzmann factor e^{-E/k_BT} (black) at 1300 K. Shown are exemplarily the third (f_3), seventh (f_7), ninth (f_9) and thirteenth (f_{13}) sampling cycle (from yellow to red). Note that the maximum of $P(E, T)$ belonging to the third cycle is at higher energies which is not within the limits of the diagram.

4.2.2 Details for the MD simulations

MD simulations are carried out with a time integration by the Verlet algorithm [148] using a timestep of 0.2 fs. In order to propagate the core/shell particles, the shells are given a mass of 0.2 u [141] and their motion is integrated following the adiabatic core/shell model by Mitchell and Fincham [53] (see Sec. 2.3.3). Equilibration is performed in an NPT ensemble applying a Nose-Hoover chain thermostat and a Hoover chain barostat [148, 149], where the cell constant is allowed to vary. The overall center-of-mass of the system is fixed by a correction of the velocities to compensate for an observed minute translation of the system originating from numerical imprecision in the decoupling of the relative core/shell motion during equilibration. Production runs are conducted in the NVE ensemble as thermostating is not necessary because observed thermalization rates of the relative core/shell motion are in no case higher than $4.0 \cdot 10^{-4}\,\mathrm{K\,ps^{-1}}$ up to a temperature of 600 K, which is well below the average literature value of $1.0\,\mathrm{K\,ps^{-1}}$ by Mitchell and Fincham [53]. For each investigated configuration and temperature, 7 simulations are performed incorporating an equilibration of 50 ps and a production run of 1.95 ns. In order to investigate only the diffusive regime, data sampling was commenced after 250 ps. A sufficient simulation length in terms of diffusion correlation is ensured by a prior analysis via block-averaging. To assess the microscopic information of the diffusion processes, snapshots of the trajectories are discretized as described in Sec. 3.3.1. To filter recrossing events, core sets around each crystal position are defined with an acceptance radius of 0.55 Å compared to the smallest distance between adjacent tetrahedral and octahedral sites of d_{Td-Oh} =1.8 Å [100, 101].

NEB calculations on the force field level are employed to investigate rare migration events identified from the discretized trajectories (see above) as an ion hops over two interstitial sites. From the first to last involved snapshot, 7-11 images are constructed depending on the length of the estimated diffusion path. Similarly, processes resembling the observed rare-events are embedded by linear interpolation of an assumed first and last snapshot with the same number of images. Using this procedure all rare events found in MD trajectories for temperatures of 300-400 K and randomly chosen events for 500 K and 600 K are investigated. The latter is constrained since the sheer amount of identified events for the higher temperatures is too large to be computed in its entirety.

4.3 Force field validation

The employed force field potential by Kerisit *et al.* is an extention to a TiO_2 force field by Matsui and Akaogi [150] to incorporate Li. The interaction parameters were derived based on the lattice constants and bulk modulus of Li_2O and lithiated rutile [151, 152]. Shell model constants are directly obtained from reorganization energies following charge transfer in rutile (see equation. 2.10). Hereby, electronic structure calculations provide reference data for the training procedure [68]. The resulting description of ternary compounds has shown to successfully reproduce thermodynamic and kinetic properties of lithiated phases of the TiO_2 polymorphs [151, 153], Li_2TiO_3 [152] and $Li_4Ti_5O_{12}$ [141]. Here, only minor discrepancies are seen in the elastic constants for a fraction of investigated polymorphs. Nevertheless, based on a restricted parameterization of Li-O interactions to a tetrahedral O coordination and the special purposes of this work, an additional validation is shown in the following.

4.3.1 Occupational disorder in a minimal cell

A major goal of this work is the investigation of the occupational disorder. To validate a good reproduction of the latter by the employed force field potential, relative energies and forces for different configurations are compared to DFT via geometry optimizations. For this, the full configuration space of a $1 \times 1 \times 1$ supercell in the R$\bar{3}$m space group is tested. This presents the smallest possible stoichiometric representation with a chemical formula of $Li_8Ti_{10}O_{24}$. The mixed occupancy of the $R\bar{3}m$ representation only encompasses the distribution of 2 Li and 10 Ti ions on the octahedral sites which yields $12!/(10! \times 2!) = 66$ possible configurations. These can be further reduced to 6 inequivalent configurations due to symmetry (see Fig. 4.3) [1, 11].

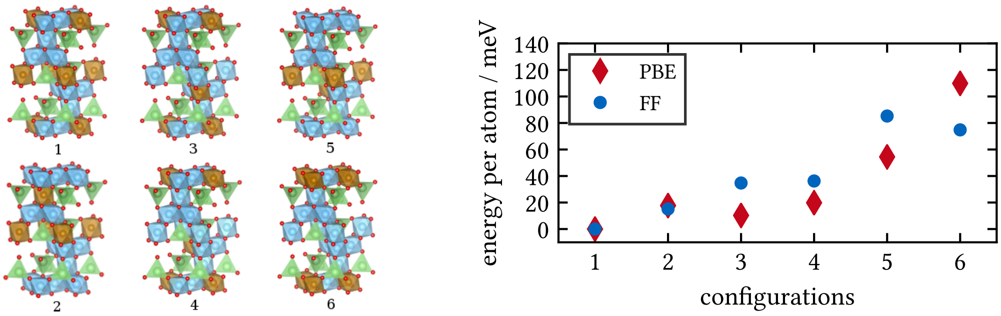

Fig. 4.3: (left) Symmetry inequivalent configurations of $Li_8Ti_{10}O_{24}$ in the $R\bar{3}m$ space group. Oxygen is shown in red, Ti in octahedral sites in blue, Li in octahedral sites in gold and Li in tetrahedral sites in green. (right) Comparison of the relative energies of the geometry optimized symmetry inequivalent configurations of $Li_8Ti_{10}O_{24}$. The energies are referenced to the minimum energy configuration 1 of the potential (blue) and DFT-PBE (red), respectively. Adapted with permission from Ref. [1]. © 2017 American Chemical Society.

For DFT and potential based calculations, atomic positions are initialized based on the experimental crystallographic positions and lattice parameters [138], and thereafter relaxed. This way, the optimized structures give an unbiased representation of the local minima in a PES. As shown in Fig. 4.3, the relative energies of configurations 1-6 optimized via DFT and the employed potential show a slight deviation. Although the general trend of the energetic order is reproduced, energetically close lying structures yield a reversed order for the configurations 2-3 and 5-6.

It should be noted, that these deviations occur at an energy range exceeding the energies for the relevant configuration space (see Sec. 4.4). Hence, these configurations represent especially unfavorable structures where the electronic structure in the small periodic cell will be able to exert compensating polarization effects which are not accordingly mimicked by the core/shell model. As shown in the next section, the deviations in larger supercells are fundamentally smaller. Therefore, the correct general trend and the good reproduction at low energies ensures that the force field potential yields sufficiently accurate energetics and forces for the description of the occupational disorder. [1]

4.3.2 *Ti^{16c} antisite defect validation*

In this work novel Ti^{16c} defects are discovered during extensive structural sampling by means of the employed force field potential (see Sec. 4.4). Thus, these defects also require validation since they were not included in the original force field parameterization.

Defect predictability

Defects are investigated in the $1\times1\times1$ and $2\times2\times1$ supercell of the lowest energy configuration in the $R\bar{3}m$ space group representation (denoted 1, see above in Sec. 4.3.1). For this, a prior systematic screening of all possible Ti^{16c} defects is conducted performing geometry optimizations based on the force field potential to retrieve stable defects. Randomly chosen low energy candidates (denoted $a, b, c, \dots$) are then re-optimized using DFT to establish their stability on the *ab initio* PES. All probed defects remain stable and thus represent local minima at the DFT level, thereby confirming a reliable force prediction of the employed potential. In comparing the resulting relative energies referenced to the defect-free configuration as shown in Fig. 4.4, a profound size dependent deviation is seen. In the small $1 \times 1 \times 1$ supercell, defects appear at considerably lower energies in the force field potential which translates to an overestimation of thermodynamic stability. In comparison to that, in the larger $2 \times 2 \times 1$ supercell large deviations disappear. In fact, either relative energies coincide remarkably well or the defect stability is even underestimated by the force field. Peculiarly, two of the defects show higher stability than the regular LTO configuration evident of an insufficient depiction of LTO in small supercells. It can be concluded, that the observed systematic overestimation of relative energies in the $1 \times 1 \times 1$ supercell and the overestimation of defect stability in some candidate structures in the $2 \times 2 \times 1$ supercell derive from electronic defect-defect interactions. This can be qualitatively confirmed by Mulliken charge analysis which shows that some charge transfer on DFT level occurs [1].

The defect predictability of the employed force field is assessed as adequate. Defects remain stable on the DFT PES and relative energies of defects that do not include artificial charge transfer are predicted with high accuracy. Although the force field might fail to describe the charge transfer resulting from the defect-defect interactions which is unlikely in larger cells, this strictly leads to energy stabilization effects. Thus the force field will only underestimate defect formation. The case of strong defect-defect interactions as in the small $1 \times 1 \times 1$ supercell, where the force field problematically overestimates defect stability is hereby neglected. This is due to the reason that these cells can only represent extremely high defect concentrations which are found non-probable (see Sec. 4.4) [1].

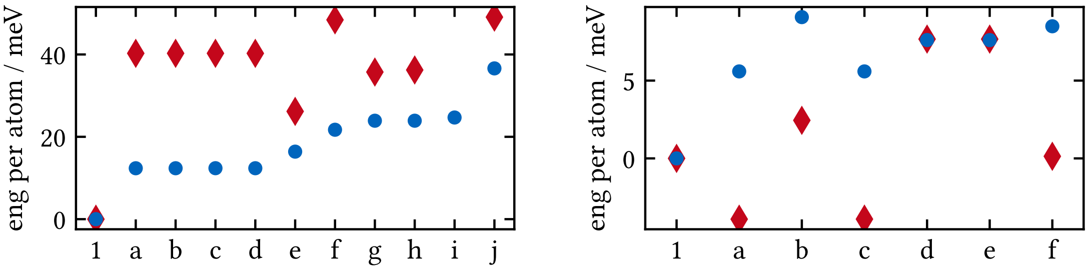

Fig. 4.4: Comparative calculations by means of the interatomic potential and DFT calculations for randomly chosen, stable Ti^{16c} defect candidate structures $a, b, c, \ldots$ referenced to the according defect free structure 1 for a $1 \times 1 \times 1$ (left) and $2 \times 2 \times 1$ supercell (right). Blue circles represent geometry optimizations on force field level, the red diamonds on DFT level. Adapted with permission from Ref. [1]. © 2017 American Chemical Society.

Thermal stability of defects

In MD simulations Ti^{16c} defects remain stable against a relaxation to the original (usually more favorable) regular LTO configuration (see Sec. 4.5). Here, a possible deactivation is associated with a large energetic barrier in the force field potential as shown by NEB calculations (see Sec. 4.4). To evaluate this general observation as predicted by the force field potential, a comparison on DFT level is conducted. Here, one obtained deactivation path of a NEB calculation showing a

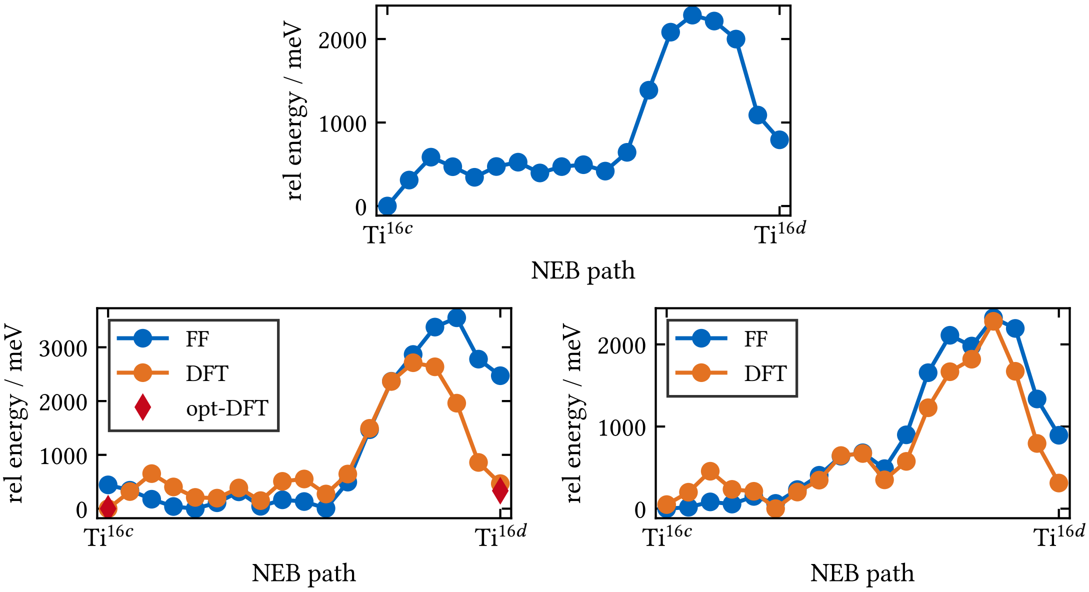

Fig. 4.5: Relative energies of the Ti^{16c} defect deactivation pathway on basis of a NEB calculation on force field level (blue) in a sampled configuration with the formula $\mathrm{Li}_{288}\mathrm{Ti}_{360}\mathrm{O}_{864}$ (top). Relative single point energies at DFT (orange) and force field level (blue) of the according NEB-images isolated in truncated cells in a $\mathrm{Li}_{64}\mathrm{Ti}_{80}\mathrm{O}_{192}$ structure (bottom left) and a $\mathrm{Li}_{36}\mathrm{Ti}_{45}\mathrm{O}_{108}$ structure (bottom right). The two local minima defined by the Ti ions in either the 16c or 16d site are marked on the x-axis. Adapted with permission from Ref. [1]. © 2017 American Chemical Society.

typical barrier is selected for comparison. Since the original cell which contains 1512 atoms is too large for a DFT calculation, the simulation cell is truncated to isolate the atomic arrangement depicting the deactivation pathway. It is ensured, that the cut-out cell remains stoichiometric and maintains an fcc lattice. This is done for each image of the deactivation path and a subsequent DFT and force field single point calculation is conducted. As shown in Fig. 4.5 for two different cut-out cells, the force field single point energies in the truncated cells reproduce the original barrier satisfactorily, validating this approach for a comparison. The according relative DFT energies coincide qualitatively with the force field derived barriers. Although allowing for a lower energy transition, they still give barriers in excess of 2.3 eV confirming thermal stability. It can be concluded, that the force field potential predicts the thermal stability Ti^{16c} defects well reflecting again a high accuracy in the description of LTO.

4.4 Sampling of the configuration space

4.4.1 Obtaining a representative ensemble of LTO

The occupational disorder of $\mathrm{Li_4Ti_5O_{12}}$ is explored via Metropolis Monte Carlo [29] and Wang-Landau sampling [82–85, 87, 88] as described in Sec. 3.2. For this, large simulation cells are employed to account for long-range effects. These consist of a $(3 \times 3 \times 3)$ Fd$\bar{3}$m super cell containing a total of 1512 atoms (according to $\mathrm{Li_{288}Ti_{360}O_{864}}$). In both samplings, new configurations are created at each step by interchanging a Li with a Ti ion on an octahedral 16*d* site and subsequently optimizing their geometries starting from an ideal fcc lattice. Although increasing the computational cost substantially, the geometry optimizations prove crucial in determining structural stabilization based on the long range effects of the disorder.

A pre-sampling to assess the relevant total energy range and estimate the expected disorder is based on the Metropolis acceptance criterion. To sample the corrugated energy landscape of the occupational disorder in its full range, ultra-high temperatures (700, 1800 and 4000 K) are used which allow for a quasi-global screening. Based on the energy range obtained from resulting 900,000 structures, the relative cDOS ($g(E)$) is approximated by a Wang-Landau sampling (see details in Sec. 4.2.1). From the obtained cDOS which links the potential energy of a structure to its relative probability, the canonical distributions can be estimated via $P(E,T) = g(E)e^{-E/k_BT}$ where k_B is the Boltzmann constant and T is the temperature [82–85, 87, 88] (see Sec. 3.2.2). Since LTO synthesis protocols include a rapid cool-down which freezes-in structures formed at high temperatures, a realistic mesoscopic ensemble of LTO is estimated from distributions of the minimum and maximum synthesis temperatures T_S at 700 and 1300 K [18, 127, 141, 154–157].

As shown in Figure 4.6, the accessible canonical distributions $P(E, T_S)$ extend over a narrow energy range with a sharp maximum at low energies and a tail extending to higher energies. Contained configurations exhibit a considerable degree of disorder based on a variety of microscopic motifs with respect to the mixed occupancy of Ti and Li on octahedral 16*d* sites. In Figure 4.7, this is illustrated by comparing the Li^{16d}-Li^{16d} radial distribution functions (RDFs) of three randomly chosen configurations from the canonical distributions to handpicked reference structures (see Fig. 4.6). Included in the latter are the four lowest energy configurations found in the smallest stoichiometric representation of LTO in the R$\bar{3}$m space group [1, 11, 158] and a recently identified lowest energy configuration “C1” realized within a $(3 \times 1 \times 1)$ Fd$\bar{3}$m unit cell [123, 140]. For an appropriate comparison, the reference structures are periodically repeated to match the employed supercell size and shape. The R$\bar{3}$m structures represent high symmetry configurations incorporat-

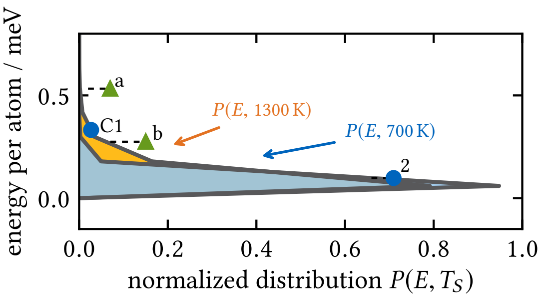

Fig. 4.6: Relative canonical distributions at 700 K (lightblue area) and 1300 K (orange area). The relative energies of the configurations C1, 2 (blue circles) and a, b (green triangles) analyzed via MD simulations (see Sec. 4.5) are marked.

ing a limited number of microscopic motifs and "C1" corresponds to a structure where octahedral lithium ions are arranged in a regular pattern giving the largest Li^{16d}-Li^{16d} distances. In the RDFs, the disordered configurations show a constant number of broadened peaks with variation found in the intensity fingerprint reflecting different combinations of all possible coordination shells of the Li^{16d} ions. In contrast to this, the high symmetry configurations (R$\bar{3}$m) each give a subset of these coordination shells with a sharp signal. Thus, motifs which appear energetically unfavorable in high symmetry representations are found to accommodate each other in locally disordered configurations. Similarly, "C1" exhibits sharp peaks and a missing coordination shell at 6.0 and 10.3 Å corresponding to its ordered occupation pattern. Although "C1" is already found at a low energy, further stabilization of this ordered pattern is possible with increasing disorder.

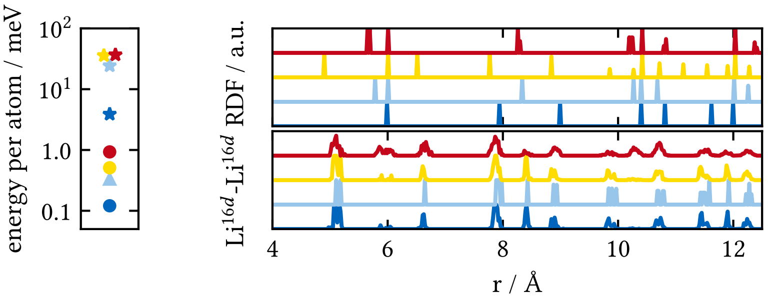

Fig. 4.7: (left) Relative energetic position and (right) comparison of the Li^{16d}-Li^{16d} radial distribution functions of the four lowest energy R$\bar{3}$m structures (stars, top), to three randomly chosen configurations from the thermal ensemble and the configuration "C1" (circles and triangle respectively, bottom).

It can be summarized from the comparison of the Li^{16d}-Li^{16d} RDFs, that LTO will mesoscopically feature a rather distinct intrinsic inhomogeneity with widely changing local Li and Ti distributions. Disorder-stabilized configurational motifs, such as found here, are likely to render the accuracy of extrapolating methods like cluster expansion [2] unsuitable for describing the disorder in these materials.

4.4.2 Ti^{16c} antisite defects

The observed disorder related stabilization described above (Sec. 4.4.1) extends to more rigorous structural changes. Here, disruptions of the regular occupation pattern can be found in Ti^{16c}

antisite defects [1]. These defects are characterized by a displacement of a Ti ion from a 16d to a 16c site followed by a shift of a Li ion on an adjacent 8a site to the original 16d site as illustrated in Fig. 4.8. A possible relaxation of this atomic arrangement to a defect-free configuration at finite temperatures is kinetically hindered. In order to show this, all possible deactivation pathways of a Ti ion from a 16*c* to a neighboring 16*d* site are investigated using NEB calculations with 15-20 interpolated images (see Sec. 4.3.2). The resulting activation energies are in excess of 2.3 eV. These high barriers can be associated with the transition of the Ti ion through a narrow tetrahedral coordinated 48*f* site [1]. Due to this bottleneck, these defects are considered as permanent irregularities of the crystal lattice [1].

Considering a quantitative influence on the material properties, the defect concentration is estimated from relative formation energies $\Delta E^{\mathrm{Ti}^{16c}}$. Since the defects are stoichiometric (and thus charge-neutral), formation energies can be determined from their relative energy referenced to the respective defect free structure. These are probed in a series of geometry optimizations of randomly introduced defects into randomly selected configurations. This way, a distribution of relative defect formation energies $p_{E_i}(\Delta E^{\mathrm{Ti}^{16c}})$ can be approximated (see Sec. 3.3.2). In order to assess defect interactions, defect pairs and triplets are additionally investigated. In an initial extensive sampling in few configurations, 99 % of the introduced single defects remained stable revealing a (slightly) skewed normal distribution of formation energies in each configuration as shown in Fig. 4.8. In contrast to this, only 2 % and less than 1 % of defect pairs and triplets remained stable at very high energies from which it can be concluded that any close range interactions are destabilizing and therefore negligible.

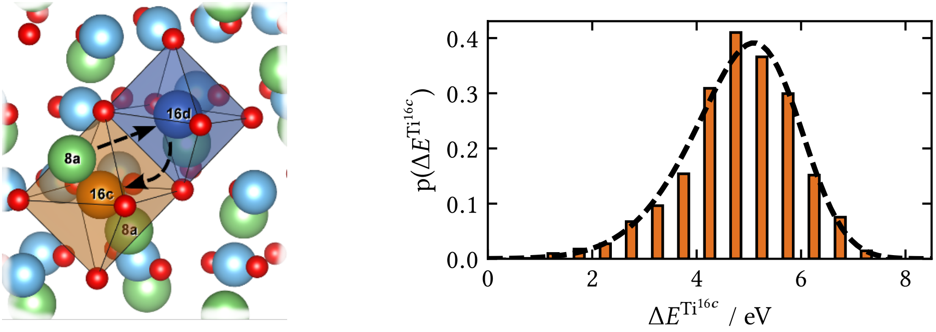

Fig. 4.8: (left) Ti^{16c} antisite defect arrangement (as labeled) in the LTO crystal lattice with oxygen ions in red, Li ions in green and Ti ions in light blue. (right) Typical relative defect formation energy distribution $p(\Delta E^{\mathrm{Ti}^{16c}})$ found in a single configuration.

Following this insight, a representative number of distributions is then fitted to sets of 100 sampled single defects per configuration. In order to relate the distributions to the energetic probability of the respective configurations, a relation to the energy bins E_i of the configurational DOS $g(E_i)$ is established (see Sec. 4.2.1). The sampled distributions within each bin E_i show only little variation of 8 % for the mean, 10 % for the standard deviation and 30 % for the skewness. Similarly an equally small variation with a maximum of 2 %, 9 % and 15 % for the mean, standard deviation and skewness for the average distributions of all bins belonging to the relevant energy range is seen. Hence, averaging of the defect formation energy distributions $p(\Delta E^{\mathrm{Ti}^{16c}})$ for the thermal ensemble is permissible. Note, that this generalization does not work for the whole configuration space since high energy configurations show distributions extending to considerably lower, even negative, formation energies. From the approximated distributions a defect formation probability $p^{\mathrm{Ti}^{16c}}$ per defect realization can be obtained for a given temperature T by integration over the Boltzmann factor as described in detail in Sec. 3.3.2

$$p^{\mathrm{Ti}^{16c}} = \int_{-\infty}^{\infty} p(\Delta E^{\mathrm{Ti}^{16c}}) \exp(-\Delta E^{\mathrm{Ti}^{16c}}/k_B T)\, d\Delta E \tag{4.1}$$

where k_B is the Boltzmann constant. A volume based probability can then be obtained by multiplying with the number of possible realizations m per simulation cell and dividing by the average volume V

$$p^{\mathrm{Ti}^{16c}/V} = p^{\mathrm{Ti}^{16c}} \times m/V_{cell}. \tag{4.2}$$

For each of the 360 Ti ions, four surrounding $16c$ sites allow an exchange with two Li^{8a} ions each, resulting in $m = 360 \times 4 \times 2 = 2880$ possibilities per simulation cell for a single defect. The resulting defect density is estimated as $\approx 6.8 \cdot 10^{-6}$ Å^{-3} for $T_S = 700$ K and $\approx 1.50 \cdot 10^{-5}$ Å^{-3} for $T_S = 1300$ K based on an average the simulation cell volume of ≈ 16400 Å^3. This translates to a probability per Ti ion of $\approx 3.1 \cdot 10^{-4}$ and $\approx 6.6 \cdot 10^{-4}$ respectively, which is about two orders of magnitude below the sensitivity of X-ray diffraction measurements [154, 159].

4.5 Li ion mobility

To rationalize Li ion mobility of $Li_4Ti_5O_{12}$ as a function of the occupational disorder, the ion diffusion is systematically investigated using MD simulations following the procedure described in Sec. 4.2.2. Since the computational cost of the MD simulations are comparably high, only few configurations in the relevant energy range can be evaluated. Thus, four representative candidate structures as indicated in Fig. 4.6 are chosen to evaluate the Li ion dynamics. Of these, two structures (“C1” and 2) correspond to regular LTO occupations and two (a and b) include a Ti^{16c} antisite defect. To evaluate mechanistic trends, various temperatures (300 K, 400 K, 500 K, and 600 K) are included. All MD simulations are performed strictly maintaining the stoichiometry $Li_4Ti_5O_{12}$. Hence, no lithiation effects are directly investigated. Although this would be of potential interest, the necessary electron transport effectively occurring as polaron hopping between Ti ions [151] cannot be modeled adequately using the here applied force field (see Sec. 2.2).

4.5.1 Li ion mobility at 300 K

To distinguish the mobility of Li ions in the simulated trajectories the discretization procedure (see 3.3.1 and 4.2.2) is employed. This allows for the evaluation of the total number of hops between different sites during the entire MD trajectory. A focus is set on the maximum displacement d that each individual Li ion reaches from its original position throughout the simulation. This can be compared to the minimal distance between two interstitial sites of $d_{\mathrm{Td-Oh}} \sim 1.8$ Å, found between a neighboring tetrahedral and octahedral site. Ions are observed to either remain in their original site, or only move to a neighboring site ($d_{\mathrm{Td-Oh}} \leq d < 2d_{\mathrm{Td-Oh}}$), or perform a multiple site migration ($d \geq 2d_{\mathrm{Td-Oh}}$). While the latter corresponds to a true diffusive pathway, for instance via the sites $8a \leftrightarrow 16c \leftrightarrow 8a$, the small displacements $d_{\mathrm{Td-Oh}} \leq d < 2d_{\mathrm{Td-Oh}}$ instead predominantly arise from jumps into intermediate interstitials (mostly $8a \longrightarrow 16c$). From these, the ions returns on a picosecond time scale thus presenting a metastable state as also found in other theoretical studies [9, 11, 12, 160].

At room temperature, the MD data reveals a clear correlation between true Li ion mobility and the Ti^{16c} defects. Thereby, no Li diffusion is observed on the nanosecond timescale if no such defect is present. This can be also recognized in the respective MSDs (see Fig. 4.12). As exemplarily shown by means of configurations "C1" and 2 in Fig. 4.6 and confirmed before in more such configurations [1], this immobility extends to representatives at both low and high energies of the thermal ensembles. Hence, irrespective of the wide range of local disorder of the regular configuration, Li ions are virtually immobile. This is consistent with the well-known low ionic conductivity of stoichiometric LTO [133, 160] and confirms recent ensemble-probing NMR results [129, 130]. In contrast to this, the configurations denoted as a and b in Fig. 4.6 that contain one Ti^{16c} defect show a small fraction of mobile Li ions. These, remain in a finite region of about 9 Å around the defect, implying localized diffusion (see Fig. 4.10). Here, a portion of ions only perform frequent back-and-forth hops to metastable intermediate sites ($d_{\mathrm{Td-Oh}} \leq d < 2d_{\mathrm{Td-Oh}}$) while others perform multiple-site migration $d \geq 2d_{\mathrm{Td-Oh}}$. In detail, the short-lived vacancies created by the former allow for a true motion by the latter. This process occurs in a concerted way as illustrated in Fig. 4.9 and may include up to three Li ions, thus resembling an interstitialcy mechanism which is characteristic for fast ion conductors [16]. Investigating the observed processes via NEB calculations (see Sec. 4.2.2) reveals diffusion barriers in the range of 0.1-0.3 eV (compare Fig. 4.11). These low energies rationalize their abundant occurrence on the here investigated nanosecond timescales. Inserting the same mechanism into the regular LTO occupation pattern however yields diffusion barriers in excess of 0.8 eV underscoring the missing mobility in configurations "C1" and 2 due to the absence of defects [1].

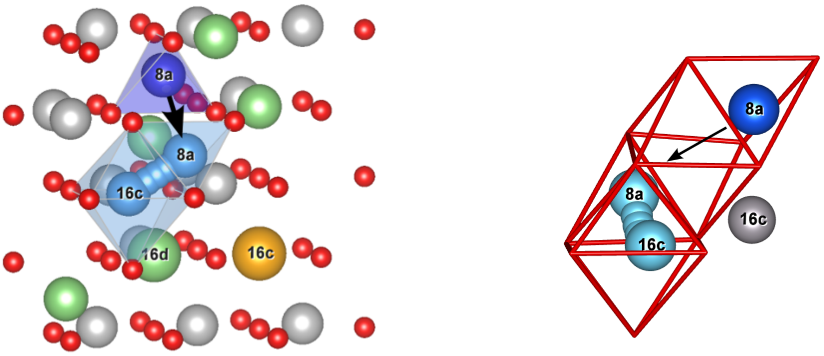

Fig. 4.9: (left) Schematic illustration of the concerted interstitialcy diffusion process as occurring in the vicinity of the Ti^{16c} defect (gold). A frequent back-and-forth hop of one Li ion to the metastable $16c$ site (light blue spheres) creates a short-lived $8a$ vacancy. This consequenty enables the multiple-site migragion of a second Li ion (dark blue sphere). Oxygen ions are shown in red, Ti ions in gray, and Li ions in green. (right) The same process depicted in the oxygen lattice (red) to indicate the coordination sites more clearly. Reproduced with permission from Ref. [1]. © 2017 American Chemical Society.

The picture emerging from these observations shows stoichiometric, nominally homogeneous LTO as a mesoscopic material composed of disordered but predominantly rigid local configurations with little Li ion mobility. This is interspersed with a lower bound of 300 ppm of Ti^{16c} defects per Ti atom (see above Sec. 4.4.1), which generate regions showing localized, correlated diffusion extending fairly far into the bulk [1].

4.5.2 *Diffusion at elevated temperatures*

The insights found at 300 K form the basis from which further understanding is gained about diffusion in the regular LTO-spinel configurations and localized around Ti^{16c} antisite defects. For this, the diffusion at the elevated temperatures 400, 500, and 600 K in the four representative configurations is additionally investigated. On this temperature range the diffusion mechanism can be evaluated in more detail.

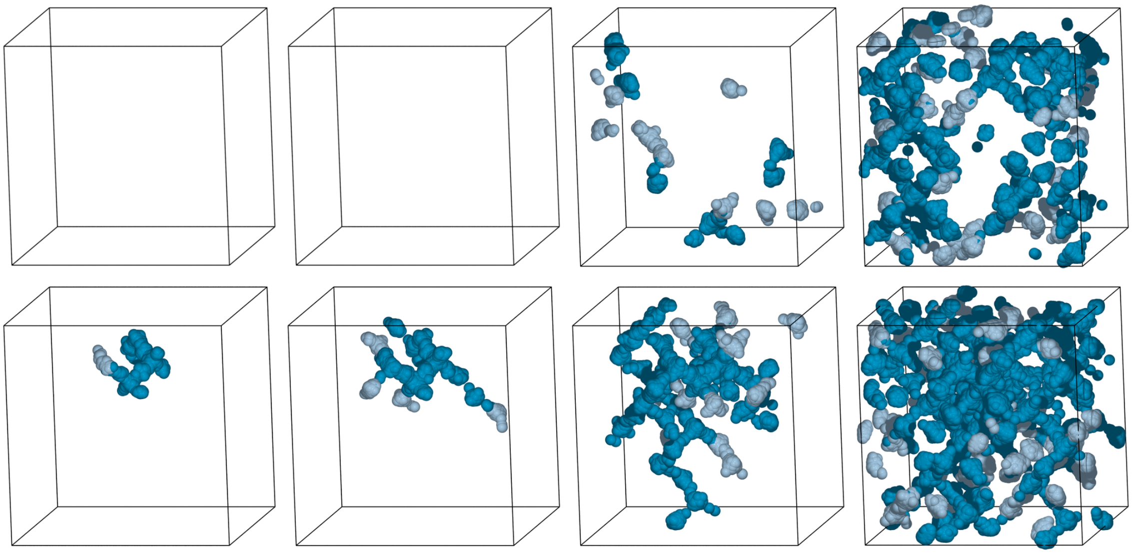

Fig. 4.10: Superimposed positions of all mobile Li ions showing evasive hops ($d_{\mathrm{Td-Oh}} \leq d < 2d_{\mathrm{Td-Oh}}$) in lightblue and multiple site migration ($d \geq 2d_{\mathrm{Td-Oh}}$) in dark blue for exemplary trajectories of configuration 2 (top) and b (bottom) at 300-600 K (from left to right).

As shown in Fig. 4.10, at 300-400 K interstitial diffusion remains locally restricted around Ti^{16c} antisite defects and is therefore only seen in the configurations a and b. With the temperature increase from 300 to 400 K the spatial extend of the localized diffusion regions defined by the maximal distance between mobile Li ions grows from 9 to 16 Å. This increase comes as a consequence of more Li ions involved in the correlated motion and individual Li ions migrating farther. Associated higher migration barriers for the correlated diffusion events are thereby observed (see Fig. 4.11). These are in the order of 0.45-0.55 eV and overcome at 400 K by Li ions originally confined aside the mobile regions at 300 K. Hereby, they either create longer diffusion channels by evading into intermediate sites ($d_{\mathrm{Td-Oh}} \leq d < 2d_{\mathrm{Td-Oh}}$) or by directly participating in multiple site migration ($d \geq 2d_{\mathrm{Td-Oh}}$). At the temperatures 500-600 K interstitial diffusion is also observed in regular LTO-spinel occupation patterns. This can be linked to spontaneously initiating evasive high energy barrier hops which enable subsequent Li ion motion similar to the correlated motion found around Ti^{16c} defects. The initial short-lived vacancies occur randomly in favorable motifs in the lattice and are connected to high energy barriers of at least 0.7-1.0 eV as evaluated from NEB calculations (see Fig. 4.11). Since the spontaneously occurring mobility regions are no longer bound to a defect, multiple such regions may appear in a simulation cell. These grow together to finally expand over the whole simulation cell at 600 K indicating long-range diffusion and a global Li ion mobility already at the here probed nanosecond times scale. Note that the initiating hops lead to rare interstitial diffusion by secondary ions only at 600 K in configuration "C1". A low mobility is thereby due to a higher rigidity of the LTO lattice based on its ordered occupation. At a temperature ≥ 500 K the high temperature diffusion also dominates in configurations including a Ti^{16c} defect masking any additional high temperature influence of the defect.

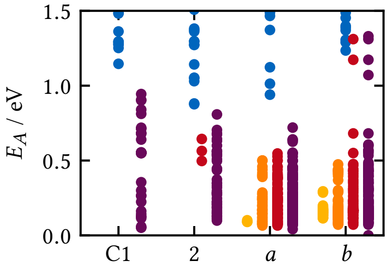

Fig. 4.11: Activation energies (E_A) from NEB calculations for correlated diffusion processes as sampled during MD trajectories (yellow, orange, red and purple for 300, 400, 500 and 600 K) and as tested in the regular LTO occupation pattern (blue) for configurations C1, 2, a, and b.

Generalizing the ion motion in detail, the observed diffusion shows Li ions to be affected by an initial void either triggered by a Ti^{16c} defect or a high energy evasive hop. Li ions show a highly correlated motion able to transport short-lived vacancies to a considerable distance. While the main diffusion patterns involve a $8a \leftrightarrow 16c \leftrightarrow 8a$ motion, a small fraction of Li ions on 16d sites close to the initial dislocation are also mobile. Interstingly, the latter have been predicted by first principles to migrate with associated barriers of 0.8 eV [11] which fits to the onset barriers found here in the high temperature case. Furthermore, for high temperature diffusion experimental studies described a dislocation of $8a$ Li ions to $16c$ sites corresponding to a disordered state [142, 143] which was further predicted as a phase change to a defective rock-salt phase at high temperatures [141]. Although we can observe high fluctuation between $8a$ and $16c$ sites, we cannot state either phenomenon to be clearly distinguishable due to a generally chaotic motion.

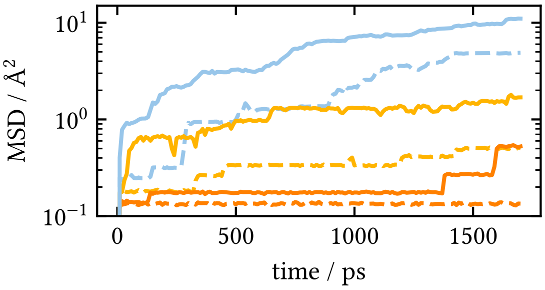

Fig. 4.12: MSD against time for single trajectories of configuration 2 (dashed lines) and a (solid lines) at 400, 500, and 600 K (orange, yellow, and blue). Note the logarithmic depiction on the y-axis as an aid for visualization.

When bridging atomic motion to macroscopic diffusion measurable in experiment, the MSD of the diffusing species is often used to evaluate a diffusion coefficient. Following the Einstein-Smoluchowski relation, normal diffusion is thereby a prerequisite. This means that the MSD needs to increase linearly with time, i.e. the anomalous diffusion exponent α needs to be equal to one in the relation MSD $\propto t^{\alpha}$ [16, 29, 93] (see Sec. 3.3.1). As shown exemplarily in Figure 4.12, the

MSD in our trajectories exhibits a non-constant proportionality to time with temperature. At 300 and 400 K a near identical MSD behavior is seen (therefore only 400 K is shown) where either no Li displacement takes place or single ion hopping events can be distinguished in the case of a configuration showing localized diffusion around a Ti^{16c} defect. When localized diffusion occurs, the MSD reaches a maximum which is defined by the spatial extent of the high Li mobility region around a defect. The associated values for α are all well below 0.1 (c.f. Table 4.1) which is directly proportional to the finite migration length in the high mobility region over the simulation time. The high temperature diffusion based on correlated motion following spontaneous void creating hops (see above) is quantitatively visible in the strong increase of the MSD. While at 500 K this mobility does not suffice for an overall three dimensional migration with α of only 0.1-0.4, the diffusion becomes truly global at 600 K with values of 0.4-0.8 (compare Tab. 4.1). The high variance of α derives hereby from the fractional dimensionality defining the percolation networks of the respective LTO configurations. A residual deviation of the global mobility at 600 K from normal diffusion is based on the highly correlated mechanism and the multitude of microscopic hopping barriers [93] where the latter is a consequence of the configuration space of LTO as also confirmed on the DFT level [11, 12, 135]. The observed transition to a global Li ion mobility upon the high temperature mechanism change compares well to an experimentally observed surge in Li ion conductivity at temperatures above 600 K [141–143].

Tab. 4.1: Averaged anomalous diffusion exponents α obtained from the time dependence of the MSD (MSD $\propto t^{\alpha}$) of the configurations C1,2,a and b for the investigated temperature range 300-600 K.

	300 K	400 K	500 K	600 K
C1	-	-	0.050	0.408
2	-	-	0.106	0.549
a	0.077	0.212	0.391	0.649
b	0.189	0.198	0.424	0.702

Since the observed values for α do not yet show normal diffusion, an evaluation of diffusion coefficients comparable with experiment is improper. Nevertheless, the ensemble averaging MSD gives an insight into the macroscopic behavior. As seen in this example, diffusion influencing effects entangled in the MSD reflect the collective motion expected at experimental time and length scales indicating for instance the mechanism change.

4.5.3 Cascade-like diffusion upon Li insertion

The here presented simulations at the temperatures 300-400 K show only localized diffusion which, as a sole mechanism, would predict no macroscopic Li ion conductivity. Since the latter is however observable in LTO at room temperature [133, 160], it is evident that this picture is not complete. Absent at the probed time scales are rarely occurring vacancy diffusion events, which present the standard diffusion model for global Li transport in Li ion battery materials [2, 9, 11, 12]. In fact, in order to witness such a vacancy diffusion event at room temperature, a simulation time longer by 2-4 orders of magnitude would be needed for the here employed system size, where the latter is estmated from the range of experimentally determined diffusion coefficients [161]. Thus, a time scale separation of the mechanisms is noted, where ultra fast localized diffusion around Ti^{16c} defects at nanosecond time scales opposes slow vacancy diffusion at microsecond time scales. This picture fits to a recent combined ^{7}Li SAE NMR and first principles study [162] where alongside different time scales of slow Li ion exchange processes, ion mobility below the experimental accessible microsecond time scale could be identified.

It can be expected, that slow and fast mechanisms cooperatively transport Li ions in LTO in a cascade-like arrangement [1]. Considering a slowly migrating Li$^+$ vacancy in the bulk approaching a region of high Li ion mobility, a quasi-instantaneously transport along the segment length of the latter can be expected. However, the low Li ion conductivity in stoichiometric $Li_4Ti_5O_{12}$ indicates that this will only take place as isolated events. This is due to a global lack of Li$^+$ vacancies which can likely be considered dilute in the pristine material and therefore present a mobility bottleneck. This situation changes upon lithiation where domains of rocksalt structured $Li_7Ti_5O_{12}$ are formed within the spinel configuration [132, 133]. In the lithiated phase Li ions previously located on the tetrahedral 8*a* sites occupy octahedral 16*c* sites which leads to an occupational mismatch on the phase boundary. Here, interphase bound, fluctuating Li vacancies are created [135]. Already at low lithiation levels of $x = 0.1$ in $Li_{4+x}Ti_5O_{12}$ a surge in Li ion conductivity is experimentally observed [129, 130] which hints that these interphase vacancies become globally mobile. This global mobility can be linked to a cascade-like diffusion where high mobility regions transport such vacancies away from the interphase and extend these - then more abundant - vacancies to a connected diffusion network.

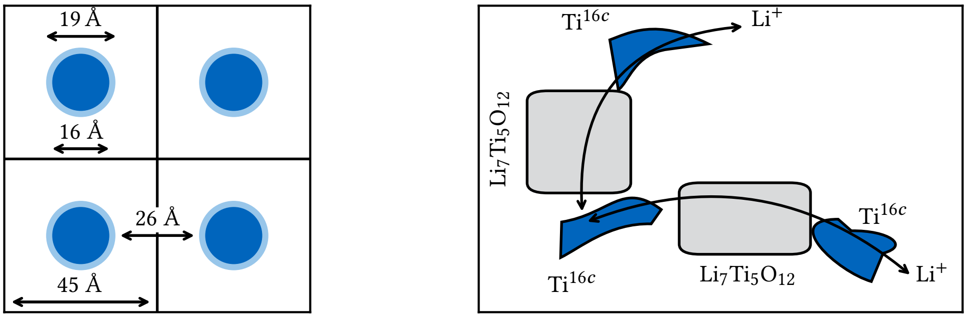

Fig. 4.13: (left) Estimated topology of the high mobility regions (blue) in $Li_4Ti_5O_{12}$ following a primitive packing. The interaction sphere of the high mobility region is shown in light blue and descriptive distances are indicated by arrows as described in the main text. (right) Schematic depiction of the connection of high mobility regions (blue) and $Li_7Ti_5O_{12}$ domains (gray) via global diffusion pathways.

To strengthen this claim, the topology of high mobility regions in $Li_4Ti_5O_{12}$ is quantified based on the simulations performed in this work. These regions depend directly on the concentration of Ti^{16c} antisite defects which seed ultra fast Li ion mobility. From the reciprocal mean defect concentration derived in Sec. 4.4.2 of $\approx 1.09 \cdot 10^{-5}$ Å^{-3}, it is estimated that a volume of $\approx 9.1 \cdot 10^4$ Å^3 is needed to incorporate one defect. Assuming a primitive packing, a cubic volume is considered separating defects with a shortest distance equivalent to the side length of 45 Å (see Figure 4.13). The spatial extent of the high mobility regions around the defects is then estimated from the space filled by mobile Li ions during the MD simulations (compare above in Sec. 4.5.2). The estimates are thereby taken from the simulations at 400 K. Here, they serve as an approximation to longer simulation times since the finite simulation time results in an inherent underestimation of the Li diffusion at 300 K. Still localized, the long-range diffusion is not connected to a mechanism change and can therefore be viewed as an accelerated 300 K simulation. Encountered additional hopping barriers found at the higher temperature are only larger by 0.1-0.2 eV which would translate to rarely occurring high energy diffusion events observable at longer time scales. The space filled by mobile Li ions is estimated by a spherical volume where a diameter is approximated by the maximum distance of mobile Li ions in a the high mobility region averaged over all trajectories. A radius of 8 Å follows to which another 1.8 Å is added which corresponds to the distance of neighboring interstitial sites necessary for a vacancy to connect with the high mobility region. As depicted in Figure 4.13, this estimate yields distances between high mobility regions around a mean of ≈ 26 Å which is equivalent to seven vacancy hops and thus renders the average mobility region isolated in the uncharged state. However when intercalating Li, high mobility regions could funnel a local Li ion gradient to accumulate adjacent moieties of $Li_7Ti_5O_{12}$ (as discussed above) which would grow until they connect to the next proximate region of high mobility. With this process repeating, close lying regions of high mobility would be connected by $Li_7Ti_5O_{12}$ moieties to form a global diffusion pathway (see Figure 4.13). Considering shorter, below-average distances between such regions, a global diffusion network could already appear at low concentrations of intercalated Li ions which would boost Li ion mobility and explain the mentioned experimental findings [129, 130]. Additionally, this proposed mechanism elucidates the origin of global percolation channels observed via conductive atomic force microscopy experiments during lithiation of LTO [137] which are linked to a $Li_7Ti_5O_{12}$ phase mediating Li ions through the bulk [136].

4.6 Conclusion and Summary

In summary, the degree of disorder and its effect on Li ion diffusion for $Li_4Ti_5O_{12}$ is investigated. Using Monte-Carlo sampling techniques we assess realistic mesoscopic representations of the configurational space which yield a high degree of disorder stabilizing a manifold of atomistic motifs. Hereby, even more disruptive Ti^{16c} antisite defects - not following the regular spinel-like arrangement - become possible and are predicted to occur with considerable concentrations. The Li diffusion is explored at various temperatures using MD simulations, which intrinsically incorporates and thus reveals all relevant ion motion.

From this it is found that vacancies appear around Ti^{16c} antisite defects and additionally at high temperatures in the regular spinel which act as a seed for confined ultra-fast correlated motion following an interstitialcy mechanism. Although the correlated migration processes are comparable at low and high temperatures, their implication is substantially different. On the one hand, fast mobility is isolated around the defect-sites at 300-400 K and therefore does not contribute to global diffusion. This renders classic vacancy diffusion as the mechanism for long range Li transport. On the other hand, multiple spontaneously occurring vacancies at temperatures $\geq$ 500 K trigger localized mobility which interconnects and even forms a global diffusion network at 600 K. This fits to the experimental observation that $Li_4Ti_5O_{12}$ transits from a bad ion conductor [160] to a good ion conductor at 600 K [143] and demonstrates the fundamental difference of diffusion at low and high temperatures due to the collective and concerted motion.

Considering the atomistic origin of the high rate capability of LTO based on a Li ion mediating $Li_7Ti_5O_{12}$ phase [136, 137], a cascade-like mechanism is proposed. The latter is characterized by fast localized diffusion around the defect sites and interphase exchange in a cooperative manner [132, 135]. With estimating distances between regions of high mobility, this mechanism is found viable to form a global diffusion network even at low concentrations of intercalated Li. This concludes a showcase of the possible impact of collective motion on the nanoscale to the mesoscale. Naturally, further investigation of this cooperative diffusion is necessary to directly elucidate the proposed mechanism. For this, lithiated stoichiometries need to be simulated explicitly, which requires a charge transfer force field to take into account mixed valence states of Ti i.e. Ti^{3+} and Ti^{4+} respectively.

In conclusion, the impact of occupational disorder is elucidated to enable collective ion motion. In the here investigated LTO, this is dominating in its net effect over single ion processes and therefore changes the picture of ion diffusion from the common description. On a more general note, Li ion diffusion in many battery materials might be subject to similar collective processes rather than solely to a single ion diffusion mechanism. This has already been confirmed for some fast ion conductors used for solid state electrolytes like LGPS [111]. Equally, this could extend to other intercalating materials of which many exhibit substantial occupational or configurational disorder, giving the necessary structural flexibility.

From a methodological perspective, this study presents a novel approach towards thoroughly investigating occupational disordered crystalline materials. Here, configurational entropy, and chaotic ionic motion are taken into account by combining different methods. Firstly, the Wang-Landau sampling mostly applied to model-problems, is technically adjusted to be employed for experimentally relevant problems as presented in Sec. 4.2.1 and generalized in 3.2.2. Secondly, the novel combination of MD simulations, their discretization, and NEB calculations allows to elucidate the diffusion mechanism without any chemical intuition. In both cases, a high degree of automatization is necessary for these tasks as the millions of involved configurations and microscopic processes cannot be analyzed by hand.

The presented methodology thus overcomes the limitations of the more common strategy where one simply investigates elementary single ion processes for an assumed “standard” diffusion mechanism [2, 9, 16]. In that, the usually picked high symmetry, low energy configurations show an explicit rigidity as seen in the above presented configuration “C1” for LTO. If occupational disorder is possible, these may not present the most stable configurations and may not depict the most likely diffusion behavior.

5 Li ion mobility in glass-amorphous Li_3OCl

In this chapter, a study on glass-amorphous Li_3OCl and its properties as a solid state electrolyte is presented. As any glass, this material has no periodic structure and is therefore subject to a considerable disorder. It differs from conventional ion conducting glasses since Li is not a guest ion in an amorphous host but constitutes the sole network forming cation. Thus, Li is both structure-giving and the mobile species which may lead to an unusual structure-mobility interplay. From this, an ion diffusion behavior can be expected which deviates from diffusion models for ion conducting glasses [104, 163, 164]. Considering the microscopic structure of a glass, a multitude of local configurations can be expected which in this case are subject to profound dynamic changes. The latter pose a considerable challenge for computer simulations since a systematic screening of structures like the random network model for amorphous materials [165] is not applicable. This renders a consistent sampling of the configurational entropy via a Monte-Carlo like procedure impractical. It follows, that a computational approach is required in which rigorous temperature dependent statistics are generated in order to capture the dynamic non-equilibrium state and its effects in this glass.

5.1 Introduction

Glass-amorphous Li_3OCl was first reported by Braga *et al.* as one of the fastest Li conducting solid state electrolytes at 300 K [166]. Depending on ambivalent doping, ionic conductivities of 2-30 mS/cm at lightly elevated temperature are reported which are on the order of non-aqueous liquid electrolytes with a conductivity of 1-10 mS/cm [167–170]. This exceptional performance makes this a superior solid electrolyte, outperforming even the best crystalline electrolyte $Li_{10}GeP_2S_{12}$ with a conductivity of 12 mS/cm [171]. On the basis of this electrolyte, a novel Li ion battery is proposed which theoretically provides unmatched capacity and lifetime [172]. This battery consists of the glass electrolyte, a Li metal anode contacting a stainless steel current collector/container and a cathode which is based on an understoichiometric sulfur or MnO_2 to glass electrolyte mix contacting a copper current collector. Interestingly, the potential in the battery is kept at a high level which supposedly prevents the formation of Li_2S compounds. Thus, the cathode is not formally Li intercalating, but sulfur is proposed to act as a redox center which undergoes intermediate redox reactions mediating Li ions to form Li metal at the cathode current collector. Here, the only driving force allowing the formation of a potential is the workfunction difference between both current collectors. This claim is based on the chemical stability of the used electrolyte against the current collector. Naturally, this concept has caught much attention and criticism. It is argued that the absence of redox reactions with an intercalation host cannot provide a thermodynamic potential. Thus plating Li metal on either electrode when charging and discharging cannot create energy [173]. Despite the skepticism for this new battery type, the involved glass-amorphous electrolyte itself promises outstanding performance also in conventional solid state batteries. Besides the high ionic conductivity, the material demonstrates mechanical malleability and is even capable to be synthezised as Na_3OCl for the use in sodium ion batteries [166, 172, 174, 175].

The exceptional properties of glass-amorphous Li_3OCl are argued to be founded in its special synthesis procedure [166, 172, 174]. Here, either wet Li_3OCl or $Li_3OCl_{1-x}(OH)_x$ ($Na_3OCl_{1-x}(OH)_x$) [174] is placed into a reactor and heated to 503-523 K. It is then cooled under air to let HCl and H_2O evaporate. Hydroxide ions are supposedly mostly removed that way and minor remains are claimed to be bound in alkali (Li or Na) polyanions. When cool, the intermediate product is ground to a powder either in an inert atmosphere or ethanol. The powder is then placed in an epoxy sealed cell and cycled at elevated temperatures to form the glass and evaporate ethanol or other remainders through the epoxy sealing. Crystalline side products are ruled out by XRD or differential scanning calorimetry measurements, hence only an amorphous phase persists. Shown via cyclic voltammetry, this phase remains stable against electrochemical reactions under operational conditions. Ambivalent dopants of Mg, Ca or Ba are optionally added via their hydroxides at understoichiometric amounts to lower the glass transition temperature. Ba doped glass exhibits the highest conductivity, however, a general lack of characterization as summarized in Tab. 5.1 leaves unclarity about this material. Furthermore, the original authors argue that the synthesis under constant electrochemical cycling leads to an alignment of the interior dipoles. Loosely based on DFT reference calculations, OLi^- dipoles form which facilitate ion migration enhancing the mobility in the excess volume of the glass [174, 175].

Tab. 5.1: Selected material properties of the pure Li_3OCl and doped $Li_{3-2x}M_x^{(II)}OCl$ (x=0.005, M=Mg, Ca, Ba) stoichiometries as taken from different publications ([166]^1 ,[176]^2, [177]^3, [174]^4). Shown are the melting and glass transitions temperatures T_m and T_g, the densities of crystalline and glass phase as available, as well as the listed conductivities for given temperatures. *The listed glass density is for a partially amorphous sample.

	T_m / K	T_g / K^1	$\rho_{crystal}$ / g cm^{-3}	ρ_{glass} / g cm^{-3}	λ_{AC} / 10^{-3} S cm^{-1}
Li_3OCl	555^2	392	2.02^3	1.96^{*1}	2.1 (335 K)^1
$Li_{3-2x}Mg_xOCl$	542^1	382 (409)			2.1 (332 K)^1
$Li_{3-2x}Ca_xOCl$		372	2.09^1		1.3 (314 K)^1
$Li_{3-2x}Ba_xOCl$		438	2.28^1		$\approx$ 33.5 (335 K)^{1,4}

Clearly, the current state of research leaves several open questions about the glass-amorphous electrolyte. Significant differences between AC and DC conductivity (stated with a factor 5 [174]) and an extremely low temperature dependence of the mobility giving an apparent migration barrier of < 0.1 eV are puzzling. Questionable is also the role of remaining OH^-, or H^+ ions. These for instance have been shown to be one of the hidden critical performance enhancers in the corresponding crystalline Li_3OCl solid state electrolyte [178]. Additionally, the stability against Li_2O and LiCl formation under operational conditions — an effect also found in the corresponding crystalline phase based on kinetic effects [179, 180] — is not yet understood. In this thesis, the Li ion mobility in the pure amorphous material is investigated to obtain an insight in absence of any possible impurities. Using atomistic simulations, a microscopic understanding of the respective ion diffusion shall be gained. Hereby, a force field potential is employed to reach the appropriate time and length scales encountered in a glass. The latter is parameterized against *ab initio* reference data in order to retain a high accuracy. Glass structure ensembles are then created using a melt-quench procedure and rigorously probed via MD simulations at different temperatures. The resulting statistics show that the experimentally reported high Li ion mobility together with a low apparent migration barrier are factual. This excludes argued side effects of impurities as the source for the observed high ion conductivity. Furthermore, the microscopic analysis shows that unexpected Cl mobility is also present which may explain the differences in AC and DC conductivity. From this follows additionally, that the applicability of this solid state electrolyte is compromised. Here, current limiting polarization concentration effects from the simultaneous conduction of cation and anions can be expected.

5.2 Computational details

DFT calculations for all reference structures of the training set are performed with the Vienna Ab Initio Simulation Package (VASP) [181, 182] using the projector-augmented wave (PAW) method [183] and a plane wave basis set in periodic boundary conditions. The PBEsol [184, 185] functional is employed and plane wave cutoff energies of ≥ 500 eV are used for all calculations. The Brillouin zone is sampled with a Γ-point centered 4×4×4 Monkhorst-Pack grid [145]. Smearing of the Fermi surface is enforced with a Gaussian width of 0.05 eV and the electronic structure is converged until a total energy difference of 10^{-6} eV. To obtain minimum energy structures, geometries are relaxed until residual forces are less than 0.001 eV/Å. To sample reference structures for the training set for the melt and glass, *ab initio* molecular dyamics (AIMD) calculations are conducted. Here, the same settings as above are used with the exception of a Brillouin zone sampling only at the Γ-point to obtain a better computational performance. Convergence of energy, forces and stress is thereby ensured and overall dynamic properties found in the trajectories do not show any noticeable differences. For simulations in the NVT ensemble a Nosé thermostat [186–188] and for NPT calculations a Langevin thermostat and barostat [28] are used.

All force field simulations are conducted using the code package LAMMPS [58] developed at Sandia National Labs. The force field terms applied in this study are based on the Born model of ionic solids, where a Coulomb term is combined with van der Waals interactions and short range repulsion as described by the Buckingham potential (see Sec. 2.2.1). Additionally, polarization is included via the core/shell model (see Sec. 2.2.2). The force field parameterization and all subsequent calculations are performed within a cutoff of 12 Å for the short-range interactions and treating Coulombic long-range interactions with a particle-particle particle-mesh solver[146]. In all simulations periodic boundary conditions are applied. MD simulations are performed using a time integration via the Verlet algorithm [148] with a timestep of 0.2 fs. The core/shell particle motion is integrated following the adiabatic core/shell model by Mitchell and Fincham [53] where shell particles are given 2 % of the ion mass (see Sec. 2.3.3). A resulting relative core/shell motion did in no case show thermalization rates higher than $8.0 \cdot 10^{-5}$ K ps^{-1} up to a temperature of 1200 K (melt simulations) which is well below the average literature value of 1.0 K ps^{-1} by Mitchell and Fincham [53]. For the NVT ensemble a Nose-Hoover chain thermostat and in NPT simulations an additional Hoover chain barostat is applied [148, 149]. Each MD simulation is equilibrated for 50 ps before data sampling.

Global and local optimization algorithms are adopted from the PYTHON packages INSPYRED [69] and SCIPY [71], respectively (see Sec. 3.1.2). These are embedded in a PYTHON framework based on the atomic-simulation-environment (ASE) [66] which is interfaced to LAMMPS via its PYTHON bindings.

Images of crystal structures and atomic depictions are created with VESTA [147].

5.3 Force Field Potential for glass-amorphous Li_3OCl

To model structure and transport in an amorphous material via atomistic simulations, force field potentials present a suitable approach. This is due to the reason that the properties of interest do not require explicit electronic structure treatment and that the moderate computational cost of force fields allows to simulate at the necessary length and time scales. For Li_3OCl such a potential has only been parameterized for the crystalline phase by Mouta *et al.* [76]. As shown below, this potential is not accurate for the description of the amorphous phase. Therefore, a new potential is parameterized as described in the following.

5.3.1 Parametrization Strategy

To illustrate the interactions between the ions in the glass a pair potential in combination with the core/shell model is chosen as described in Sec. 2.2. This is consistent with the existing force field of the Li_3OCl crystal [76]. The potential presents a versatile choice as it can describe highly ordered [39] as well as disordered phases [65]. Specifically, it has been successfully applied to many ionic crystals and oxides [24, 39, 52] (see Sec. 2.2) as well as to silica glasses [189–193]. The alternative use of manybody potentials in order to grasp strong covalent interactions, which is for example needed in transition metal compounds, is deemed negligible [34, 194]. This follows from the assumption that Li_3OCl keeps a strong ionic character independent of coordination environment or phase. Small deviations from this rule are compensated by adding polarizability via the core/shell model. The parameterization of the potential parameters is based on *ab initio* data, as presented in the following.

Estimation of the density of amorphous Li_3OCl

To set up realistic DFT reference models for the amorphous phase, knowledge of the equilibrium density or at least its approximate range is needed. In contrast to the well-defined Li_3OCl crystal (see Tab. 5.1), experimental values for glass-amorphous Li_3OCl are not available with satisfactory accuracy. Therefore, the density is estimated from an NPT AIMD equilibration for the glass at 300-400 K and for the melt at 700-900 K. The AIMD simulations are conducted for $\approx$ 120 ps, which prove adequate for a sufficient convergence. For the glass, different randomized-annealed configurations are used as initial structures in order to account for its non-ergodic behavior [119–121]. These are created via melt-quench procedures (see Sec. 5.4) on basis of the potential by Mouta *et al.* [76]. The different configurations give an approximate distribution of volumes from which an estimate for the glass density of 1.79 ± 0.02 and 1.76 ± 0.01 g/cm^{-3} at 300 and 400 K is determined. Note that these values are considerably lower than the experimentally suggested density of 1.96 g/cm^{-3} which was determined for a partially crystalline sample [166]. The latter translates to a volume expansion in comparison to the crystalline phase of only 6 % compared to 13 ± 1 and 15 ± 1 % as determined from the AIMD simulations. Taking silica as a reference where the amorphous to the crystalline phase shows an expansion of 20 % [195], the *ab initio* data appears more convincing. In contrast to the glass, the melt behaves ergodic. Thus the density can be determined more accurately from a single simulation and is found at 1.69 ± 0.03 and 1.61 ± 0.03 g/cm^{-3} for 700 and 900 K, which translates to 19 ± 2 and 26 ± 3 % volume expansion. Since the volume expansion is a more intuitive value than the density, the dimensionless ratio $V/V_{crystal}$ will be used in the following. This is referenced to the experimental lattice parameter 3.907 Å of the crystal at 300 K after [177]. This value is chosen as it lies between the DFT lattice parameters available at 300 K which are stated at 3.90 Å [179] and 3.912 Å [166].

Pair potential parameters

An energy, force and stress matching procedure as described in Sec. 3.1.1 is used to obtain the parameters for the pair potential. To enforce a high generality of the potential and prevent overfitting, a training set is chosen which contains different reference structures spanning the phase space of Li_3OCl. Thereby 16 % of crystal structures and 84 % of amorphous structures are included to cover a broad spectrum of ionic distances which are likely to result in accurate short and long range interactions [38]. To exclude artificial energy inconsistencies due to size effects (in the Brillouin zone sampling of the plane wave basis set), all structures are of comparable size. They are thereby chosen sufficiently large with 135 atoms to adequately describe disorder (an only exception are defect structures with 133 atoms). During the fitting process the training set is consistently extended to correct for unphysical configurations which appear in incorrect intermediate potentials, a procudure as also suggested in literature [65].

Crystal references are based on a 3 × 3 × 3 supercell of Li_3OCl and include two sets of structures. A first set is composed of 40 structures created with random displacements of atoms around their equilibrium positions (maximum of 1.5 Å) of which some are also compressed or expanded by 2% of the lattice constant. A second set of 24 structures is taken from NEB calculations of the vacancy diffusion barrier. The vacancy is created as a Li-Cl Schottky defect [179]. Of this latter set, 16 structures are added from NEB calculations based on intermediate potentials which show too low barriers.

Amorphous structures are taken from AIMD simulations conducted for 100-200 ps in an NVT ensemble of the glassy and molten phase. These are constrained at different volumes distributed around the densities obtained from the AIMD simulations, as described above. For the glass, simulations are performed at volumes of 1.13, 1.15 and 1.20 V_{crystal} and at 300 and 400 K. At each volume several calculations with different initial configurations are conducted to avoid a strong bias (three for 1.13 and 1.15 and two for 1.20 V_{crystal}). From the AIMD, structures from snapshots are taken every 10 ps yielding 160 structures. Of the latter, a geometry optimization is performed for 15 structures which are also added to the set. From ill-performing potentials, showing an accelerated diffusion in test MD simulations as well as strong Li-Cl overbinding, another 154 structures are added for the volumes 1.13 and 1.15 V_{crystal}. For the melt, 54 structures are taken from AIMD simulations at 900 K at different volumes of 1.20, 1.28 and 1.33 V_{crystal}. The fast dynamics in the liquid phase allows us to select structurally decorrelated snapshots. The decorrelation time is estimated from the time interval in which the MSD exceeds the first coordination sphere as determined from the radial distribution function (RDF).

In parameterizing the potential for the ternary system Li_3OCl, 21 parameters are formally included. This set can be reduced based on physical considerations [39]. Firstly, the partial charges are represented as one parameter due the need to remain charge neutrality in the force field. For the stoichiometric relation then follows: q_{Cl} = -q_{Li} and q_{O} = -2 q_{Li}. Secondly, Li can be assumed to be a relatively hard ion which will not be subject to any van der Waals interactions. This means that the Buckingham parameters $C_{\text{Li-Li}}$, $C_{\text{Li-O}}$ and $C_{\text{Li-Cl}}$ can be fixed to zero [76]. Despite this reduction, the remaining 16 parameters still pose a considerable optimization problem. Scanning all parameter dependencies on a grid within predefined boundaries scales with n^{16} where n represents the number of grid points in each dimension. This already yields $4 \cdot 10^7$ evaluations for a minimal grid of $n = 3$ which is not easily achievable and with a sufficient grid spacing (i.e. $n = 100$) impossible in the foreseeable future. Therefore a heuristic search is necessary including global and local sampling, for which a PSO algorithm is employed (see Sec. 3.1.2). To cover a reasonably large search space efficiently, all PSO optimizations are conducted using a swarm size of 500 particles. This exceeds the minimum number of recommended particles (10 × the number of variables) in order to take into account the corrugated parameter space. Most of the conducted optimizations converge more or less within 200 steps to a minimum, which is evident of an adequate swarm size. A final potential is acquired employing the following strategy:

1. Generation of a large number of good initial guesses via several PSO runs. Each particle in a PSO is initialized via uniformly randomized parameter sets within the maximal boundaries.
2. The parameter space is re-sampled around the initially guessed potentials using a PSO. For this, particles are initialized with parameter sets normally distributed around the initial guess.
3. Best candidates are locally optimized using an L-BFGS optimizer (see Sec. 3.1.2) and validated as described below.
4. When the training set is iteratively extended, the parameterization is restarted from step 2.

Core/shell parameters

The pair potential described above shall reproduce the stoichiometric material at 0 K according to the accuracy of the DFT-PBEsol reference (see Sec. 5.2). To amend this potential with an accurate description for defective structures, the core/shell model is added which is parameterized on top of the final potential (compare Sec. 3.1.3). For this, the energy, force and stress matching procedure is also employed. This is applied to a new training set including Li-Cl Schottky defects and Li, Cl and O Frenkel defects in crystalline structures.

The defects are randomly introduced into a $3 \times 3 \times 3$ supercell of Li_3OCl following a subsequent geometry optimization at DFT level. In total, 11 and 16 structures with Schottky and Frenkel defects are taken into account. Additionally, 8 structures describing a NEB path of a vacancy diffusion process (see above) are appended, respectively. To relate these perturbed structures to the equilibrium crystal, 15 crystal structures with slight atom displacements (as above) are added as well. This specialized training set ought to be sufficient to parameterize the two spring constants k for O and Cl and obtain a reasonable static polarizability. The reduced size of the training set of 50 structures is also advantageous considering the increased computational cost of the core/shell evaluation. Here, every reference structure evaluation requires an optimization of the shell positions. For that, a conjugate gradient optimization as implemented in LAMMPS is employed. The increase in computer time scales directly with the number of optimization steps which, on average, turns out to be eight.

Although the search space for the optimization problem is only defined by two variables (the spring constants k), a local optimization based on the above mentioned L-BFGS optimizer is unreliable. Here, the parameter space involves many local minima which prohibit a gradient based search. Therefore, a global search based on the particle swarm method is applied. Hereby, 200 particles are used to cover the complete parameter space uniformly within 20-800 eV Å^{-1} for each k during the initialization. The shell charges — which present an arbitrary choice — are taken from the previous parameterization for the Li_3OCl crystal [76]. Starting from this, a fit finds a best solution usually within 10 steps whereby the median of particles falls close to that solution already at step 50. Hence, this “global” optimization problem exhibits a minor search effort and fortunately converges very fast to a global minimum.

5.3.2 Fitting success

The parameters of the final potential can be found in the Appendix A. For those, a relatively good fit to the training set is achieved. The agreement in relative energy, forces and stress components to the reference data is shown in Fig. 5.1 and the according mean errors are given in Tab. 5.2. Overall, a comparably good reproduction of the DFT properties is seen in relating the crystalline, glassy and molten phase, showing no evidence of systematic errors in the potential. Seemingly large errors in e.g. the energies are mostly owed to outlying, extreme configurations. The goodness of the fit and prediction becomes apparent when comparing to the potential of Mouta *et al.* [76]. Here, systematic errors can be found in the description of glass and melt structures which appear critical in the overestimation of energies and underestimation of stresses (see Fig. 5.1). Of course it should be noted that this force field potential was not parameterized against the amorphous structures. Nevertheless, even for the crystal, the here obtained force field exhibits superior performance which is mainly attributed to a better description of configurations far away from equilibrium. This observation confirms the disadvantage of an empirical parameterization where only the macroscopic equilibrium can be captured [52].

Tab. 5.2: Residual mean error of relative energy (ΔE in meV), forces (ΔF in meV Å^{-1}) and stress components ($\Delta\sigma$ in meV Å^{-2}) for the training set, phase-divided into crystal, glass and melt structures. Values are given as obtained for the here derived force field potential and as a comparison for the potential by Mouta *et al.* which was parameterized for the crystal Li_3OCl using an empirical approach. Specifically errors for the isolated Buckingham potential as well as for the combination with core/shell model are listed.

this work						
	Buckingham			Buckingham & core/shell		
	ΔE	ΔF	$\Delta\sigma$	ΔE	ΔF	$\Delta\sigma$
crystal	1215	47	0.516	1166	24	0.580
glass	1896	103	0.674	1201	77	0.649
melt	922	142	0.690	1214	101	0.655
Mouta *et al.* [76]						
	Buckingham			Buckingham & core/shell		
	ΔE	ΔF	$\Delta\sigma$	ΔE	ΔF	$\Delta\sigma$
crystal	1335	124	2.720	1218	85	2.683
glass	4336	230	4.122	3011	174	4.051
melt	7876	346	1.306	5082	260	1.146

The parameterized core/shell model yields a corrected description of the defective structures in the training set. The mean error improves for energies by 110 meV, for forces by 18 meV Å^{-1} and for stress components by 0.05 meV Å^{-2}. While the change in energy and stress is rather negligible, the improvement in the forces is quite dramatic. This shows especially for the outliers, i.e. the problematic defects as depicted in Fig. 5.2. A noticeable improvement in most properties with

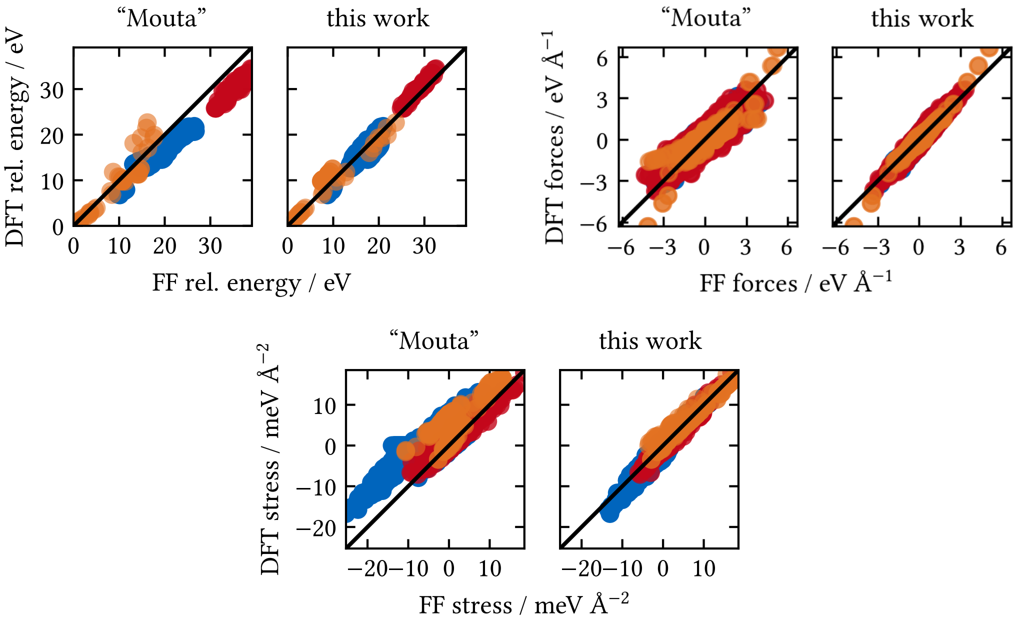

Fig. 5.1: Corellation of energies (top left), forces (top right) and stress components (bottom) from DFT against different force field potentials (FF) for the structures in the training set. In each graph the force field to DFT relation is given on the left for the parameterization of Mouta *et al.* (labeled “Mouta”) and on the right for the here obtained potential (labeled “this work”). Data points corresponding to crystal structures are shown in orange, to glass structures in blue and to melt structures in red.

the additional core/shell model stays consistent for all structures in the larger training set used for the parameterization of the Buckingham potential as shown in Tab. 5.2. The only exception concerns the energies in the melt structures which worsen significantly by 30 % and the stress components in the crystal which worsen by 10 %. In the former a systematic underestimation is thereby introduced. This is due to the the absence of the melt structures in the specialized core/shell training set. This way the core/shell model removes a bias towards the melt from the parameterization. Since the melt is not of special interest in this work, this error is unproblematic. In comparison to that, a corrected description of the short range response to vacancies yielded by the core/shell model is highly anticipated. The latter emerges as seemingly important which shows in the improved forces and energies of the crystal and glass.

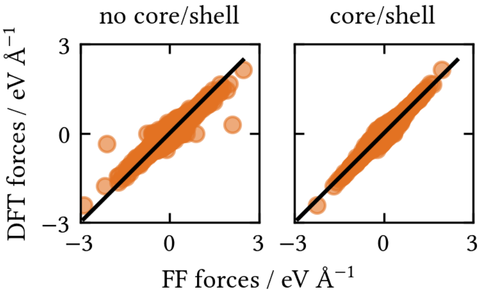

Fig. 5.2: Comparison of force components from DFT against the parameterized pair potential (FF) for the structures in the core/shell training set. (Left) without and (right) with the core/shell model.

Since the core/shell parameters are parameterized following physical motivation (the polarizability), the here obtained parameter set is examined more closely. The resulting force constants k yield polarizabilities for O of 0.69 Å^3 and for Cl of 2.32 Å^3 (following Equ. 2.10). These values reflect the expected physics quite well where Cl is more easily polarizable. Comparing to polarizabilities from experimental or *ab initio* data, the here obtained values are below the literature reference of $\approx$ 1.81 Å^3 and $\approx$ 2.90 Å^3 [75] for O and Cl in a Li environment, respectively. On the one hand, this could be based on the difference in chemical environment as compared to the literature reference values. On the other hand a difference might be due to the partial charges in the parameterized Buckingham potential, which already represent a mean static polarizability [27]. Furthermore, the oscillation frequencies of the core/shell particles based on the obtained force constants are $3{\cdot}10^{14}\,\mathrm{s}^{-1}$ and $1{\cdot}10^{14}\,\mathrm{s}^{-1}$ for O and Cl, respectively. These are well above the fastest vibrations in the melt at 900 K of $5{\cdot}10^{10}\,\mathrm{s}^{-1}$ (oscillation period of 20 ps) as estimated from the Fourier transformation of the velocity autocorrelation function from the corresponding AIMD simulations. Thus, the core/shell particles should be able to represent instantaneous polarization in the adiabatic model (see Sec. 2.3.3).

5.3.3 Validation of the force field potential

Accurately reproduced DFT energies, forces, and stress components are a measure of success for the fitting procedure against the training set. However, these do not indicate the chemical predictive power of a force field potential. Thus, any emerging trial potentials are further validated by comparing simulations to macroscopic, thermal properties against which no formal parameterization has been conducted. Specifically, the thermal volume expansion and ionic mobility of the crystal, glass and melt are evaluated.

Reference values for the crystal are taken from literature, where the temperature dependent lattice constant has been determined experimentally [166] and diffusion barriers for the vacancy diffusion mechanism have been reported in different DFT studies [179, 196]. In contrast to this, reference values for the glass or melt are not available at a reliable accuracy. For this reason, the here conducted AIMD simulations (see above 5.3.1) serve as a comparison. Although, some reference structures of the very same data are also included in the training set, their sensitive temperature dependence is not.

For the evaluation of trial potentials, the temperature dependent volume is equilibrated for 100 ps in NPT MD simulations using crystal, glass and melt structures containing 135 atoms. NEB calculations for the diffusion barrier in the crystal are computed using eight images in a $3 \times 3 \times 3$ supercell of Li_3OCl where a vacancy is introduced via a Li-Cl Schottky defect. The diffusion coefficients in melt and glass are sampled over 500 ps in NVT MD simulations. For this, the very same initial configurations as employed in the AIMDs reference calculations are employed to ensure a best possible comparability. Hereby, the force field MD exceeds the AIMD statistics of 100-200 ps, from which a lower standard deviation can be expected.

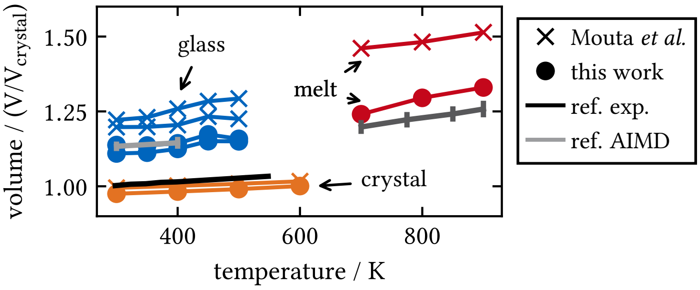

Fig. 5.3: Volume against temperature for the validation of the force field potentials. Included are the volume expansion of the crystal (orange), the glass (blue), and the melt (red). The references are indicated with solid lines and are taken from literature for the crystal or AIMD simulations as described in the text. Compared are the potential including core/shell particles with parameters from Sec. A (circles) and the one of Mouta *et al.* [76] (crosses).

As shown in Fig. 5.3 the here parameterized potential reproduces the density of the glass quite well. It can be noted that above 400 K the volume expansion increases which hints to a liquification of the system as expected for the glass transition. In comparison to this, the crystal and melt are not as well represented. In the melt an overestimation of the volume by 3-10 % can be seen, which points to inaccuracies of the potential to produce the far tail of the long range interactions. The crystal on the other hand is underestimated by 2-3 % which is rather a sign of inaccuracies in the reproduction of the Madelung potential [39]. Considering the deviation in melt and crystal, the here compared volume represents a very sensitive parameter in comparison to the usually compared lattice constants. Thereby, deviations of similar magnitute are also found in DFT studies of crystalline Li_3OCl. Reported lattice constants show differences of up to 3% when translated to volume [197, 198]. Despite these deviations for melt and crystal, it is shown that the force field potential is successfully tuned to accurately reproduce the glass density relevant for this work.

Considering ion mobility in the crystal, the force field potential reproduces the vacancy migration barrier at 0 K sufficiently accurate with 0.29 eV which compares well with values obtained via DFT of 0.31 eV [179]. In contrast to this, the comparison of diffusion coefficients in the amorphous phases from MD simulations is more ambiguous (see Tab. 5.3). This is due to the insufficient statistics, in particular in the AIMD, for the determination of the ion migration. Especially pronounced in the small cells of the glass configurations, the associated errors easily exceed 100 %. Thus, only a qualitative comparison is possible to estimate the ion diffusion. With this in mind, the determined diffusion coefficients compare surprisingly well. At all temperatures Li, Cl, and O mobilities are found to be on the same order of magnitude. A seemingly systematic overestimated by a factor of 1.5-2.0 by the force field potential portrays an acceptable deviation. In the melt, the associated error in the diffusion coefficients is considerably lower — evidence for its ergodic behavior. Here, the overestimation by the force field potential becomes clearer. Besides the quantitative differences, phenomenological trends are consistent. Those are the apparent mobility of Cl ions in the glass (see discussion in Sec. 5.5) as well as a peculiar order in the long range diffusion coefficients of $D_{Li} > D_{Cl} > D_O$ in the melt. Here, the strong Li-O interaction forms a volatile network of mixed edge and corner linked OLi_6 units and the oxygen ions diffuse with a continuously exchanging Li "solvation shell".

Tab. 5.3: Diffusion coefficients as obtained from the AIMD reference and the force field validation calculations for the here obtained potential and the potential by Mouta *et al.* [76] as a comparison. As described in the text the diffusion coefficients are obtained for Li, Cl and O in short NVT calculations with a system size of 135 atoms for the glass at 300 and 400 K and the melt at 900 K.

	AIMD	this work	Mouta *et al.* [76]
	glass (300 K)	/ 10^{-5} Å^2 ps^{-1}	
Li	18.706 ± 18.955	28.322 ± 14.936	0.698 ± 1.893
Cl	4.754 ± 4.259	9.613 ± 20.991	0.624 ± 1.636
O	0.717 ± 4.454	3.213 ± 5.282	0.467 ± 1.141
	glass (400 K)	/ 10^{-5} Å^2 ps^{-1}	
Li	45.410 ± 97.134	169.167 ± 94.721	0.123 ± 0.142
Cl	20.485 ± 101.132	16.460 ± 30.729	1.616 ± 1.278
O	0.470 ± 29.709	4.713 ± 6.689	1.128 ± 1.002
	melt (900 K)	/ 10^{-2} Å^2 ps^{-1}	
Li	22.459 ± 5.770	40.114 ± 3.227	12.109 ± 1.473
Cl	12.023 ± 1.621	30.616 ± 5.584	10.875 ± 0.970
O	5.903± 0.654	12.504± 1.128	4.305 ± 0.424

To put the performance of the derived potential into perspective, a comparison to the force field potential by Mouta *et al.* is conducted. Due to the lack of a parameterization for the amorphous phase, the potential predicts according volumes with a substantial deviation as shown in Fig. 5.3. This is due to the missing anharmonicity in the potential which also reflects in the wrong thermal expansion of the crystal. The latter is obtained at 300 K with $2.31 \cdot 10^{-5}$ K^{-1} which is, however, only slightly improved by the here derived potential with $2.91 \cdot 10^{-5}$ K^{-1} in comparison to DFT $3.89 \cdot 10^{-5}$ K^{-1} [166] and experiment $4.79 \cdot 10^{-5}$ K^{-1} [166]. It follows, that the empirical derivation only yields a correct description of the crystal at 300 K — i.e. the thermal equilibrium it was parameterized to. Considering the mobility, the vacancy diffusion barrier is reproduced with a similar error as in the here derived potential. Curiously, the diffusion coefficients in the amorphous phase are dramatically underestimated. Since Cl diffusion turns out as high as Li, it is suspected that the latter is slowed down based on an overbinding of Li to O. Thus, this empirically derived force field potential shows an ambiguous behavior as such an overbinding is not seen in the migration barrier of the crystal. It becomes evident, that this force field only yields an effective description of the crystal at room temperature void of microscopically accurate interactions.

5.3.4 Suggested improvements for future force field parameterizations

The parameterization of the potential as described in this section, involves a lot of input based on chemical intuition in the setup of the initial training set and the potential validation. Likewise, the parameterization procedure requires a major computational effort to find good initial trial potentials which serve as the basis for subsequent localized searches. Based on the usually vast parameter space, finding good starting points involves some luck. In order to improve on these non-systematic factors, some considerations shall be put forward in the following.

In the current approach, the physical constraints — fixing the van der Waals parameters $C_{\mathrm{Li-Li}}$, $C_{\mathrm{Li-O}}$ and $C_{\mathrm{Li-Cl}}$ to zero — give Li Coulomb interactions particular leverage. In that, the partial charge of Li presents the only parameter to control the Li-Li long range interaction. In combination with the other charges it thus delivers an effective background potential, synonymous with the Madelung potential in the crystal. Corrections to this point charge model follow from the van der Waals parameters $C_{\mathrm{O-O}}$, $C_{\mathrm{O-Cl}}$, and $C_{\mathrm{Cl-Cl}}$. In contrast to this, the Buckingham term with the parameters A_{ij} and ρ_{ij} only correct for the short range interactions with an overall less significant impact on the macroscopic physics.

Most trial potentials obtained by the strategy presented in Sec. 5.3.1 follow these systematic relations. This can be deduced from the sensitivity of the cost function on the parameters, i.e. to the measure of agreement to the reference data (see 3.1.1). Thereby, the PSO finds a best fractional charge relatively fast. A more tedious search is required for the C_{ij} parameters, for which however minima clearly converge (dependent on the charge). In contrast to this, the cost function is comparably insensitive to the Buckingham terms. This underlines their lack of importance on the intermediate and long range interactions if an optimal partial charge is found. In fact, most trial potentials converge with a minimum Li-Li Buckingham term, whereby all Li-Li interactions remain dependent on only the Coulomb interactions. Although these effects agree with the underlying physics of the force field terms, it needs to be acknowledged that these relations are not generally in place. In many potentials, Coulomb, Buckingham, and van der Waals interactions arbitrarily mix to reproduce effective interactions. Often, the Buckingham terms have a significant effective range to overcompensate ill-defined charges.

Considering this systematic finding, an adapted strategy is proposed:

1. A first optimization of the partial charge and the van der Waals parameters to a broad training set, including many chemically relevant structures is conducted. Here, Buckingham parameters would be constraint at minimal values - medium A_{ij} and small ρ_{ij}. A global minimum would be thus swiftly obtained.
2. In a second step, the Buckingham parameters would be adjusted to a specialized training set including many short ion distances to map an exact profile of the short range interactions.
3. A final readjustment of charges and van der Waals parameters by repeating the first step would follow.

4. Since it turned out to be very effective, the core/shell parameters would be adjusted in a subsequent physical parameterization as elaborated in Sec. 5.3.1

Albeit not tested, this strategy might reduce the sampling effort and enhance the quality of the obtained potential by strictly enforcing the physical meaning of each force field term. This can prove to be especially crucial for pair potentials as used here which have been shown to be very sensitive on the chosen parameters compared to many body potentials [199].

5.4 Obtaining a glass structure ensemble

The disorder in glasses results from a second order phase transition following the rapid cooling of a liquid. In that, a material approaches solidification continuously until a perceived structural arrest occurs at the glass transition. The gradual thermodynamic transformation yields an amorphous solid which is not at thermodynamic equilibrium. This shows for example in a density dependence on the synthesis procedure or observable secondary structural relaxation. The latter consists of non-translational, localized phenomena measurable by e.g. dielectric spectroscopy [119–121, 200, 201]. From a microscopic perspective, a glass is an amorphous solid, hence without any long-range order which resembles a frozen, liquid-like structure. The according energy landscape is a corrugated one, defined by many super basins describing possible configurations of an infinitely extending disordered random structure. A transition between such super basins corresponds to translational changes of the global network. Such transitions are only possible above the glass temperature or ultimately in the liquid phase when a system becomes ergodic. The super basins are interspersed by many local minima representing localized rearrangements of atoms. Transitions between these local minima correspond to the secondary relaxation described above. These can be constituted of a variable length scale, thereby including a varying number of atoms. Depending on the height of the barriers between such local minima, a comparably mobile glass network can be found at finite temperatures [121, 201–203].

Many challenges are to be faced when simulating such a material. Finite simulation cells with periodic boundary conditions cannot truly represent a disordered infinitely extended system, but merely give an approximation. Therefore, the simulation cells need to be chosen large enough, so that the enforced periodic boundary conditions do not influence the local disorder. Additionally, the vast amount of global configurations according to the super basins described above can only be sparsely sampled in a very limited subspace. Hereby, a representative picture can be approached by studying an array of glass structures to obtain a structural ensemble. Finally, temperature effects which sample structural rearrangements according to local minima in the energy landscape need to be sampled at long time scales in order to be statistically meaningful. This latter effect strongly depends on the depth of the minima and how relevant rare events are for the studied phenomena.

5.4.1 The melt-quench procedure

Glass structures are created using a melt-quench procedure, a method motivated by the conventional glass synthesis and regularly employed in simulation studies [120, 121, 164]. Simulation cells containing 1080 atoms are used corresponding to a chemical composition of $Li_{648}O_{216}Cl_{216}$. Since the density of the pure glass was not determined experimentally [166], a distribution of supercell volumes is studied. To this end, structural ensembles are created at constrained volumes of 1.12, 1.13, 1.14, 1.15 and 1.17 V_{crystal} distributed around the estimated volume from AIMD simulations (see above in section 5.3.1). This likely gives a more realistic representation of the material considering the non-equilibrium synthesis conditions of the glass [120, 166].

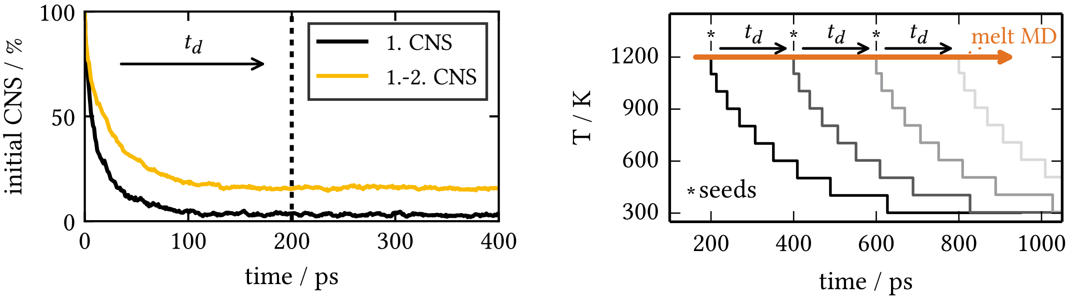

Fig. 5.4: (left) Decay of the first (black) as well as the combined first and second (gold) O-O coordination shell (CNS) via ion exchange over the course of the melt trajectory. It can be seen, that the combined CNS does not completely decorrelate, which is evident of the fast exchange within the melt. (right) Schematic representation of the melt-quench procedure temperature profiles for the example of the fast quench protocol (shades of gray). Indicated are the seeds which are drawn in the interval of the decorrelation times t_d from the melt MD simulation (orange).

For each volume 20 glass structures are quenched, seeded from a melt at 1200 K in which all ions show fast diffusion allowing for rigorous positional rearragement. The seeds are drawn every 200 ps to ensure that initial structures are decorrelated. This decorrelation period t_d is determined by monitoring the mean decay time of the first O-O coordination shell, which is equivalent to the mixing of the slowest diffusing species (see Fig. 5.4). Hereby, for each O ion the coordinating O ions within a radius $\approx 4\,\text{Å}$ for the first shell and $\approx 8\,\text{Å}$ for the additional second shell (as determined from the respective O-O RDF) are tagged at a time t_0. During the MD simulation of the melt the relative preservation of the original coordinating O ions is monitored and averaged over all O ions yielding the mean decay. This procedure is time averaged over different initial times t_0. For the quench, a stepped temperature profile with a step size of $\Delta T = 100\,\text{K}$ is chosen. Long dwelling times after each temperature drop are included to allow sufficient structural equilibration. The dwelling times are extended exponentially every step to account for the slower relaxation dynamics at lower temperatures (following the temperature decay $T(t) = 800\,K \exp(-rt) + 300\,K$ with r as the decay exponent). Two relaxation protocols are applied yielding an overall quenching rate of 0.26 and 1.32 K/ps (according to $r = 10^{-6}$ and $2 \cdot 10^{-7}\,\text{ps}^{-1}$). A relatively long structural relaxation is thereby enforced compared to the usual cooling rates applied in linear melt-quench procedures of 25-50 K/ps in AIMD [204–207] and 5-10 K/ps in classical MD simulations [191–193]. The total simulation time for each quench protocol amounts to 680 ps for the fast quench and 3.4 ns for the slow quench. All MD simulations are performed in an NVT ensemble as described in Sec. 5.2.

5.4.2 Characterization of the glass ensembles

In order to characterize the thermal behavior of the material with statistical relevance, sampling of thermodynamic properties is commenced after the quench for 1.5 ns in all structures. During this sampling, the NVT ensemble is maintained.

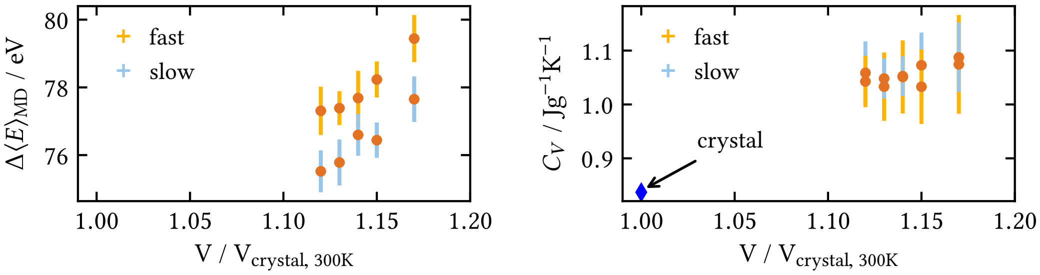

Fig. 5.5: Averaged thermodynamic properties of the quenched glass ensembles for the investigated volumes at 300 K. Note, each data point and corresponding standard deviation is based on the data of 20 structures (see above Sec. 5.4.1). (left) Average relative energy $\Delta\langle E\rangle_{\mathrm{MD}}$ sampled after the quench and referenced to the crystal. (right) Heat capacity C_V at constant volume with the theoretical crystal reference indicated (see text). Ensembles created with the fast quench rate are shown in yellow, and with the slow quench rate in light blue.

Complying with an ensemble based representation of a glass, the obtained structures are discussed as averages characterized by volume and quenching rate. Here, each ensemble corresponds to the average and standard deviation from 20 glass structures (see above Sec. 5.4.1). To classify the ensembles in the potential energy landscape picture, the time-averaged relative energy is compared (see Fig. 5.5). Each ensemble shows a distribution of energies where the included data points correspond to different super basins belonging to different glass network configurations. Despite this energy span, a clear separation of the fast and slow quenched ensembles is found whereby slow quenching rates yield lower energy structures indicating relevant thermodynamic relaxation at long time scales. The ensemble energies also show a decreasing trend with volume indicating an unambiguous convergence for the fast quench towards the equilibrated volume around 1.12 and 1.13 $\mathrm{V/V_{crystal}}$.

In comparing a second order phase transition to a glass against the according first order phase transition to a crystal, the change in thermodynamic properties is continuous compared to discontinuous. This is characteristically seen in the heat capacity whereby its bifurcation during the phase transition results in a lower value for the crystal [121, 200]. Therefore, the heat capacity C_V at constant volume of the glass ensembles is sampled based on the fluctuation of the potential and kinetic energy E_{pot} and E_{kin} as described in Sec. 3.3.3. A convergence of C_V with sampling time is ensured in order to capture sufficient secondary relaxation, i.e. transitions between the local minima in the energy landscape. As shown in Fig. 5.5, the expected [121, 200] relation of C_V at a higher value for the created glass ensembles in comparison to the crystal is found. The latter is calculated on basis of the same interatomic potential.

The glass structures of the ensembles can be characterized by the time averaged radial distribution function (RDF) as shown in Fig. 5.6. The ensemble-averaged RDFs have a shape typical for systems with no long-range order like liquids or amorphous solids. They thereby converge to the normalized bulk density (= 1) at which point all short range order is lost [189]. This convergence indicates that the used simulation cells with a minimum box length of 24.3 Å (1.12 $\mathrm{V/V_{crystal}}$) suffice to describe the long range disorder present in the investigated glass. Interestingly, the RDFs show a coinciding behavior independent of volume or quench rate. This is despite the energy differences observed for the different quench procedures. Thus, the glass maintains a

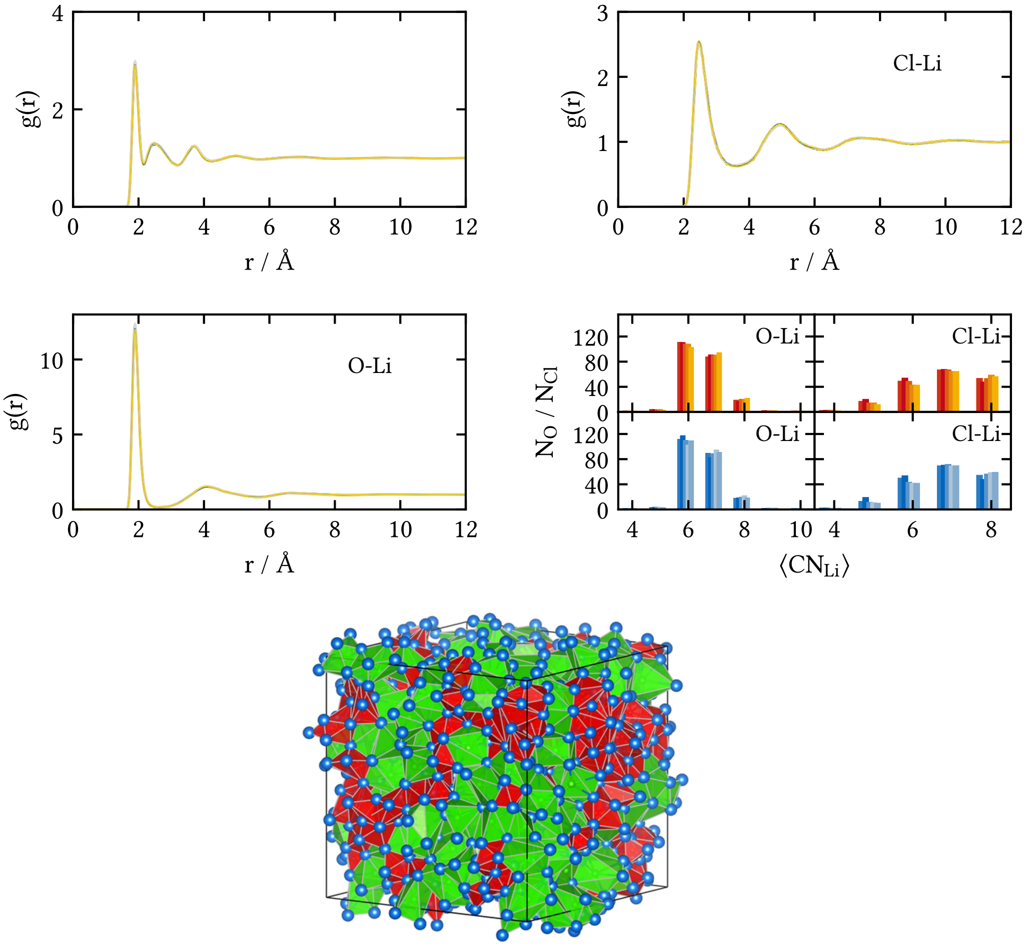

Fig. 5.6: Structure properties of the quenched glass ensembles for the investigated volumes at 300 K. Time averaged (top left) all-ion (top right) Cl-Li and (middle left) O-Li RDFs g(r) as a mean for the different ensembles. Note that all RDFs coincide. (middle right) Ensemble averaged histogram of the time averaged CNs within a cutoff of 2.5 Å for O-Li and 3.5 Å for Cl-Li. Ensembles created with the fast quench rate are shown in shades of yellow, and at slow quench rates in shades of blue, where lighter shading depicts larger volumes. (bottom) Exemplary glass structure as resulting from a fast or slow quench. Li is depicted in blue, O-Li and Cl-Li coordination polygons are depicted in red and green, respectively.

liquid-like glass structure during relaxation where an overall short-range order decorrelates at 10 Å. As shown exemplarily in Fig. 5.6 individual small agglomerates of amorphous Li_2O and LiCl are formed. Considering these different chemical environments based on the O and Cl coordination by Li, the individual RDFs as well as the according time averaged CNs are compared as shown in Fig. 5.6. The O-Li coordination shows a strong randomization where specifically any short-range order is already lost beyond 8 Å. As seen in the first coordination shell of the RDF at 2.5 Å as well as in the CNs, it can be found that O-Li packing is comparably dense. Thereby, an octahedral environment or slightly higher coordination is found which is characterized by edge and corner sharing polyhedra (see exemplarily Fig. 5.6). In comparison to that, the Cl-Li shows a farther reaching short-range order in its RDFs where a decorrelation only appears beyond 10 Å. The resulting packing is less dense with a first coordination shell at 3.5 Å showing a less rigid coordination environment, whereby over- and undercoordination is apparent.

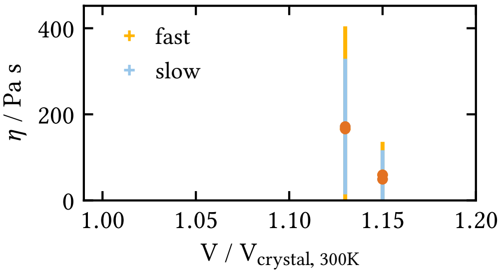

Fig. 5.7: Estimated shear viscosity η at 300 K. The viscosity is sampled over a correlation time of 500 ps for 4 ns for selected volumes of 1.13 and 1.15 $V_{crystal}$. Ensembles created with the fast quench rate are shown in yellow, and at slow quench rates in light blue.

To estimate the mechanical properties of the glass, the shear viscosity η is computed via the auto correlation function of the off-diagonal components of the stress tensor as described in Sec. 3.3.3. For this glassy material, the decay of the autocorrelation function extends far beyond the time scale of MD trajectories and needs to be approximated. Here, the mean of an exponential and linear fit to a correlation function averaged over a correlation period of 500 ps for each structure is taken. Unfortunately, this method lacks robustness which can be seen in the large standard deviation (outliers are discarded) in Fig. 5.7. Thus, the estimated η is not quantitatively reliable. Additionally, it is likely underestimated if a long time convergence leveling of the according correlation function is not captured in the sampling period. From this well-known effect for slow converging correlation functions [92] the obtained viscosity represents merely a low bound. As seen from the estimated values, the viscosity shows no significant sensitivity to the quench rate. In comparison to that, the volume strongly affects viscosity. Approaching the equilibrium volume, ensembles yield a viscosity > 100 Pa s which corresponds to typical values of semi-solids. Representing a low bound, this excludes the simulated material to behave like a true liquid. Nevertheless, the approximate low viscosity rather indicates a ductile glass-amorphous material than a typically stiff glass. A high ductility is therby a favorable property for a solid state electrolyte since it avoids complex manufacturing in order to ensure crack-free contact to the electrodes [208].

5.5 Ion mobility

Ionic diffusion in amorphous materials is inherently complex due to their disordered, non-periodic structure. From a single ion motion point of view, the number of coordination sites and according diffusion barriers is not discrete as in a crystal lattice but rather follows a distribution [16, 91, 163]. Additionally, collective ion motion is a general phenomenon which leads to strong activation and correlation effects [16, 201]. Percolation through the material would then depend on the highest migration barrier, if a rigid host network is assumed [104, 163]. However, structural relaxation of the host network — common in a weak glass — may continuously change the potential energy landscape similar to the reaction of a solvent to the migration of a solute [164]. These considerations on the complexity of ion diffusion are based on fast ion conducting glasses where foreign ions (glass modifiers) diffuse within the excess volume of a host network (glass formers) [16, 163, 164]. In the glass-amorphous Li_3OCl this situation is not given since Li is both network forming and the mobile species. Therefore, a decoupling of viscoelastic relaxation and ionic conductivity below the glass temperature [119, 164, 209] can only apply if structure-giving and mobile Li ions can be strictly separated. Due to this lack of a lattice or a clear host network to charge carrier separation, the elemental diffusion processes in the glass cannot be predicted easily from chemical intuition. To investigate such a complex ion transport, MD simulations provide the most practical method. Propagating the system at finite temperatures thereby allows the ions to explore the configuration space autonomously yielding the effective ion motion.

5.5.1 Ion diffusion in glass-amorphous Li_3OCl

To gain insight into the ion migration, classical MD simulations for 4 ns are conducted after the individual glass quenches at 300, 340 and 400 K (see Sec. 5.4). Here, only the glass ensembles at the volumes 1.13 and 1.15 V_{crystal} are investigated due to the high computational cost. As shown exemplarily in Fig. 5.8 the sampled mean square displacement (MSD) shows a rather irregular behavior even over the long timescale indicative of the slurry dynamics in this disordered material. Surprisingly, not only Li but also Cl ions migrate at 300 K. This stands in contrast to the O ions which only exert minor rearrangement, as seen in their low MSD. This mobility behavior is qualitatively confirmed on the short time scales of AIMD simulations, i.e. at a high chemical accuracy (see details in Sec. 5.3). In characterizing the statistical time dependent diffusion [90], the MSD is taken as a time average $\langle \text{MSD} \rangle$ (see Sec. Fig. 5.8). From this $\langle \text{MSD} \rangle$ the phenomenological diffusion behavior can be deduced. In the ballistic regime occurring at a time scale ≤ 50 ps, ions already show a large instantaneous displacement (indicated by the dotted lines in Fig. 5.8). This is due to large amplitude vibrations in the excess volume of the amorphous material. It follows a transition regime where ions are subject to collisions and cooperative effects which converges unusually slow in time, especially for Li. The long range transport follows with the typical normal diffusion behavior. For all investigated trajectories this long range migration is derived by a fit to the long-time (orange dashes in Fig. 5.8) linear part of the MSD which will also be the used quantity in the further statistical analysis.

As a measure for the long range ion transport, the tracer diffusion coefficents are evaluated from the Einstein relation based on the linear part of the MSD (see Sec. 3.3). In Fig. 5.8 the diffusion coefficients are shown as averages of the structural ensembles defined by volume and quenching rate (compare Sec. 5.4). Naturally, the Li diffusion is considerably higher than the Cl diffusion. Nevertheless, the latter still shows a true long range mobility with finite diffusion

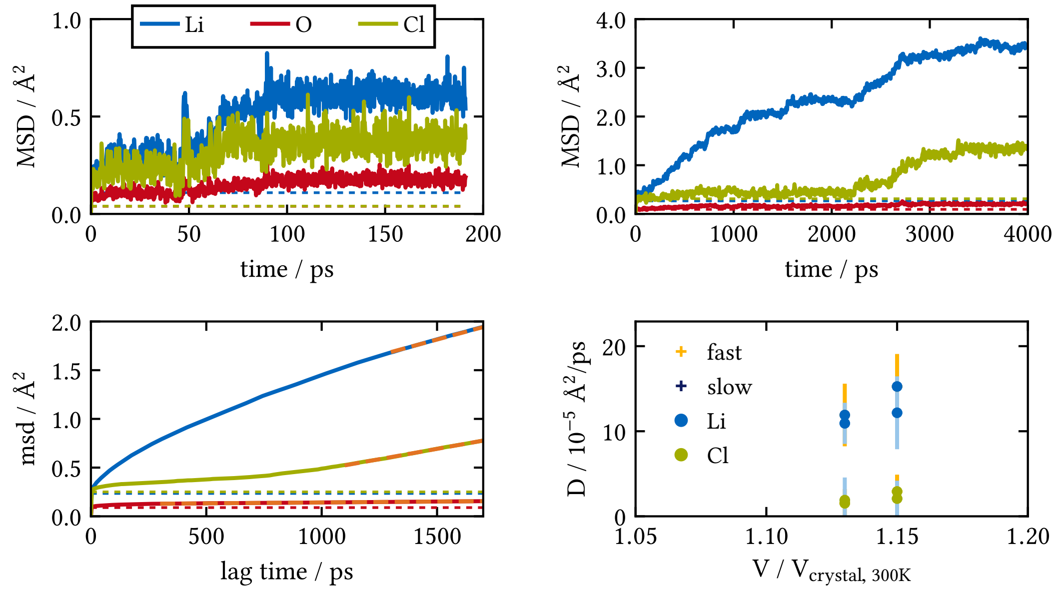

Fig. 5.8: Exemplary MSDs from MD simulations at 300 K of trial glass configurations with a volume of 1.13 V_{crystal} from an AIMD (top left) of a system with 135 atoms and from a classical MD (top right) of a system with 1080 atoms, as well as the time averaged MSD of the latter (bottom left). The ballistic motion on quasi-instantaneous timescales corresponding to the vibration is marked with dotted lines. The orange striped lines indicate the fit to the long range migration behavior. (bottom right) Averaged diffusion coefficients of each studied ensemble for Li (blue) and Cl (green) ions. Ensembles created with the fast quench rate are shown in yellow, and at slow quench rates in light blue.

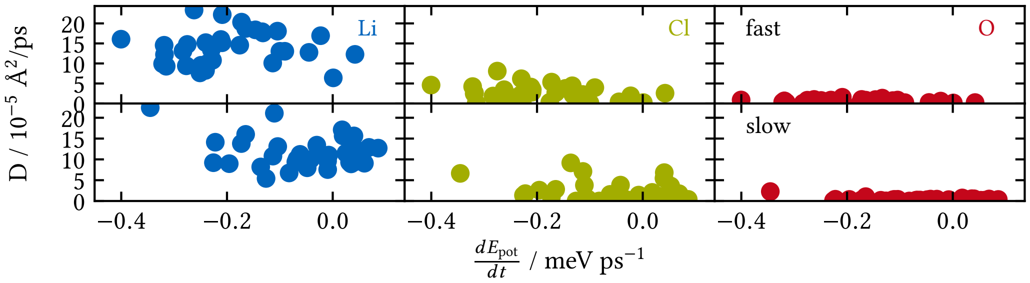

Fig. 5.9: Diffusion coefficients of Li, Cl and O plotted against structural relaxation of the glass samples monitored by the average rate for the overall change in potential energy for each MD simulation at 300 K.

coefficients. Among the different ensembles, the diffusion coefficients show little deviation. This is not suprising with respect to their near identical short range order (see Sec. 5.4.2). In that, only the fast quenched ensemble in the extended volume of 1.15 V_{crystal} shows an effect on both Li and Cl diffusion. This is possibly due to a larger excess volume in the glass network facilitated by the fast quench in the larger cell. In the corresponding slow quenched ensemble this excess volume has likely closed as hinted by the lowered diffusion.

Since a continous structural relaxation is expected in a glass [121, 201, 202], it suggests itself that the observed diffusion might be a direct result thereof. Indeed such a relaxation can be observed in many structures. However, the according relaxation is minor involving only a few 100 meV per simulation cell over the course of the 4 ns simulation. A correlation to the diffusion is estimated by relating the single diffusion coefficients of Li, Cl and O against the average rate of the change in potential energy dE_{pot}/dt for each MD simulation. As shown in Fig. 5.9, only a weak correlation between the diffusion coefficients and the energetic relaxation of $< 1\,\%$ for Li and Cl is found. Hereby it can also be seen, that O remains virtually immobile in all trajectories and does not partake in relaxation processes. Thus, it is concluded that any relaxation only corresponds to light structural rearrangements and the observed diffusion coefficients embody true long range transport.

Tab. 5.4: Share of Li and Cl ions (in %) which show long range mobility according to an individual maximal displacement ≥ 3.5Å at any point of the trajectory. Averages are taken for the slow and fast quenches as indicated.

	slow			fast		
	300 K	340 K	400 K	300 K	340 K	400 K
Li	36.7	63.9	94.2	44.3	72.3	96.4
Cl	9.5	20.0	50.6	14.5	30.5	60.8

Considering the detailed ion motion, single ion trajectories are evaluated based on the overall displacement and the mean chemical environment expressed via an averaged CN. Ions which travel further than 2.5 Å (i.e. beyond the first coordination sphere, see Fig. 5.6) are thereby considered to show true mobility. Already at 300 K, a large share of Li ions ($\approx 40\%$) and a considerable share of Cl ions ($\approx 12\%$) is mobile (see Tab. 5.4). These shares increase gradually with temperature until at 400 K most of the Li ions and half of the Cl ions show diffusion. This trend coincides with the experimentally found glass transition temperature of 392 K [166] where the glass gradually transforms to a supercooled liquid. In comparing the ensembles based on the quenching rate, the slow quenched ensembles show slightly less mobile ions. In the latter, these are likely more favorably bound within the glass network. This also explains the observed energy stabilization of the slow quenched ensembles (see Sec. 5.4.2). Matching the mobile ions to their average CN as shown in Fig. 5.10 allows to estimate in which chemical environment highest ion mobility occurs. For Li, fastest diffusion is found at a high Cl CN of 3-5 and a low O CN of 0-2 which points to the amorphous LiCl agglomerates and its interface to the Li_2O phase. A moderate diffusion is found within the Li_2O phase. These trends can be linked to the stronger binding of O, yielding a tighter glass network with less excess volume. For Cl, no distinct correlation is seen meaning that Cl diffuses homogeneously. This phenomenological behavior stays consistent at higher temperatures.

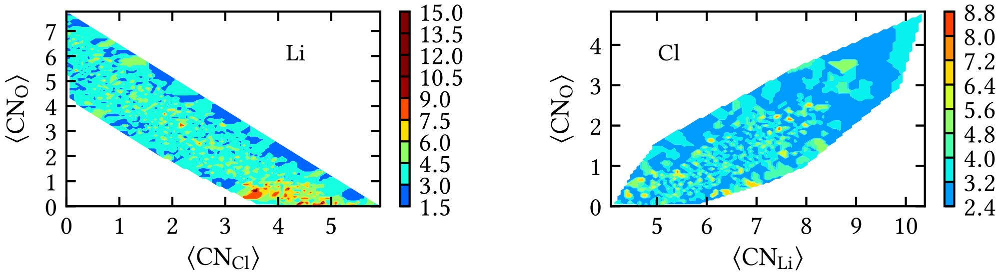

Fig. 5.10: Correlation between migration and CNs for (left) Li and (right) Cl motion at 300 K. The colormap shows the displacement of mobile ions ($\Delta r > 2.5$ Å) against the time averaged CNs.

5.5.2 Ion conductivity in Li_3OCl

To estimate the ionic conductivity from the ion migration, the Einstein formulation of the charge diffusion [96] is employed (see Sec. 3.3.1). Here, only the Li and Cl motion is taken into account. This is due to the reason, that the negligible oxygen motion is strongly emphasized in the squared dependence of the charge in the Einstein formulation. Considering longer simulation times, this effect would disappear as the O contribution would be dwarfed by long-range diffusing Li and Cl which is for example seen at the elevated temperature of 340 K.

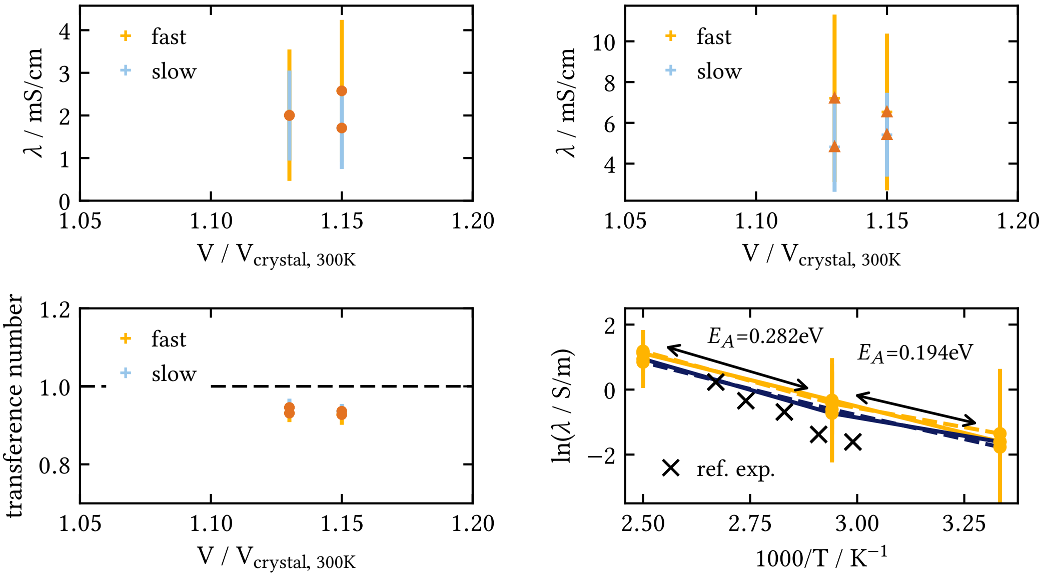

Fig. 5.11: Ensemble based ion conduction properties. Ionic conductivities λ following the Einstein formulation for the current [96] are shown for 300 K (top left) and 340 K (top right). (bottom left) The corresponding Li transference numbers at 300 K (see text). (bottom right) Arrhenius relation of the ion diffusion with the here included temperatures. The corresponding experimental data [166] (denoted "ref. exp.") is plotted with black crosses. Ensembles created with the fast quench rate are shown in yellow, and at slow quench rates in blue.

As shown in Fig. 5.11, an overall high conductivity around ≈ 2.0 mS/cm is found. This is associated with a large uncertainty, since the different glass configurations are subject to strongly varying ion diffusion. This is mainly based on the irregular occurrence of Cl motion in the different configurations. The latter exerts a considerable influence on the charge transport as a moving counter ion. At an elevated temperature of 340 K the conductivities climb to ≈ 5.0 S/cm in the slow quenched ensembles which only deviates from the experimentally reported value of 2.1 mS/cm at 335 K [166] by roughly a factor of 2. At this elevated temperature, the fast quenched ensembles exhibit pronounced higher conductivities in comparison to a coinciding conductivity at 300 K. This likely points to a low-temperature liquification based on the less integrated, higher energy structure. The apparent conductivity via the temperature dependence in the Arrhenius relation is depicted in Fig. 5.11 (bottom right). The marked experimental data (crosses) shows that a noticeable temperature dependence can be expected. In comparing that, only an estimate can be made based on the few temperatures treated here, where the two available temperature fronts are separated (the linear relation between neighboring data points). These exhibit effective activation barriers of 0.19 and 0.28 eV between 300-340 K and 340-400 K, respectively. The low temperature front compares well with the experimental activation barrier of ≈ 0.21 eV. In contrast to that, at higher temperatures the force field potential underestimates the energy activation barrier. This is likely due to the constraint volume of the simulation, since the experimental high temperature barrier is associated with a volume expansion at the glass transition.

In deducing the conduction mechanism, the Haven ratios — i.e. the relation between the tracer diffusion and the conductivity diffusion coefficient $\mathrm{H_R} = D^*/D_\sigma$ — are determined (see section 3.3.1). Hereby, the tracer diffusion coefficient D^* represents the average single ion mobility in a random walk like depiction. In comparison to that, D_σ represents a diffusion coefficient including any correlation and activation effects. As shown in Tab. 5.5 the overall $\mathrm{H_R}$ show a values within 1.0-2.0 which points to a slower charge transport than the overall ion diffusion. Such values are comparable to ionic liquids where a strong correlation of Brownian motion and Li hops between solvent molecules yield complicated back correlation effects [96, 106]. Interestingly, the single ion $\mathrm{H_R}$ show values between 0.4-0.7 which point to an opposite relation: faster charge transport than ion diffusion. This is also the relation found in conventional fast ion conducting glasses, where $\mathrm{H_R}$ is normally between 0.1-0.8. A higher conductivity than the actual ion diffusion results from cooperative and collective effects [91, 104, 201]. The discrepancy between the overall and single ion $\mathrm{H_R}$ reveals the mechanistic relationships within the investigated glass. In that, ions independently move within the instantaneous amorphous host in a glass-like collective motion. However, the fast moving charge centers given by Li and Cl, show a coupled, parallel motion, reducing the overall charge transport and thus yielding the high overall $\mathrm{H_R}$. Considering, the decrease of the overall $\mathrm{H_R}$ with temperature (see Tab. 5.5), it can be seen, that this coupling disappears when approaching the glass transitions. Here, the system becomes more fluid-like allowing for a random motion.

Tab. 5.5: Haven ratios $\mathrm{H_R} = D^*/D_\sigma$ of the overall Li and Cl conductivity (full) and of the single ions at the temperatures (T) 300, 340 and 400 K.

T	full	Li	Cl
300	2.19 ± 0.99	0.67 ± 0.32	0.40 ± 0.35
340	1.91 ± 0.97	0.66 ± 0.36	0.52 ± 0.39
400	1.54 ± 0.87	0.59 ± 0.34	0.59 ± 0.39

5.5.3 *Effects of the Cl mobility on the electrolyte performance*

Considering the observed Cl mobility, the overall ion conductivity does not represent the effective Li transport relevant for battery application. This relation in which Li ions contribute to the total conductivity can be expressed via the transference number $t_x = I_x / I_{\text{tot}}$, the ratio of the current I_x contributed by a species x to the total ion current I_{tot}. Here, the corresponding single ion conductivities I_x are determined from the Einstein formulation as described in Sec. 3.3.1. The Li transference number is comparably constant for all structural ensembles with $t_{\text{Li}} \approx 0.95$ (see Fig. 5.11). t_{Li} directly relates the effective Li conductivity to the total conductivity [96] which is therefore only slightly lowered and still yields ≈ 1.9 mS/cm at 300 K.

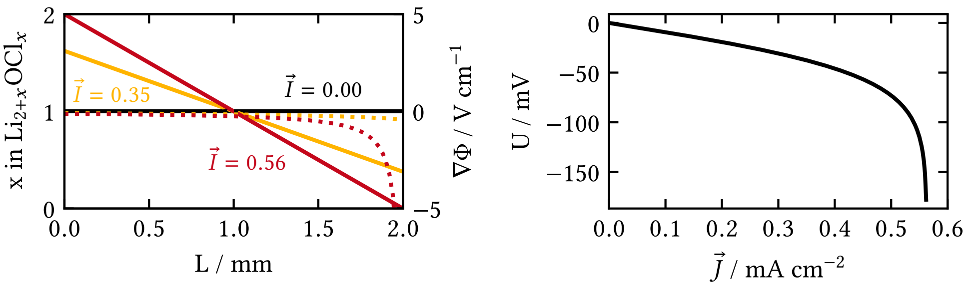

Fig. 5.12: (left) Polarization concentration profile expressed in the stoichiometric composition x in $Li_{2+x}OCl_x$ and the corresponding electric field for different currents (in mA cm^{-2}) along a one dimensional model cell (see text). (right) The current density $\vec{J}$ to potential U relationship resulting from the model.

Although the observed Cl motion does not contribute to the relevant charge transport, it nevertheless critically affects the operational ion current. When applying an electric field during operational conditions, ions and counter ions migrate in opposite directions which leads to a concentration polarization. Here, Cl ions accumulate at the counter electrode and bind Li ions due to the necessity to maintain charge neutrality. Along the applied potential, the amount of mobile Li ions decreases which lowers the power density of the material and ultimately limits to a maximum applicable current [210].

In order to estimate this effect, a one dimensional cell model is employed with the following assumptions derived from the simulations: In the electrolyte Li_3OCl, each immobile O ion with a charge of $z_O = -2$ binds two Li ions ($z_{Cl} = +1$) forming a charge neutral amorphous Li_2O host network. Within this network Cl ions and Li ions diffuse as a binary electrolyte (no convection). Additionally, the diffusion coefficients are assumed to remain constant, independent of local Cl and Li concentration. This assumption is based on the fact that the local electrostatic effects are already included in the ensemble averaged diffusion coefficients. Secondly, due to the Li_2O and LiCl agglomerates in the glass structure, an uneven Cl / Li concentration gradient is likely along the electrode cross section (see Fig. 5.6). Thus, a continuous phase network close to the original composition Li_3OCl throughout the material can be assumed. This would guarantee a steady conduction according to the averaged diffusion coefficient. Furthermore, magnetic correlation is neglected. This yields a binary system that can be considered like a dilute electrolyte via a simplified Nernst-Planck equation [211, 212]:

$$\frac{\partial c_i}{\partial t} = -D_i \nabla^2 c_i + \frac{D_i z_i e}{\mathrm{k_B} T} c_i \nabla \Phi \tag{5.1}$$

where c_i, D_i and z_i are the concentration, diffusion coefficient and charge of species i, e is the elementary charge, $\mathrm{k_B}$ the Boltzmann constant and T the temperature. The time dependent diffusion thereby depends on Fick's law of diffusion and electrostatic polarization following the electric field $E = -\nabla\Phi$. Under operation conditions a steady state $\frac{\partial c_i}{\partial t} = 0$ will be reached which depends on the applied current I or its respective current density $\vec{J} = I/A$ perpendicular to the electrode cross section A. In the steady state, the flux of Cl ions will be zero and an equilibrating concentration profile will therefore only depend on the flux of Li ions [211]:

$$\vec{J} = -2 z_{Li} e D_{\mathrm{Li}} \frac{dC}{dx} \tag{5.2}$$

where $\frac{dC}{dx}$ is the concentration gradient along the one dimensional cell with length $0 \leq x \leq L$ (see a detailed derivation in the Appendix B). As input for the model serve the average Li diffusion coefficient $D_{\mathrm{Li}} = 12 \cdot 10^{-5}\,\text{Å}^2\mathrm{ps}^{-1}$ at 300 K, an equilibrium concentration C_0 according to the here determined density of 1.770 g cm^{-3} (see Sec. 5.3), and a cell length of 2 mm as also used in trial cells by Braga *et al.* [166]. Concentration profiles according to applied currents as shown in Fig. 5.12 are determined. The limiting current for the binary electrolyte at which the concentration of Cl at the electrode drops to zero is found to be around 0.56 mA cm^{-2}. The corresponding electric field curves are also shown in Fig. 5.12. For the limiting current density it can be seen, that a rapid potential drop suddently appears, representative of the interfacial resistance building up due to the depletion of charge carriers [22].

When reaching the limiting potential in glass-amorphous $\mathrm{Li_3OCl}$, the material would still remain Li conducting in contrast to the dilute binary Li-Cl electrolyte used in the model. This is due to the persisting $\mathrm{Li_2O}$ host network which is itself conductive. However, maintaining currents which strongly exceed the limit current is probably difficult. A likely unfavorable stability of the isolated low density $\mathrm{Li_2O}$ host network would yield a thermodynamic driving force against the complete Cl depletion at the electrode. In overcoming the latter, induced chemical reactions would be imaginable leading to the degradation of the electrolyte interfaces. These considerations, however, remain speculation since experimentally probed current densities using a dilutely doped glass-electrolyte have not yet exceeded into the limiting regime. For example, in the above mentioned cell, maximum current densities have only been probed until 0.1 mA cm^{-2} [166]. Nevertheless, for practical high power applications where current densities of 10 mA cm^{-2} are necessary [22], the concentration polarization may become performance limiting. Here, the according effect would have to be countered by using thin electrolytes. Following the relations from the one dimensional model, these would need to be in the range of 10-100 μm. As reported in [172], such thicknesses are realizable for this material.

5.6 Sensitivity to the force field potential

As discussed in Sec. 2.2 and 5.3 force field potentials are expected to be sensitive towards the employed parameters. Most of the trial parameter sets tested in this work which are derived from the final training set show, however, a similar microscopic behavior as described above. Nevertheless, some earlier potentials not subject to a comprehensive training set, differ substantially in their phenomenological behavior. An interesting example shows overbinding between Li-Cl that leads to strong agglomeration towards phase separated LiO_2 and LiCl. Thus, the resulting macroscopic material resembles more a glass-ceramic than a homogeneous glass. Although this effect originates in a strong overestimation of the stability of this phase separation and is therefore chemically inaccurate, the resulting ensembles are worthwhile for a discussion.

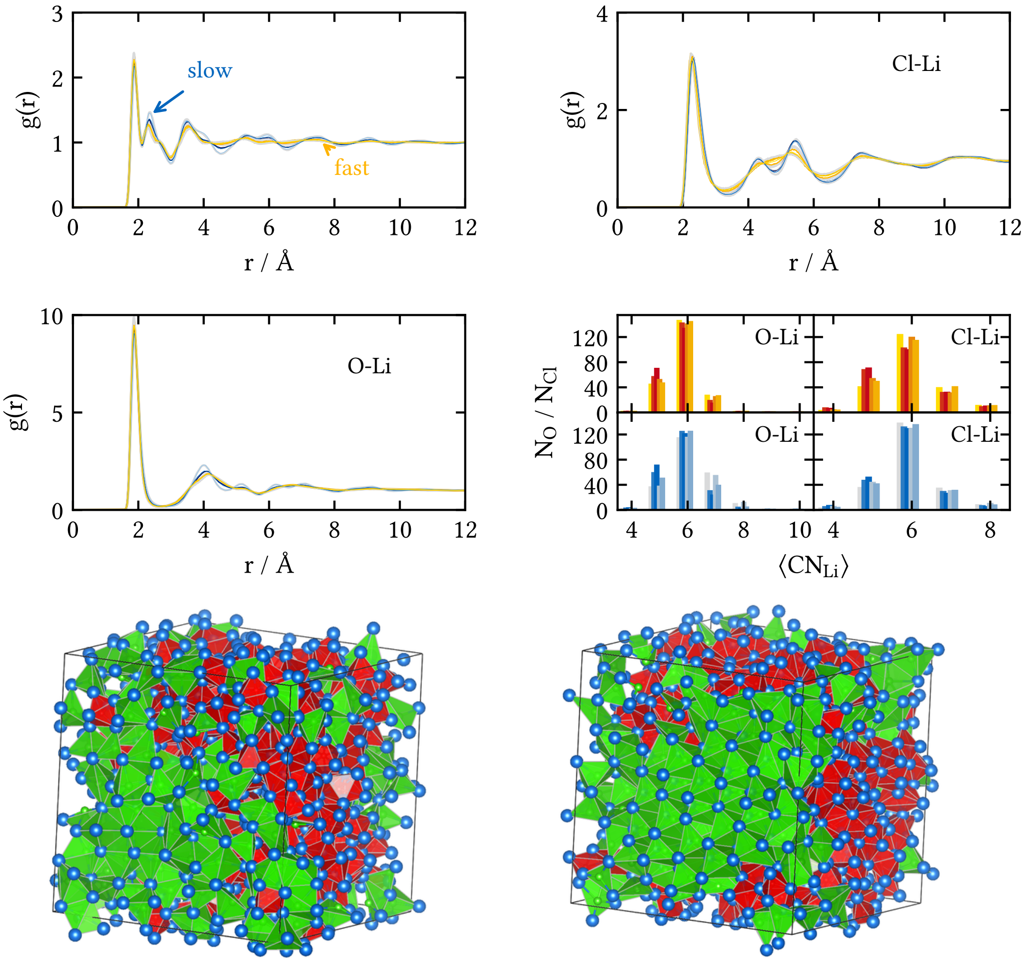

Fig. 5.13: Structure properties of the quenched glass ensembles for an alternative force field potential at 300 K. (top left) All-ion (top right) Cl-Li and (middle left) O-Li RDFs g(r) averaged for the different volumes. (middle right) Ensemble averaged histogram of the time averaged O-Li and Cl-Li CNs within a cutoff of 2.5 Å and 3.5 Å, respectively. Ensembles created with the fast quench rate are shown in yellow, and at slow quench rates in blue. The averaged RDFs and CNs are additionally depicted with lighter colors for smaller volumes. (bottom) Exemplary glass structures resulting from a fast (left) and slow quench (right) of the same seed. Li is depicted in blue, O-Li and Cl-Li coordination polygons are depicted in red and green, respectively.

The respective force field potential gives similar quench rate and volume dependencies on the energies as the force field potential in the preceding chapter. However, the quench rate dependent structure ensembles differ noticeable as shown in Fig. 5.13. Here, the RDFs of the fast and slow quenched ensembles are well distinguishable. While the Li-O RDF is only subject to slight deviation in the short-range ordering, the Cl-Li RDF shows a fundamentally different shape depending on the quench rate. In that, the slow quenched ensembles have a particularly long-range order, which decorrelates only around 12 Å. In the corresponding CN plots, this can be recognized in a large share of octahedrally coordinated Cl ions. As exemplarily shown in Fig. 5.13, these originate in the formation of LiCl crystallites. In contrast to this, the fast quenched structures do not show such crystallization, but are still subject to a phase separation of an amorphous LiO_2 and LiCl phase. It should be noted, that these crystallites are unlikely present in the experimental glass-amorphous Li_3OCl since no evidence can be found in respective XRD spectra [166]. In the latter, crystallites would usually be identifiable as it is known from other glass-ceramics [213–215].

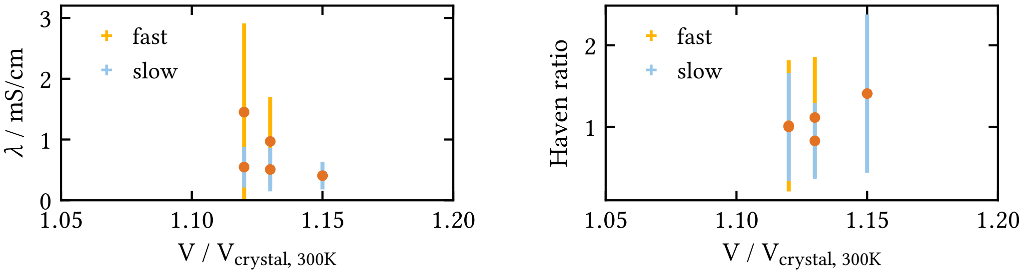

Fig. 5.14: Ensemble based ion conduction properties for an alternative force field potential at 300 K. (left) Ionic conductivity λ following the Einstein formulation for the current [96] at 300 K. (right) Ensemble based Haven ratios at 300 K. Ensembles created with the fast quench rate are shown in yellow, and at slow quench rates in blue.

Curiously, the ion mobility in these phase separated structures exhibits comparable behavior to the more accurate force field potential described in the preceding sections. In that, Li ions show a reduced diffusion coefficient. On the one hand, this is based on an inherently slower movement and on the other on a smaller number of ions participating in diffusion. Despite the stronger binding of Cl, it still exhibits motion to the same extent. The resulting conductivity is only slightly underestimating the experimental values as shown in Fig. 5.14. Additionally, the lower Haven ratios indicate a less coupled charge transport based on the more isolated ion diffusion events mostly concentrated at the interphase between Li_2O and LiCl. Here, the relation between Li and Cl yields a transference number t_{Li} of ≈ 0.8.

In conclusion, it can be seen that this alternative force field potential describes a mesoscopically different material. Despite this, the same macroscopic key characteristics as exhibited by the previously described force field are found with almost quantitative comparability. This underscores the observed insights about the macroscopic ion mobility in Sec. 5.5 for this highly unusual material and puts any inaccuracies resulting from an insufficient parameterization into perspective.

5.7 Conclusion and Summary

In this chapter, the glass-amorphous Li_3OCl has been investigated with a focus on its performance as a solid state electrolyte in Li ion battery applications. Using atomistic simulations, the microscopic structure and ion mobility are analyzed. The claimed extraordinary ion conductivity [166, 172, 174] is confirmed. Thus, any deceptive charge transport from side products of the glass synthesis procedure, like remaining water, can be excluded as a sole reason for the high conductivity. A surprising finding is the mobility of Cl ions which leads to an involved conduction mechanism. Here, a coupled Li and Cl motion is observed whereby each individual ion species is subject to collective diffusion. While the latter is a typical mechanism found in glasses, the former resembles more the conduction within an ionic liquid. Due to the motion of both Li and Cl a concentration polarization can be expected which will likely lead to a limited current/power performance of the electrolyte. This can only be overcome by using electrolytes of reduced thickness, hereby determined in the 10-100 μm range for high power applications. It should be noted that the here investigated pure Li_3OCl is not considered for battery applications but rather its dilutely doped variants. These exhibit slightly higher conductivity and a profoundly reduced temperature dependence with an activation energy of only 0.06-0.13 eV [166, 174]. From an atomistic point of view, the dopants might promote a less rigid glass structure otherwise encountered only at higher temperatures. Thus, it is likely that these would exhibit the here obtained picture with a different temperature relation.

The current data leaves some uncertainty. In that, the glass appears mechanically very soft from the computed shear viscosity. The latter is based on very approximate calculations which can only determine a lower bound. Additionally, the characteristics of the ion motion exhibit some fluid like behavior. This is not untypical for a glass, and likely pronounced based on the specialties of this material. Overall, further confirmation is necessary, in order to ensure the computational model to depict a glass and not its supercooled liquid counterpart.

The methodological effort of this work is founded in the force field parameterization and the combination of an involved analysis to deduce atomistic and microscopic behavior in detail. For the former a well-working strategy has been developed yielding an accurate potential, able of a precise reproduction of DFT level interactions. The high quality predictive capability of the parameterized potential has thereby been confirmed in an extensive validation. The ionic diffusion and conductivity is evaluated thoroughly using methods from statistical mechanics as more closely presented in Sec. 3.3. In order to dismantle different characteristics hidden in the chaotic ion motion in this highly disordered material, these methods present a superior approach.

6 Summary, Conclusions and Outlook

Computer simulations have been playing an important role in driving the research of battery materials over the last decades. A plethora of computational studies, typically based on density functional theory (DFT), have been most illuminating. These aim at the prediction of material performance in terms of structure-property relations [3, 4, 24] or the deduction of guidelines for the rational design of new compounds [4–8, 26]. However, the rather small DFT model systems that are computationally tractable with present day resources represent a severe limitation. They unavoidably fail to capture the considerable structural disorder that is often present in such materials. Notwithstanding, this aspect may have a crucial impact on operative kinetic processes such as macroscopic ion transport, and hence also on battery performance.

The main challenge in capturing structural disorder in corresponding theoretical models is the inclusion of configurational entropy. This relates directly to the simulated structures, both in terms of size (i.e. number of atoms) and phase-space sampling. The latter calls for addressing not only the most stable structure (or structures), but an entire thermal ensemble of potentially representative configurations. Considering also the large simulation sizes that are required, this translates to an extensive combinatorial problem. The latter encompasses an almost staggering amount of possibilities for the atomic degrees of freedom (DOF) — the full representation of which is far from trivial.

This thesis strategically combined a unique set of methodological tools and sampling techniques to explore the vast configurational space of battery materials. In order to access macroscopic length and time scales, while retaining all atomic DOFs, force field potentials were employed. These enable the explicit computation of large system sizes due to their advantageous numerical efficiency as compared to *ab initio* methods. The force fields were parameterized and/or validated against DFT to ensure that they provide a faithful representation of the underlying chemical interactions. On this basis, extensive statistical sampling was conducted which showed that the full flexibility of the atomic DOFs is absolutely necessary for describing the disorder and its influence on transport phenomena. This revealed unprecedented insight into disorder-induced implications to battery performance. The latter were showcased for two systems of great technological value, namely the anode material $Li_4Ti_5O_{12}$ (LTO) and the glass-amorphous Li_3OCl solid-state electrolyte.

In a first application to LTO (described in chapter 4 and published in Ref. [1]), Monte-Carlo (MC) sampling showed that low-energy structures are characterized by a high degree of microscopic inhomogeneity. Facilitated by the latter, novel disorder-stabilized Ti^{16c} antisite defects were discovered. As observed in molecular dynamics (MD) simulations, these promote a localized mobility that follows correlated diffusion. On this basis, a cascade-like mechanism was proposed which elucidates the formation of Li percolation channels during the Li intercalation process [137]. Consequentially, this explained the surge in Li ion conductivity upon Li insertion that has been measured experimentally [129, 130]. This disorder-induced mesoscopic ion transport mechanism fundamentally differs from the usually assumed bulk vacancy diffusion [16] and finally rationalizes the exceptional rate capabilities of LTO in battery applications.

The glass-amorphous Li_3OCl solid-state electrolyte [166, 172, 174] (described in chapter 5) was investigated in a second application. This material presents a special ion conducting glass since Li is the sole cation and thus simultaneously forms the host structure and acts as a charge carrier. MD simulations in structural ensembles revealed that not only Li but also Cl diffusion occurs as a likely result from this rather unusual composition. Individually, each ion species exhibited a diffusion mechanism typical for ion conducting glasses [16, 104, 163, 164]. However, their combination resulted in a coupled Li/Cl migration that ultimately changes the perceived conductivity. This mechanism suggests that Li diffusion is considerably higher, thereby rationalizing ion conductivities that have been reported experimentally [166]. In contrast, the observed Cl mobility likely influences the performance in a battery application through concentration polarization effects. Resulting limiting currents were thereby estimated. In light of these, a maximum electrolyte thickness of 10-100 μm was predicted for practical high-power battery applications.

This work overall underscores the importance of microscopic disorder to determine fundamental material properties and processes that are crucial to the operating performance in a battery. Such effects may only be illuminated from a multi-scale modeling approach, that allows for accurately bridging the gap between the micro- and mesoscale. The hereby presented strategy is uniquely set apart from commonly applied procedures which are unable to retain a high degree of atomistic detail when moving towards larger scales [2, 3, 9, 24]. Relying on large-scale simulations and extensive statistical sampling, this thesis thus offers a most detailed representation of ion mobility. This rationalizes experimental conductivities for two representative systems that lie at the frontier of battery research. It is reasonable to expect that much of the hereby derived physical insight extends also to other applications of configurationally disordered compounds. Ultimately, this opens the road towards a deeper understanding of transport phenomena in general. This in turn, helps to guide future efforts in designing the next-generation materials for electrochemical energy storage.

Notably, the devised methodology establishes a protocol that can be applied beyond a particular class of force fields. In this thesis, the latter are specifically based on the Born model of solids. While demonstrating sufficient accuracy for the presented purposes, these cannot depict the full chemical picture when e.g. involving atoms of mixed valence states. Therefore, the application of extended charge transfer force fields represents the obvious next step forward. These can describe varying oxidation states and hence electron transport processes. In this respect, a suitable candidate is the recent embedded-ion method (EIM) by Zhou et al. [216, 217]. This many-body potential was developed based on a charge-modified version of the modified embedded atom method (MEAM) [218–220]. Here, to ensure charge neutrality, the charges are determined from an embedded background potential rather than an explicit optimization procedure. While thus promising improved performance, this potential also follows excellent energy conservation during MD simulations. It is therefore rendered particularly suitable for the computational strategies proposed in this thesis. Ultimately, this will allow for investigating electron conduction that occurs alongside ion transport — an aspect that is particularly relevant during Li intercalation. Furthermore, it will enable the accurate description of unsaturated ions that appear at grain boundaries and interfaces [9, 25, 68, 151]. Finally, applications are envisioned that will also extend to metals and semiconducting materials. Especially in the case of the latter, the inclusion of slow electron transport via polaron hopping is crucial to the accurate description of ion diffusion since these processes occur on the same time scale [9].

Acknowledgments / Danksagung

First and foremost I would like to thank Prof. Dr. Karsten Reuter for the support and guidance during my time as a PhD student. My gratitude not only encompasses the scientific or strategic advice but also the many opportunities to look beyond the scope of the PhD thesis. Especially, the numerous visits to conferences as well as to collaborators in Jülich, Mülheim, and Stanford university need to be pointed out. Additionally, I would like to thank for the extended research visit at SLAC, Stanford university from which I gained scientifically as well as personally.

Likewise, I would like to thank my supervisor and mentor Dr. Christoph Schuerer for his effortless support. His ingenious scientific and technical input was invaluable for the progress of my projects. I would also like to thank him for the freedom and leeway he allowed for. In that, I certainly had much opportunity to explore new techniques and gain a broader background.

Also, I would like to thank Prof. Dr. Alan Luntz and Dr. Johannes Voss for mentoring me and their scientific guidance during my research visit at SLAC, Stanford university. Especially the time invested in lengthy scientific discussions was invaluable and illuminating.

I also owe my gratitude to many others which helped me in valuable discussions. Here I would like to point out Dr. Harald Oberhofer, Dr. Simon Rittmeyer, and Simone Swantje Köcher. I would also like to acknowledge the IT-team: Georg Michelitsch, Matthias Kick, David Egger, Christoph Schober, Christoph Muschielok, Juan Lorenzi and Christian Kunkel for all their support and for their friendship. Following up, much appreciation goes to the rest of the group, the old and the new members, for an incredibly pleasant atmosphere during my time there.

Besides the theory group I would like to thank my friends here in Munich and Cologne who showed great understanding for my no-shows in times of stress. I would like to express my deepest appreciation to my girlfriend Vanessa who always reassures me in times of self-doubt and showed great support, patience and love. Finally, I would like to thank my parents who always give their unconditional support and have helped me in every conceivable way. Without their care and their love, this journey would have been much bumpier if not impossible.

Garching, June, 2018

Hendrik Heenen

Bibliography

[1] H. Heenen, C. Scheurer, and K. Reuter, Nano Lett. **17**, 3884 (2017) (cit. on pp. i, iii, v, 29, 36, 43, 44, 48–51, 53, 55, 59, 91).

[2] A. Van der Ven, G. Ceder, M. Asta, and P. Tepesch, Phys. Rev. B: Condens. Matter Mater. Phys. **64**, 184307 (2001) (cit. on pp. iii, v, 2, 34, 35, 38, 43, 44, 52, 58, 61, 92).

[3] Y. Meng and M. Dompablo, Energy Environ. Sci. **2**, 589 (2009) (cit. on pp. iii, v, 1, 2, 35, 38, 39, 91, 92).

[4] A. Urban, D.-H. Seo, and G. Ceder, NJP Comput. Mater. **2**, 16002 (2016) (cit. on pp. iii, v, 2, 91).

[5] S. Kirklin, B. Meredig, and C. Wolverton, Adv. Energy Mater. **3**, 252 (2013) (cit. on pp. iii, v, 2, 91).

[6] R. Muller and P. Schultz, Modelling Simul. Mater. Sci. Eng. **21**, 070301 (2012) (cit. on pp. iii, v, 2, 91).

[7] Y. Wang, W. Richards, S. Ong, L. Miara, J. Kim, Y. Mo, and G. Ceder, Nat. Mater. **14**, 1026 (2015) (cit. on pp. iii, v, 2, 35, 91).

[8] G. Hautier, AIP Conference Proceedings **1765**, 020009 (2016) (cit. on pp. iii, v, 2, 91).

[9] A. Van der Ven, J. Bhattacharya, and A. A. Belak, Accounts Chem. Res. **46**, 1216 (2013) (cit. on pp. iii, v, 1, 2, 34, 35, 38, 43, 44, 54, 58, 61, 92).

[10] A. Urban, J. Lee, and G. Ceder, Adv. Energy Mater. **4**, 1400478 (2014) (cit. on pp. iii, v, 43, 44).

[11] B. Ziebarth, M. Klinsmann, T. Eckl, and C. Elsaesser, Phys. Rev. B: Condens. Matter Mater. Phys. **89**, 174301 (2014) (cit. on pp. v, 43, 44, 48, 51, 54, 57, 58).

[12] V. Weber, T. Laino, A. Curioni, T. Eckl, C. Engel, J. Kasemchainan, and N. Salingue, J. Phys. Chem. C **119**, 9681 (2015) (cit. on pp. v, 43, 44, 54, 58).

[13] R. Levy, *Microelectronic materials and processes*, 1st (Kluwer Academic, Dordrecht, 1989) (cit. on p. 1).

[14] J. Choi, X. Yang, Z. Norman, S. Billinge, and J. Owen, Nano Lett. **14**, 127 (2014) (cit. on p. 1).

[15] W. Callister, *Materials science and engineering: an introduction*, 7th (John Wiley & Sons, New York, 2007) (cit. on p. 1).

[16] H. Mehrer, in *Diffusion in solids* (Springer, 2007) (cit. on pp. 1, 30, 31, 33, 35–38, 43, 44, 55, 57, 61, 80, 91, 92).

[17] B. Scrosati and J. Garche, J. Power Sources **195**, 2419 (2010) (cit. on p. 1).

[18] M. V. Reddy, G. V. Subba Rao, and B. V. R. Chowdari, Chem. Rev. **113**, 5364 (2013) (cit. on pp. 1, 43, 51).

[19] N. Nitta, F. Wu, J. Lee, and G. Yushin, Mater. Today **18**, 252 (2015) (cit. on p. 1).

[20] H. Buschmann, J. Dölle, S. Berendts, A. Kuhn, P. Bottke, M. Wilkening, P. Heitjans, A. Senyshyn, H. Ehrenberg, A. Lotnyk, V. Duppel, L. Kienle, and J. Janek, Phys. Chem. Chem. Phys. **13**, 19378 (2011) (cit. on p. 1).

[21] O. Bohnke, Solid State Ion. **179**, 9 (2008) (cit. on p. 1).

[22] A. C. Luntz, J. Voss, and K. Reuter, J. Phys. Chem. Lett. **6**, 4599 (2015) (cit. on pp. 1, 38, 86).

[23] I.-H. Iek-Heng Chu, H. Nguyen, S. Hy, Y.-C. Lin, Z. Wang, Z. Xu, Z. Deng, Y. Meng, and S. Ong, Appl. Mater. Interfaces **8**, 7843 (2016) (cit. on p. 1).

[24] M. S. Islam and C. A. J. Fisher, Chem. Soc. Rev. **43**, 185 (2014) (cit. on pp. 2, 9, 38, 39, 66, 91, 92).

[25] N. G. Hörmann, M. Jäckle, F. Gossenberger, T. Roman, K. Forster-Tonigold, M. Naderian, S. Sakong, and A. Groß, J. Power Sources **275**, 531 (2015) (cit. on pp. 2, 43, 92).

[26] B. Kozinsky, S. Akhade, P. Hirel, A. Hashibon, C. Elsässer, P. Mehta, A. Logeat, and U. Eisele, Phys. Rev. Lett. **116**, 055901 (2016) (cit. on pp. 2, 38, 91).

[27] F. Jensen, *Introduction of Computational Chemistry*, second (John Wiley & Sons, Chichester, 2007) (cit. on pp. 2, 5, 7, 8, 19, 71).

[28] M. Allen and D. Tildesley, in *Computer simulations of liquids* (Akademic Press, 1987) (cit. on pp. 2, 12–16, 19, 30, 31, 41, 42, 65).

[29] D. Frenkel and B. Smit, in *Understanding molecular simulation: from algorithms to applications* (Akademic Press, 1996) (cit. on pp. 2, 8, 11–15, 27, 28, 30, 31, 33, 41, 51, 57).

[30] W. J. Hehre, *A Guide to Molecular Mechanics and Quantum Chemical Calculations* (Wavefunction, Inc., 2003) (cit. on p. 2).

[31] C. J. Cramer, *Essentials of Computational Chemistry*, second (John Wiley & Sons, 2004) (cit. on pp. 2, 5, 7, 8).

[32] J. Bhattacharya and A. Van der Ven, Phys. Rev. B: Condens. Matter Mater. Phys. **81**, 104304 (2010) (cit. on pp. 2, 44).

[33] V. Diwakar, S. Harinipriya, and V. Subramanian, in *Theory and experiment in electrocatalysis* (Springer, 2010), pp. 315–349 (cit. on p. 3).

[34] S. J. Plimpton and A. P. Thompson, MRS Bulletin **37**, 513 (2012) (cit. on pp. 3, 7, 8, 66).

[35] A. Szabo and N. Ostlund, *Modern Quantum Chemistry: Introduction to Advanced Electronic Structure Theory*, first (Dover Publications, Mineola, 1989) (cit. on pp. 5–7).

[36] P. Hohenberg and W. Kohn, Phys. Rev. **136**, B864 (1964) (cit. on p. 6).

[37] A. Becke, J. Phys. Chem. **140**, 18A301 (2014) (cit. on p. 7).

[38] J. Hill, C. Freeman, and L. Subramanian, in *Reviews in computational chemistry* (Wiley-VCH, Inc., 2007) (cit. on pp. 8, 9, 19, 38, 67).

[39] M. Born and K. Huang, in *Dynamical theory of crystal lattices* (Oxford University Press, Oxford, UK, 1954) (cit. on pp. 8, 45, 66, 67, 72).

[40] M. Daw and M. Baskes, Phys. Rev. Lett. **50**, 1285 (1983) (cit. on p. 8).

[41] M. Daw and M. Baskes, Phys. Rev. B **29**, 6443 (1984) (cit. on p. 8).

[42] M. Baskes, Phys. Rev. Lett. **59**, 2666 (1987) (cit. on p. 8).

[43] J. Tersoff, Phys. Rev. B **37**, 6991 (1988) (cit. on p. 8).

[44] D. Pettifor and I. Oleinik, Phys. Rev. B **59**, 8487 (1999) (cit. on p. 8).

[45] A. van Duin, S. Dasgupta, F. Lorant, and W. Goddard, J. Phys. Chem. A **105**, 9396 (2001) (cit. on p. 8).

[46] J. Yu, S. Sinnott, and S. Phillpot, Phys. Rev. B **75**, 085311 (2007) (cit. on p. 8).

[47] A. Toukmaji and J. Board, Comput. Phys. Commun. **95**, 73 (1996) (cit. on p. 8).

[48] E. Pollock and J. Glosli, Comput. Phys. Commun. **95**, 93 (1996) (cit. on p. 8).

[49] C. Catlow, *Computer modelling in inorganic crystallography* (Academic Press, San Diego, 1997) (cit. on p. 9).

[50] A. Sokol and C. Catlow, *Computational methods for energy materials* (John Wiley & Sons, Ltd, 2013) (cit. on p. 9).

[51] B. Szigeti, Proc. Roy. Soc. **204**, 51 (1950) (cit. on p. 9).

[52] C. Catlow and W. Mackrodt, *Computer simulation of solids* (Springer, 1982) (cit. on pp. 9, 10, 19, 25, 66, 69).

[53] P. J. Mitchell and D. Fincham, J. Phys: Condens. Matter **5**, 1031 (1993) (cit. on pp. 9, 15, 16, 47, 65).

[54] B. Dick and W. Overhauser, Phys. Rev. **112**, 90 (1958) (cit. on pp. 9, 10).

[55] R. Sternheimer, Phys. Rev. **96**, 951 (1954) (cit. on p. 9).

[56] R. Sternheimer, Phys. Rev. **107**, 1565 (1957) (cit. on p. 9).

[57] G. Bussi, D. Donadio, and M. Parrinello, J. Chem. Phys. **126**, 014101 (2007) (cit. on p. 11).

[58] S. Plimpton, App. Math. Sci. **117**, 1 (1995) (cit. on pp. 12, 14, 17, 21, 45, 65).

[59] P. Lindan and M. Gillan, J. Phys: Condens. Matter **5**, 1019 (1993) (cit. on pp. 15, 16).

[60] W. Smith, C. Yong, and P. Rodger, Mol. Simulat. **28**, 385 (2002) (cit. on p. 16).

[61] J. Gale and A. Rohl, Mol. Simulat. **29**, 291 (2003) (cit. on pp. 16, 39).

[62] D. Fincham, W. Mackrodt, and P. Mitchell, J. Phys: Condens. Matter **6**, 393 (1994) (cit. on p. 17).

[63] J. Gale, Philos. Mag. B **73**, 3 (1996) (cit. on pp. 19, 25).

[64] P. Brommer, A. Kiselev, D. Schopf, P. Beck, J. Roth, and H.-R. Trebin, Modelling Simul. Mater. Sci. Eng. **23**, 074002 (2015) (cit. on pp. 19, 20, 22).

[65] P. Tangney and S. Scandolo, J. Chem. Phys. **117**, 8898 (2002) (cit. on pp. 20, 21, 66, 67).

[66] A. H. Larsen, J. J. Mortensen, J. Blomqvist, I. E. Castelli, R. Christensen, M. Dułak, J. Friis, M. N. Groves, B. Hammer, C. Hargus, E. D. Hermes, P. C. Jennings, P. B. Jensen, J. Kermode, J. R. Kitchin, E. L. Kolsbjerg, J. Kubal, K. Kaasbjerg, S. Lysgaard, J. B. Maronsson, T. Maxson, T. Olsen, L. Pastewka, A. Peterson, C. Rostgaard, J. Schiøtz, O. Schütt, M. Strange, K. S. Thygesen, T. Vegge, L. Vilhelmsen, M. Walter, Z. Zeng, and K. W. Jacobsen, J. Phys: Condens. Matter **29**, 273002 (2017) (cit. on pp. 21, 45, 65).

[67] R. Storn and K. Price, J. Glob. Optim. **11**, 341 (1997) (cit. on p. 22).

[68] S. Kerisit, N. A. Deskins, K. M. Rosso, and M. Dupuis, J. Phys. Chem. C **112**, 7678 (2008) (cit. on pp. 22, 25, 48, 92).

[69] A. Garrett, *Inspyred: bio-inspired algorithms in python*, version 1.0 (cit. on pp. 22, 65).

[70] J. Kennedy and R. Eberhart, Proc. IEEE International Conf. on Neural Networks **1**, 1942 (1995) (cit. on pp. 22, 23).

[71] E. Jones, T. Oliphant, and P. Peterson, *SciPy: open source scientific tools for Python*, version 0.19.1 (cit. on pp. 22, 65).

[72] R. Hassan, C. B., O. de Weck, and G. Venter, 46th AIAA/ASME/ASCE/AHS/ASC Structures, Structural Dynamics and Materials Conference **2**, 1 (2015) (cit. on pp. 23, 24).

[73] S. Wengert, "Validation of a Polarizable Atomistic Force Field for the Solid State Ion Conductor LATP," Master thesis (Technische Universität München, 2018) (cit. on p. 23).

[74] M. Sangster, G. Peckham, and D. Saunderson, J. Phys. C: Solid State Phys. **3**, 1026 (1970) (cit. on p. 25).

[75] F. Holka, M. Urban, P. Neogrády, and J. Paldus, J. Chem. Phys. **141**, 214303 (2014) (cit. on pp. 25, 71).

[76] R. Mouta, M. Melo, E. Diniz, and C. Paschoal, Chem. Mater. **26**, 7137 (2014) (cit. on pp. 25, 66–69, 72, 73).

[77] D. Frenkel, in *Introduction to Monte-Carlo methods*, Vol. 23 (John von Neumann Institute for Computing, Jülich, NIC Series, 2004), pp. 29–60 (cit. on pp. 26, 27).

[78] L. Reichl, *A Modern Course in Statistical Physics*, 2nd (John Wiley & Sons, 2004) (cit. on p. 26).

[79] N. Metropolis, A. Rosenbluth, M. Rosenbluth, A. Teller, and E. Teller, J. Chem. Phys. **21**, 1087 (1953) (cit. on p. 26).

[80] D. Earl and M. Deem, Phys. Chem. Chem. Phys. **7**, 3910 (2005) (cit. on pp. 27, 28).

[81] A. Malakis and T. Papakonstantinou, Phys. Rev. E: Stat. Phys., Plasmas, Fluids, Relat. Interdiscip. Top. **88**, 013312 (2013) (cit. on p. 27).

[82] F. Wang and D. Landau, Phys. Rev. E: Stat. Phys., Plasmas, Fluids, Relat. Interdiscip. Top. **64**, 056101 (2001) (cit. on pp. 28, 29, 46, 51).

[83] B. Schulz, K. Binder, M. Mueller, and D. Landau, Phys. Rev. E: Stat. Phys., Plasmas, Fluids, Relat. Interdiscip. Top. **67**, 067102 (2003) (cit. on pp. 28, 29, 46, 51).

[84] D. Landau, S.-H. Tsai, and M. Exler, Am. J. Phys. **72**, 1294 (2004) (cit. on pp. 28, 29, 46, 51).

[85] R. Belardinelli and V. Pereyry, Phys. Rev. E: Stat. Phys., Plasmas, Fluids, Relat. Interdiscip. Top. **75**, 046701 (2007) (cit. on pp. 28, 29, 46, 51).

[86] D. Landau and K. Binder, *A Guide to Monte Carlo Simulations in Statistical Physics*, 3rd (Cambridge University Press, 2009) (cit. on p. 28).

[87] T. Vogel, Y. Li, T. Wuest, and D. Landau, Phys. Rev. Lett. **110**, 210603 (2013) (cit. on pp. 28, 29, 51).

[88] R. Belardinelli and V. Pereyry, Phys. Rev. E: Stat. Phys., Plasmas, Fluids, Relat. Interdiscip. Top. **93**, 053306 (2016) (cit. on pp. 28, 29, 46, 51).

[89] A. Tröster and C. Dellago, Phys. Rev. E: Stat. Phys., Plasmas, Fluids, Relat. Interdiscip. Top. **71**, 066705 (2005) (cit. on p. 29).

[90] H. Flyvbjerg and H. Petersen, J. Chem. Phys. **91**, 461 (1989) (cit. on pp. 31, 80).

[91] G. Murch, Solid State Ion. **7**, 177 (1982) (cit. on pp. 31, 37, 80, 84).

[92] A. Kinaci, J. Haskins, and T. Çağin, J. Chem. Phys. **137**, 014106 (2012) (cit. on pp. 32, 41, 79).

[93] J. Kärger, D. M. Ruthven, and D. N. Theodorou, *Diffusion in nanoporous materials* (Wiley-VCH, 2012) (cit. on pp. 32, 57, 58).

[94] M. Kowsari, S. Alavi, B. Najafi, K. Gholizadeh, E. Dehghanpishehd, and F. Ranjbar, Phys. Chem. Chem. Phys. **13**, 8826 (2011) (cit. on pp. 33, 34).

[95] A. Marcolongo and N. Marzari, Phys. Rev. Materials **1**, 025402 (2017) (cit. on pp. 33, 34).

[96] J. Haskins, W. Bennett, J. Wu, D. Hernańdez, O. Borodin, J. Monk, C. Bauschlicher Jr., and J. Lawson, J. Chem. Phys. B **118**, 11295 (2014) (cit. on pp. 33, 38, 83–85, 88).

[97] D. Stein and F. Spera, Am. Mineral. **80**, 417 (1995) (cit. on p. 34).

[98] G. Henkelman, B. P. Uberuaga, and H. Jónsson, J. Chem. Phys. **113**, 9901 (2000) (cit. on p. 35).

[99] G. Henkelman and H. Jónsson, J. Chem. Phys. **113**, 9978 (2000) (cit. on p. 35).

[100] C. Schuette, F. Noe, J. Lu, M. Sarich, and E. Vanden-Eijnden, J. Chem. Phys. **19**, 134 (2011) (cit. on pp. 35, 47).

[101] M. Sarich, R. Banisch, C. Hartmann, and C. Schuette, ZIB-Report, 0 (2013) (cit. on pp. 35, 47).

[102] M. Vogel, Phys. Rev. B: Condens. Matter Mater. Phys. **70**, 094302 (2004) (cit. on p. 35).

[103] N. J. J. de Klerk and M. Wagemaker, Chem. Mater. **28**, 3122 (2016) (cit. on p. 35).

[104] J. Isard, J. Non-Cryst. Solids **246**, 16026 (1999) (cit. on pp. 36–38, 63, 80, 84, 92).

[105] G. Murch and R. Thorn, Philos. Mag. **39**, 673 (1979) (cit. on p. 37).

[106] F. T., M. Kunze, M. Schönhoff, J. Sundermeyer, and B. Roling, J. Phys. Chem. B **112**, 12985 (2008) (cit. on pp. 38, 84).

[107] M. Islam, D. Driscoll, C. Fisher, and P. Slater, Chem. Mater. **17**, 5085 (2005) (cit. on p. 38).

[108] R. Malik, D. Burch, M. Bazant, and G. Ceder, Nano Lett. **10**, 4123 (2010) (cit. on p. 38).

[109] S. Adams and R. Rao, Solid State Ion. **184**, 57 (2011) (cit. on p. 38).

[110] C. Tealdi, C. Spreafico, and P. Mustarelli, J. Mater. Chem. **22**, 24870 (2012) (cit. on p. 38).

[111] X. He, Y. Zhu, and Y. Mo, Nat. Commun. **8**, 15893 (2017) (cit. on pp. 38, 61).

[112] Y. Zhu, X. He, and Y. Mo, ACS Appl. Mater. Interfaces **7**, 23685 (2015) (cit. on p. 38).

[113] N. Mott and M. Littleton, Trans. Faraday Soc. **34**, 485 (1938) (cit. on p. 38).

[114] A. Lidiard, J. Chem. Soc., Faraday Trans. 2 **85**, 341 (1989) (cit. on p. 38).

[115] J. Harding, J. Chem. Soc., Faraday Trans. 2 **85**, 351 (1989) (cit. on p. 39).

[116] C. Catlow, J. Chem. Soc., Faraday Trans. 2 **85**, 335 (1989) (cit. on p. 39).

[117] J. Maier and R. Amin, J. Electrochem. Soc. **155**, A339 (2008) (cit. on p. 39).

[118] G. Gardiner and M. Islam, Chem. Mater. **22**, 1242 (2010) (cit. on p. 39).

[119] C. Angell, K. Ngai, G. McKenna, P. McMillan, and S. Martin, J. Appl. Phys. **88**, 3113 (2000) (cit. on pp. 40, 66, 75, 80).

[120] P. Debenedetti and F. Stillinger, Nature **410**, 259 (2001) (cit. on pp. 40, 66, 75, 76).

[121] F. Stillinger and P. Debenedetti, Annu. Rev. Condens. Matter Phys. **4**, 263 (2013) (cit. on pp. 40, 66, 75, 77, 82).

[122] P. Daivis and B. Todd, J. Chem. Phys. **124**, 194103 (2006) (cit. on p. 41).

[123] P. C. Tsai, W. D. Hsu, and S. K. Lin, J. Electrochem. Soc. **161**, A439 (2014) (cit. on pp. 43, 44, 51).

[124] L. Kavan, J. Procházka, T. M. Spitler, M. Kalbáč, M. Zukalová, T. Drezen, and M. Grätzel, J. Electrochem. Soc. **150**, A1000 (2003) (cit. on p. 43).

[125] W. J. H. Borghols, M. Wagemaker, U. Lafont, E. M. Kelder, and F. M. Mulder, J. Am. Chem. Soc. **131**, 17786 (2009) (cit. on p. 43).

[126] Y. Shi, L. Wen, F. Li, and H.-M. Cheng, J. Power Sources **196**, 8610 (2011) (cit. on p. 43).

[127] J. M. Feckl, K. Fominykh, M. Doeblinger, D. Fattakhova-Rohlfing, and T. Bein, Angew. Chem. **51**, 7459 (2012) (cit. on pp. 43, 51).

[128] M. Park, X. Zhang, M. Chung, G. B. Less, and A. M. Sastry, J. Power Sources **195**, 7904 (2010) (cit. on p. 43).

[129] W. Schmidt, P. Bottke, M. Stemad, P. Gollob, V. Hennige, and M. Wilkening, Chem. Mater. **27**, 1740 (2015) (cit. on pp. 43, 55, 59, 60, 91).

[130] W. Schmidt and M. Wilkening, J. Phys. Chem. C **120**, 11372 (2016) (cit. on pp. 43, 55, 59, 60, 91).

[131] D. Young, A. Ransil, R. Amin, Z. Li, and Y.-M. Chiang, Adv. Energy Mater. **3**, 1125 (2013) (cit. on p. 44).

[132] M. Kitta, T. Akita, S. Tanaka, and M. Kohyama, J. Power Sources **257**, 120 (2014) (cit. on pp. 44, 59, 60).

[133] M. Wagemaker, D. R. Simon, E. M. Kelder, J. Schoonman, C. Ringpfeil, U. Haake, D. Luetzenkirchen-Hecht, R. Frahm, and F. M. Mulder, Adv. Mater. **18**, 3169 (2006) (cit. on pp. 44, 55, 58, 59).

[134] M. Wagemaker, E. van Eck, A. Kentgens, and F. Mulder, J. Phys. Chem. B **113**, 224 (2008) (cit. on p. 44).

[135] S. Ganapathy, A. Vasileiadis, J. R. Heringa, and W. Marnix, Adv. Energy Mater. **7**, 1601781 (2017) (cit. on pp. 44, 58–60).

[136] C. Kim, N. S. Norberg, C. T. Alexander, R. Kostecki, and J. Cabana, Adv. Funct. Mater. **23**, 1214 (2013) (cit. on pp. 44, 60).

[137] M. G. Verde, L. Baggetto, N. Balke, G. M. Veith, J. K. Seo, Z. Wang, and Y. S. Meng, ACS Nano **10**, 4312 (2016) (cit. on pp. 44, 60, 91).

[138] K. Kataoka, Y. Takahashi, N. Kijima, J. Akimoto, and K.-i. Ohshima, J. Phys. Chem. Solids **69**, 1454 (2008) (cit. on pp. 44, 48).

[139] Z. Yang, D. Choi, S. Kerisit, K. M. Rosso, D. Wang, J. Zhang, G. Graff, and J. Liu, J. Power Sources **192**, 588 (2009) (cit. on p. 44).

[140] S. Zahn, J. Janek, and D. Mollenhauer, J. Electrochem. Soc. **164**, A221 (2017) (cit. on pp. 44, 51).

[141] M. Vijayakumar, S. Kerisit, K. M. Rosso, S. D. Burton, J. A. Sears, Z. Yang, G. L. Graff, J. Liu, and J. Hu, J. Power Sources **196**, 2211 (2011) (cit. on pp. 44, 45, 47, 48, 51, 57, 58).

[142] C. Pecharromán and J. Amarilla, Phys. Rev. B: Condens. Matter Mater. Phys. **62**, 12062 (2000) (cit. on pp. 44, 57, 58).

[143] I. Leonidov, O. Leonidova, L. Perelyaeva, R. Samigullina, S. Kovyazina, and M. Patrakeev, Phys. Solid State **45**, 2183 (2003) (cit. on pp. 44, 57, 58, 60).

[144] V. Blum, R. Gehrke, F. Hanke, P. Havu, V. Havu, X. Ren, K. Reuter, and M. Scheffler, Comp. Phys. Commun. **180**, 2175 (2009) (cit. on p. 45).

[145] H. Monkhorst and J. Pack, Phys. Rev. B: Condens. Matter. **13**, 5188 (1976) (cit. on pp. 45, 65).

[146] R. W. Hockney and J. W. Eastwood, *Computer simulation using particles* (CRC Press, 1988) (cit. on pp. 45, 65).

[147] K. Momma and F. Izumi, J. Appl. Crystallogr. **44**, 1272 (2011) (cit. on pp. 45, 65).

[148] M. E. Tuckerman, J. Alejandre, R. Lopez-Rendon, A. L. Jochim, and G. J. Martyna, J. Phys. A: Math. Gen. **39**, 5629 (2006) (cit. on pp. 47, 65).

[149] W. Shinoda, M. Shiga, and M. Mikami, Phys. Rev. B: Condens. Matter Mater. Phys. **69**, 134103 (2004) (cit. on pp. 47, 65).

[150] M. Matsui and M. Akaogi, Mol. Simul. **6**, 239 (1991) (cit. on p. 48).

[151] S. Kerisit, K. M. Rosso, Z. Yang, and J. Liu, J. Phys. Chem. C **113**, 20998 (2009) (cit. on pp. 48, 54, 92).

[152] M. Vijayakumar, S. Kerisit, Z. Yang, G. L. Graff, J. Liu, J. A. Sears, S. D. Burton, K. M. Rosso, and J. Hu, J. Phys. Chem. C **113**, 20108 (2009) (cit. on p. 48).

[153] S. Kerisit, K. M. Rosso, Z. Yang, and J. Liu, J. Phys. Chem. C **114**, 19096 (2010) (cit. on p. 48).

[154] T. Ohzuku, A. Ueda, and N. Yamamoto, J. Electrochem. Soc. **142**, 1431 (1995) (cit. on pp. 51, 54).

[155] Y. Tang, L. Yang, Z. Qiu, and J. Huang, J. Mater. Chem. **19**, 5980 (2009) (cit. on p. 51).

[156] H. Shiiba, M. Nakayama, and M. Nogami, Solid State Ion. **181**, 994 (2010) (cit. on p. 51).

[157] D. Shao, J. He, Y. Luo, W. Liu, X. Yu, and Y. Fang, J. Solid State Electrochem. **16**, 2047 (2012) (cit. on p. 51).

[158] Y. Sun, L. Zhao, H. Pan, X. Lu, L. Gu, Y.-S. Hu, H. Li, M. Armand, Y. Ikuhara, L. Chen, and X. Huang, Nat. Commun., 2878 (2013) (cit. on p. 51).

[159] D. C. Johnston, J. Low Temp. Phys. **25**, 145 (1976) (cit. on p. 54).

[160] M. Wilkening, R. Amade, W. Iwaniak, and P. Heitjans, Phys. Chem. Chem. Phys. **9**, 1239 (2007) (cit. on pp. 54, 55, 58, 60).

[161] Y. Wang, L. Gu, Y. Guo, H. Li, X. He, S. Tsukimoto, Y. Ikuhara, and L. Wan, J. Am. Chem. Soc. **134**, 7874 (2012) (cit. on p. 58).

[162] M. F. Graf, H. Tempel, S. S. Köcher, R. Schierholz, C. Scheurer, H. Kungl, R.-A. Eichel, and J. Granwehr, RSC Adv. **7**, 25276 (2017) (cit. on p. 59).

[163] J. Kawamura, R. Asayama, N. Kuwata, and O. Kamishima, in *Phys. solid state ionics* (Research Signpost, 2006) (cit. on pp. 63, 80, 92).

[164] A. Chandra, A. Bhatt, and A. Chandra, J. Mater. Sci. Technol. **29**, 193 (2013) (cit. on pp. 63, 75, 80, 92).

[165] Y. Tu, J. Tersoff, G. Grinstein, and D. Vanderbilt, Phys. Rev. Lett. **81**, 4899 (1998) (cit. on p. 63).

[166] M. Braga, J. Ferreira, V. Stockhausen, J. Oliveirad, and A. El-Azab, J. Mater. Chem. A **2**, 5470 (2014) (cit. on pp. 63, 64, 66, 67, 72, 73, 75, 76, 82–84, 86, 88, 89, 91, 92).

[167] L. Valøena and J. Reimers, J. Electrochem. Soc. **152**, A882 (2005) (cit. on p. 63).

[168] R. Kumar, B. Singh, and S. Sekhon, J. Mater. Sci. **40**, 1273 (2005) (cit. on p. 63).

[169] Q. Li, J. Chen, L. Fan, X. Kong, and Y. Lu, Green Energy & Environment **1**, 18 (2016) (cit. on p. 63).

[170] E. Logan, E. Tonita, K. Gering, J. Li, X. Ma, L. Beaulieu, and J. Dahn, J. Electrochem. Soc. **165**, A21 (2018) (cit. on p. 63).

[171] N. Kamaya, K. Homma, Y. Yamakawa, M. Hirayama, R. Kanno, and M. Yonemura, Nat. Mater. **10**, 682 (2011) (cit. on p. 63).

[172] M. Braga, N. Grundish, A. Murchison, and J. Goodenough, Energy Environ. Sci. **10**, 331 (2016) (cit. on pp. 63, 64, 86, 89, 91).

[173] D. Steingart and V. Viswanathan, Energy Environ. Sci. **11**, 221 (2017) (cit. on p. 63).

[174] M. Braga, A. Murchison, J. Ferreira, P. Singh, and J. Goodenough, Energy Environ. Sci. **9**, 948 (2016) (cit. on pp. 63, 64, 89, 91).

[175] M. Braga, J. Ferreira, A. Murchison, and J. Goodenough, J. Electrochem. Soc. **164**, A207 (2017) (cit. on pp. 63, 64).

[176] J. Zhang, J. Han, J. Zhu, Z. Lin, M. Braga, L. Daemen, W. L., and Y. Zhao, Inorg. Chem. Commun. **48**, 140 (2014) (cit. on p. 64).

[177] O. Reckeweg, B. Blaschkowski, and T. Schleid, Z. Anorg. Allg. Chem. **638**, 2081 (2012) (cit. on pp. 64, 67).

[178] A.-Y. Song, Y. Xiao, K. Turcheniuk, P. Upadhya, A. Ramanujapuram, J. Benson, A. Magasinski, M. Olguin, L. Meda, O. Borodin, and G. Yushin, Adv. Energy Mater. **8**, 1700971 (2017) (cit. on p. 64).

[179] A. Emly, E. Kioupakis, and A. Van der Ven, Chem. Mater. **25**, 4663 (2013) (cit. on pp. 64, 67, 72, 73).

[180] M.-H. Chen, A. Emly, and A. Van der Ven, Phys. Rev. B: Condens. Matter Mater. Phys. **91**, 214306 (2015) (cit. on p. 64).

[181] G. Kresse and J. Furthmüller, Phys. Rev. B: Condens. Matter Mater. Phys. **54**, 11169 (1996) (cit. on p. 65).

[182] G. Kresse and J. Furthmüller, Comput. Mater. Sci. **6**, 15 (1996) (cit. on p. 65).

[183] P. Blöchl, Phys. Rev. B: Condens. Matter Mater. Phys. **50**, 17953 (1994) (cit. on p. 65).

[184] J. Perdew, A. Ruzsinszky, G. Csonka, O. Vydrov, G. Scuseria, L. Constantin, X. Zhou, and K. Burke, Phys. Rev. Lett. **100**, 136406 (2008) (cit. on p. 65).

[185] J. Perdew, A. Ruzsinszky, G. Csonka, O. Vydrov, G. Scuseria, L. Constantin, X. Zhou, and K. Burke, Phys. Rev. Lett. **102**, 039902 (2009) (cit. on p. 65).

[186] S. Nosé, J. Chem. Phys. **81**, 511 (1984) (cit. on p. 65).

[187] S. Nosé, Prog. Theor. Phys. Suppl. **103**, 1 (1991) (cit. on p. 65).

[188] D. Bylander and L. Kleinman, Phys. Rev. B: Condens. Matter Mater. Phys. **46**, 13756 (1992) (cit. on p. 65).

[189] J. Kubicki and A. Lasaga, Phys. Chem. Minerals **17**, 661 (1991) (cit. on pp. 66, 77).

[190] M. Utz, P. Debenedetti, and F. Stillinger, Phys. Rev. Lett. **84**, 1471 (2000) (cit. on p. 66).

[191] A. Cormack, J. Du, and T. Zeitler, Phys. Chem. Chem. Phys. **4**, 3193 (2002) (cit. on pp. 66, 76).

[192] J. Du and A. Cormack, J. Am. Ceram. Soc. **88**, 2532 (2005) (cit. on pp. 66, 76).

[193] G. Broglia, G. Ori, L. Larcher, and M. Montorsi, Modelling Simul. Mater. Sci. Eng. **22**, 065006 (2014) (cit. on pp. 66, 76).

[194] P. Vashishta, R. Kalia, A. Nakano, and J. Rino, J. Appl. Phys. **103**, 083504 (2008) (cit. on p. 66).

[195] W. Haynes, *CRC Handbook of Chemistry and Physics*, 92nd (CRC Press., 2011) (cit. on p. 66).

[196] Z. Lu, C. Chen, Z. Baiyee, X. Chen, C. Niub, and F. Ciucci, Phys. Chem. Chem. Phys **17**, 32547 (2015) (cit. on p. 72).

[197] Y. Zhang, Y. Zhao, and C. Chen, Phys. Rev. B: Condens. Matter Mater. Phys. **87**, 134303 (2013) (cit. on p. 72).

[198] Z. Deng, B. Radhakrishnan, and S. Ong, Chem. Mater. **27**, 3749 (2015) (cit. on p. 72).

[199] S. Longbottom and P. Brommer, *Uncertainty quantification for classical effective potentials*, DPG Spring Meeting, 2018 (cit. on p. 75).

[200] M. Ediger, C. Angell, and S. Nagel, J. Phys. Chem. **100**, 13200 (1996) (cit. on pp. 75, 77).

[201] H. Yu, W. Wang, H. Bai, and K. Samwer, Natl. Sci. Rev. **1**, 429 (2014) (cit. on pp. 75, 80, 82, 84).

[202] F. Stillinger, Science **267**, 1935 (1995) (cit. on pp. 75, 82).

[203] E. La Nave, F. Sciortino, P. Tartaglia, C. De Michele, and S. Mossa, J. Phys: Condens. Matter **15**, S1085 (2003) (cit. on p. 75).

[204] M. Benoit, S. Ispas, P. Jund, and R. Jullien, Eur. Phys. J. B **13**, 631 (2000) (cit. on p. 76).

[205] S. Ispas, M. Benoit, P. Jund, and R. Jullien, Phys. Rev. B. **64**, 214206 (2001) (cit. on p. 76).

[206] X. Lei, Y. Jeeb, and K. Huang, J. Mater. Chem. A **3**, 19920 (2015) (cit. on p. 76).

[207] T. Baba and Y. Kawamura, Front. Energy Res. **4**, 22 (2016) (cit. on p. 76).

[208] K. Kerman, A. Luntz, V. Viswanathan, Y.-M. Chiang, and Z. Chen, J. Electrochem. Soc. **164**, A1731 (2017) (cit. on p. 79).

[209] B. Scrosati, A. Magistris, C. Mari, and G. Mariotto, in *Fast ion transport in solids* (Springer Netherlands, 1993) (cit. on p. 80).

[210] P. Atkins and J. de Paula, *Physical Chemistry*, 8th (Oxford University Press, 2006) (cit. on p. 85).

[211] J. Newman and K. Thomas-Alyea, *Electrochemical systems*, 3rd (Wiley-Interscience, 2004) (cit. on p. 86).

[212] R. O'Hayre and C. Suk-Won, *Fuel cell fundamentals*, 2nd (Wiley, 2009) (cit. on p. 86).

[213] M. Tatsumisago and A. Hayashi, Int. J. Appl. Glass Sci. **5**, 226 (2014) (cit. on p. 88).

[214] T. Tsujimura, Solid State Ion. **262**, 829 (2014) (cit. on p. 88).

[215] A. Hayashi, K. Noi, A. Sakuda, and M. Tatsumisago, Nat. Commun. **3**, 856 (2012) (cit. on p. 88).

[216] X. Zhou and F. Doty, Phys. Rev. B **78**, 224307 (2008) (cit. on p. 92).

[217] X. Zhou, F. Doty, and P. Yang, Comput. Mater. Sci. **50**, 2470 (2011) (cit. on p. 92).

[218] X. Zhou, H. Wadley, J.-S. Filhol, and M. Neurock, Phys. Rev. B **69**, 035402 (2004) (cit. on p. 92).

[219] X. Zhou and H. Wadley, J. Phys. Condens. Matter **17**, 3619 (2005) (cit. on p. 92).

[220] E. Lee, K.-R. Lee, M. Baskes, and B.-J. Lee, Phys. Rev. B **93**, 144110 (2016) (cit. on p. 92).

Appendices

A Force field potential parameters for glass-amorphous Li_3OCl

Tab. 1.1: Pair potential parameters for the description of glass-amorphous Li_3OCl as obtained via the parameterization procedure described in Sec. 5.3.1 at a cutoff of 12 Å and the usage of a PPPM long-range solver for the reciprocal part of the Coulomb interactions.

ion pair (ij)	A_{ij} / eV	ρ_{ij} / Å	C_{ij} / eV · Å^6
Li-Li	15594.1325	0.0832	0.0000
Li-O	982.9501	0.2472	0.0000
Li-Cl	441.6885	0.3083	0.0000
O-O	6415.7122	0.2460	89.5308
O-Cl	25817.1797	0.2540	140.2019
Cl-C	30193.5880	0.2636	82.0073

Tab. 1.2: Partial charges q_{ion} and core/shell parameters q_{shell} and k_{cs} for the description of glass-amorphous Li_3OCl as obtained via the parameterization procedure described in Sec. 5.3.1 at a cutoff of 12 Å and the usage of a PPPM long-range solver for the reciprocal part of the Coulomb interactions.

i	q_{ion} / e	q_{shell} / e	k_{cs} / eV Å^{-2}
Li^+	0.743569	0.000	0.0000
O^{2-}	−1.487138	−2.183	82.6440
Cl^-	−0.743569	−2.535	43.4797

B Steady state charge polarization in a one dimensional dilute binary electrolyte

The influence of an electric field on ions in a solution induces directed migration. The resulting transport can be described by the Nernst-Planck equation. Hereby, the time dependency of the ion flux F_i of species i as the change in its concentration c_i [1]

$$\frac{\partial c_i}{\partial t} = -\nabla F_i \tag{B.1}$$

results in

$$\frac{\partial c_i}{\partial t} = \nabla \left[D_i \nabla c_i - u c_i + \frac{D_i z_i e}{\mathrm{k_B} T} c_i \left(\nabla \Phi + \frac{\partial A}{\partial t} \right) \right] \tag{B.2}$$

where D_i and z_i are the Diffusion coefficient and charge of species i, e is the elementary charge, $\mathrm{k_B}$ the Boltzmann constant, T the temperature, $\nabla \Phi = -E$ the change in potential corresponding to the negative of the electric field and A the magnetic vector potential accounting for electrostatic correlation. Equation B.2 includes a terms accounting for diffusion after Fick, convection of the electrolyte and the electrostatic influence of an electric field.

An electrolyte in a closed electrochemical cell is not subject to convection giving $u = 0$ and in a dilute ion concentration the diffusion coefficient can be assumed constant as well as electrostatic correlation can be neglected setting $\frac{\partial A}{\partial t} = 0$. A simplified expression results

$$\frac{\partial c_i}{\partial t} = \nabla \left[D_i \nabla c_i + \frac{D_i z_i e}{\mathrm{k_B} T} c_i \left(\nabla \Phi \right) \right]. \tag{B.3}$$

Considering the long time limit of the ion motion under the influence of an electric field, a steady state $\nabla^2 c_i = 0$ will be reached yielding a constant flux

$$F_i = - \left[D_i \nabla c_i + \frac{D_i z_i e}{\mathrm{k_B} T} c_i \left(\nabla \Phi \right) \right]. \tag{B.4}$$

The total current density $\vec{J}$ consists of the individual fluxes

$$\vec{J} = \sum_i z_i e F_i \tag{B.5}$$

and in the bulk of the electrolyte charge neutrality can be assumed yielding an overall charge density $\rho_e = 0$ and a constant current density

$$\rho_e = \sum_i z_i e c_i = 0; \qquad \frac{\partial \rho_e}{\partial t} = \nabla \vec{J} = 0 \tag{B.6}$$

Considering a binary electrolyte containing two ions A^+ and B^- with charges z_A and z_B where the free diffusion of one species is hindered e.g. by an electrode permeable to only A^+ a concentration polarization scenario arises. As indicated in Fig. 2.1 species B^- will establish a concentration gradient under the influence of the field $\nabla\Phi$ directed in x which will yield a field gradient $\frac{d\Phi}{dx}$. Due to the necessity to maintain charge neutrality, i.e. following quasi charge neutrality A^+ will establish a proportional concentration gradient after equ. B.6 giving [1, 2]

$$c = c_A z_A = c_B z_B \tag{B.7}$$

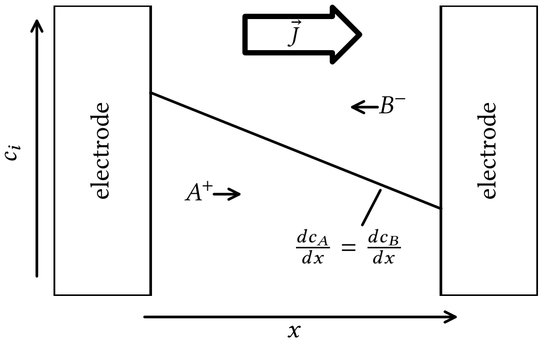

Fig. 2.1: Schematic polarization concentration profile dc/dx for a one dimensional binary dilute electrolyte under the influence of an electric field establishing the current density $\vec{J}$. Species A^+ establishes a flux in the steady state and the diffusion of species B^- is hindered.

In the steady state there is no flux of species B^- ($F_B = 0$), with equ. B.4 and a electric field directed in x follows

$$0 = -D_B \nabla c_B + \frac{D_B z_B e}{\mathrm{k_B} T} c_B \left(\frac{d\Phi}{dx}\right) \tag{B.8}$$

giving an expression for $\frac{d\Phi}{dx}$

$$\frac{d\Phi}{dx} = \frac{dc_B}{dx} \frac{1}{c_B z_B} \frac{\mathrm{k_B} T}{e} \tag{B.9}$$

For the current density $\vec{J}$ follows:

$$\vec{J} = z_A e F_A = -z_A e \left(D_A \frac{dc_A}{dx} + \frac{D_A z_A e}{\mathrm{k_B} T} c_A \frac{d\Phi}{dx}\right). \tag{B.10}$$

Inserting the expression for $\frac{d\Phi}{dx}$ (equ. B.9)

$$\vec{J} = -z_A e D_A \left(\frac{dc_A}{dx} + \frac{c_A z_A}{c_B z_B} \frac{dc_B}{dx}\right). \tag{B.11}$$

Based on the quasi charge neutrality (equ. B.7), the expression simplifies to

$$\vec{J} = -z_A e D_A \left(\frac{dc_A}{dx} + \frac{dc_B}{dx}\right) \tag{B.12}$$

Finally, if $z_A = -z_B$ the concentration gradients are identical giving

$$\vec{J} = -2 z_A e D_A \frac{dc}{dx} \tag{B.13}$$

This expression allows to determine the concentration gradient in dependence of the applied current density $\vec{J}$.

Appendix Bibliography

[1] J. Newman and K. Thomas-Alyea, *Electrochemical systems*, 3rd (Wiley-Interscience, 2004) (cit. on pp. 109, 110).

[2] R. O'Hayre and C. Suk-Won, *Fuel cell fundamentals*, 2nd (Wiley, 2009) (cit. on p. 110).